

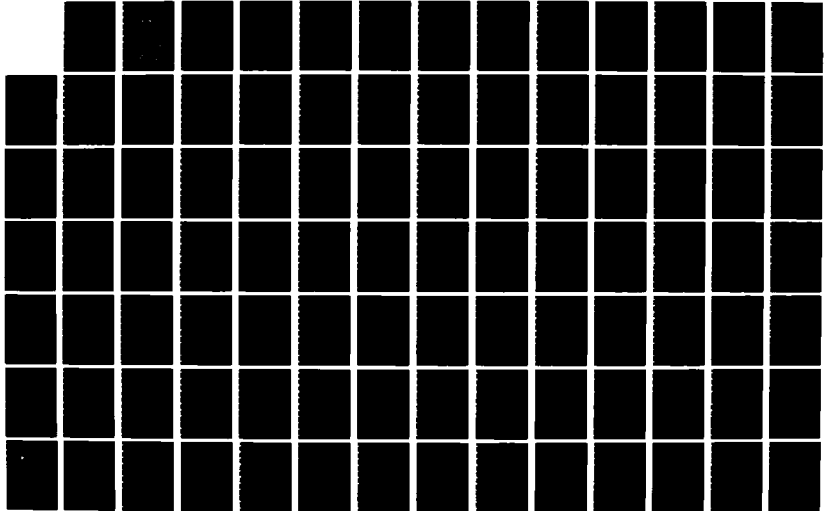
AD-A172 145

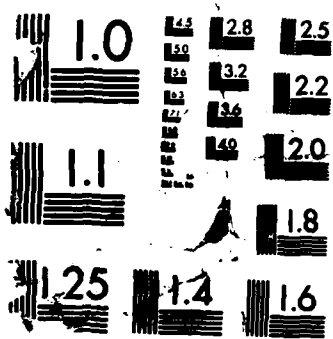
A MIXED COMPUTATIONAL ALGORITHM BASED ON THE UPDATED  
LAGRANGIAN DESCRIPTI (U) VIRGINIA POLYTECHNIC INST AND  
STATE UNIV BLACKSBURG DEPT OF E P R HEYLIGER ET AL.  
AUG 86 VPI-E-86-17 N00014-84-K-0552 F/G 12/1

1/2

UNCLASSIFIED

NL





MICROCOPY RESOLUTION TEST CHART  
NATIONAL BUREAU OF STANDARDS-1963-A

AD-A172 145

OF **COLLEGE  
ENGINEERING**

A MIXED COMPUTATIONAL ALGORITHM BASED ON THE UPDATED  
LAGRANGIAN DESCRIPTION FOR PLANE ELASTIC  
CONTACT PROBLEMS

by

P. R. Heyliger and J. N. Reddy  
Department of Engineering Science and Mechanics  
Virginia Polytechnic Institute and State University  
Blacksburg, VA 24061

OTC FILE COPY



**VIRGINIA  
POLYTECHNIC  
INSTITUTE  
AND  
STATE  
UNIVERSITY**

**S** DTIC  
ELECTE  
SEP 24 1986  
**D**  
**E**

BLACKSBUR  
VIRGINIA

This document has been approved  
for public release and sale; its  
distribution is unlimited.

86 9 24 058

Department of the Navy  
OFFICE OF NAVAL RESEARCH  
Mechanics Division  
Arlington, Virginia 22217

Contract N00014-84-K-0552  
Project NR 064-727/5-4-84 (430)

Research Reort No. VPI-E-86.17

A MIXED COMPUTATIONAL ALGORITHM BASED ON THE UPDATED  
LAGRANGIAN DESCRIPTION FOR PLANE ELASTIC  
CONTACT PROBLEMS

by

P. R. Heyliger and J. N. Reddy  
Department of Engineering Science and Mechanics  
Virginia Polytechnic Institute and State University  
Blacksburg, VA 24061

DTIC  
SEP 2 1986

August, 1986

Approved for public release, distribution unlimited.

**A MIXED COMPUTATIONAL ALGORITHM BASED ON THE UPDATED  
LAGRANGIAN DESCRIPTION FOR PLANE ELASTIC  
CONTACT PROBLEMS**

P. R. Heyliger and J. N. Reddy  
Department of Engineering Science and Mechanics  
Virginia Polytechnic Institute and State University  
Blacksburg, Virginia 24061

**ABSTRACT**

A mixed variational statement and corresponding finite element model are developed for an arbitrary plane-body undergoing large deformations (i.e. large displacements, large rotations and small strains) under external loads using the updated Lagrangian formulation. The mixed finite element formulation allows the nodal displacements and stresses to be approximated independently.

Two algorithms are discussed for the analysis of a thin, uniformly loaded plate with a circular hole in contact with a pin. The different algorithms consider the separate cases of a rigid pin and a flexible pin, and use different methods to account for the computational difficulties that arise from the unknown contact area and the presence of friction between the pin and the plate. A number of different contact problems are solved using these two techniques.

A hybrid technique is presented that combines the numerical technique of the finite element method with the experimental technique of moire interferometry. The displacements at the pin-hole interface are measured from physical experiments and are then used as prescribed boundary conditions in the finite element analysis of the modeled problem. Results of this algorithm are compared with solutions obtained from strictly computational algorithms that are independent of the experimental data. The agreement is found to be very good.

Accession For	
NTIS GRA&I	<input checked="" type="checkbox"/>
DTIC TAB	<input type="checkbox"/>
Unannounced	<input type="checkbox"/>
Justification	
By _____	
Distribution/	
Availability Codes	
Dist	Avail and/or Special
A-1	



## TABLE OF CONTENTS

	Page
ABSTRACT	
TABLE OF CONTENTS	
1. INTRODUCTION.....	1
1.1 Motivation.....	1
1.2 Literature Review.....	3
1.3 The Present Study.....	6
2. GOVERNING EQUATIONS .....	11
2.1 Introduction.....	11
2.2 Mixed Virtual Work Formulation.....	11
2.3 Finite Element Model.....	18
2.4 Some Computational Aspects.....	22
3. NUMERICAL ALGORITHMS .....	27
3.1 Introduction.....	27
3.2 Rigid Pin Contact Algorithm.....	29
3.3 Elastic Pin Contact Algorithm.....	31
3.3.1 General Concepts.....	31
3.3.2 Finite Element Matrices.....	38
3.3.4 Determination of Stick and Slip.....	40
3.3.5 Computation of Contact Forces.....	42
4. A HYBRID NUMERICAL/EXPERIMENTAL TECHNIQUE .....	49
4.1 Introduction.....	49
4.2 Moire Interferometry.....	49
4.3 The Hybrid Technique.....	51
4.4 Description of the Plate.....	55
5. NUMERICAL EXAMPLES AND RESULTS.....	61
5.1 Introduction.....	61
5.2 Rigid Pin Algorithm Examples.....	61
5.2.1 Infinitely Long Cylinder Under Uniform Load.....	62
5.2.2 Orthotropic, Pin-Loaded Plate.....	62
5.3 Elastic Pin Algorithm Examples.....	67
5.3.1 Infinitely Long Cylinder Under Uniform Load.....	69
5.3.2 Orthotropic, Pin-Loaded Plate.....	78
5.3.3 Aluminum, Pin-Loaded Plate.....	86
5.4 Results of Hybrid Numerical/Experimental Technique.....	90
6. SUMMARY AND CONCLUSIONS.....	103
6.1 Summary.....	103
6.2 Conclusions.....	104
REFERENCES.....	108
APPENDIX.....	113

## 1. INTRODUCTION

### 1.1 Motivation

The solution of contact problems generally involves the determination of the states of displacement, strain, and stress acting within the domains of two or more separate bodies pressing against one another under external action. Unlike most problems in solid and structural mechanics, where the critical regions of interest are usually far removed from the point of application of the loads, the domain of interest in contact problems is the area at or near the region of contact, which is typically the region of load transfer. Contact stresses are typically among the largest stresses found within the contacting bodies.

The accurate numerical simulation of the response of two elastic bodies in contact with one another under external load remains as one of the most challenging problems of computational solid mechanics due to several inherent complications. The region or area of contact between the two bodies is changing continuously during the loading, and is generally not known a-priori as a function of the applied loading. In addition, the presence of friction between the two bodies creates varying regions of stick and slip. Hence this type of problem is highly nonlinear, and although some exact elasticity solutions exist, these are typically for problems with simple geometrical shapes and frictional conditions. Numerical techniques must therefore be used to solve problems involving more complicated geometries and contact conditions.

The finite element method has long been established as a versatile and powerful tool of analysis for solid and structural mechanics problems and has recently been applied to numerous studies of elastic

contact problems. Mixed finite element models, in which independent approximations of displacements and stresses are introduced, have also been developed and applied to problems in solid mechanics, but to a much lesser extent. Mixed formulations would appear to be especially applicable to contact problems since the stresses at the contact boundary are computed as part of the solution rather than part of the post-computation as practiced in displacement formulations. These boundary stresses are of extreme importance in computing the regions of stick and slip and are useful in other steps of the analysis as well.

Among the many different types of contact problems found in engineering, the problem of a thin, pin-loaded plate has recently received considerable attention, particularly due to the increasing use of composite materials in modern structural applications [1-10]. Elasticity solutions and finite element approximations have dominated the majority of these analyses, most of which have ignored the effects of the pin by assuming that it is rigid and hence have only modeled and subsequently analyzed the domain of the plate. A number of other simplifying assumptions were invoked in many of these analyses, including the assumptions of a cosinusoidal radial traction on the hole boundary as well as a constant coefficient of friction acting between the pin and the plate. In addition, various assumptions were made to approximate the behavior of the contacting bodies at the contact region, since this information is required in order to obtain a solution to the problem, and is in general not known as a function of any of the parameters of the problem.

A review of the pertinent literature is presented in the following section to assess the gains made in the past and to indicate the



direction of recent research efforts in the analysis of elastic contact problems. Since most contact algorithms are strictly numerical, a brief review of geometrically nonlinear analysis is included, particularly highlighting the lack of studies regarding applications of mixed methods to nonlinear problems in plane elasticity in general, and contact problems in particular.

## 1.2 Literature Review

The displacement finite element model, based on the principle of minimum total potential energy, has been applied to many problems in structural engineering and solid mechanics since the early 1960's. The mathematical and numerical properties of the displacement finite element method have been firmly established and numerous publications allude to these advances. The textbooks by Reddy [11], Zienkiewicz [12], and Bathe [13] contain a host of references regarding both the historical development of and recent advances in most branches of finite element analysis.

Although the mathematical properties of mixed finite element approximations have seen extensive development in recent years [14-16], the applications of mixed models to actual physical problems have been relatively few. In linear, two-dimensional elasticity problems, the mixed finite element equations can be developed using the Hellinger-Reissner variational principle [17]. Dunham and Pister [18] were among the first to use this principle to introduce mixed finite element approximations and present numerical results for plane elasticity problems. They obtained displacements and stresses that were superior to those obtained using an equivalent displacement model. Pitkaranta and Sternberg [19] analyzed several mixed finite element methods for the

plane elasticity equations on a rectangular domain, while Mirza and Olsen [20] presented a more thorough study regarding the convergence and performance of the mixed finite element method for linear plane elasticity applications.

Contact problems are generally regarded as being highly nonlinear for two major reasons. First, the body or bodies under analysis might undergo large deformations, and hence must be modeled such that the new geometry and the most recent state of stress in each body are accounted for in an appropriate manner in the subsequent loading. Second, the boundary conditions change continuously as a result of the changes in the contact region with increasing load. The development of the governing finite element models for the nonlinear response of a solid body under external load has been developed by numerous investigators [21-32], but none of these have addressed mixed models for plane elasticity problems. Horrigmoe and Bergen [33] presented an incremental mixed variational principle and corresponding finite element model for solid bodies, but gave no numerical examples or comments on implementation.

Contact problems have challenged mathematicians and engineers for over a century. In 1881, Hertz obtained a solution for the problem of two elastic cylinders in contact with one another [34]. Numerous attempts have since been made to accurately model the physics of contact for more complicated problems using, among other methods, finite element techniques. Due to the inherent nonlinearity of the contact problem, all of the most successful of these algorithms contain several iterative procedures to account for the varying regions of contact and of stick and slip.

Nearly all investigations of contact problems using the finite element method have employed the more conventional displacement formulations. Chan and Tuba [35] used conventional elements and iterative procedures to solve several different contact problems. Bathe and Chaudhary [36] imposed the contact conditions by constructing the total potential of the nodal contact forces for an element in contact and adding this term to the original potential energy functional. Campos, Oden and Kikuchi [37] solved discretized contact problems using prescribed normal boundary tractions and nonlinear inequalities. Francavilla and Zienkiewicz [38] used the flexibility matrices of two elastic bodies in frictionless contact along with iterative procedures to check for penetration. This technique was later modified by Sachdeva and Ramakrishnan [39] to include the effects of friction. Marks and his colleagues [40-41] presented several solution techniques for contact problems using the conjugate gradient technique integrated with the finite element method for frictionless contact problems. Okamoto and Nakazawa [42] presented a technique which used three-dimensional elements and used the magnitude of load causing a change in the contact status of one node as a load step. Fredrickson [43] used iterative techniques to account for the contact conditions and also used a superelement technique to reduce the number of degrees of freedom.

Past studies of contact problems using mixed finite element models are not nearly as numerous as those using displacement models. Haslinger and Hlavacek [44] presented a mixed formulation for the Signorini problem with prescribed normal contact forces but gave no numerical results. Tseng and Olsen [45] applied the mixed finite

element method to several plane elasticity contact problems using the equations of linear elasticity along with an iterative scheme.

The increasing use of composite materials in structural applications has generated a great deal of interest in the problem involving a bolt or pin in contact with an elastic plate. Although a variety of techniques have been used to analyze this problem, most studies have used either elasticity or finite element solutions to obtain the states of displacement and stress in the plate [1-10]. Most analyses have neglected the elasticity of the pin by assuming that it is perfectly rigid [4-9], while others have assumed a cosinusoidal radial stress acting between the pin and the plate at the points of contact [1,2,10]. The validity of this latter assumption has been demonstrated experimentally for isotropic plates [3], but was recently shown to be incorrect for orthotropic plates by Hyer and Klang [46]. Of the numerical studies of the pin-loaded plate problem, the only analysis that accounted for the combined effects of nonlinearity, actual boundary loading, friction, and orthotropy of the plate was developed by Wilkinson, Rowlands, and Cook [47]. They presented a simple iterative technique to compute the stresses around the hole of a pin-loaded orthotropic plate. This method was later modified by Rahman et al. [48]. The results of these two techniques were also verified experimentally by Wilkinson and Rowlands [49]. A review of other pertinent methods in the displacement finite element analysis of pin joints is given by Rao [50].

### 1.3 The Present Study

Despite the gains made in recent years in the understanding of contact phenomena between solid bodies, the extreme complexity of such

problems has thwarted the development of a general and effective computational method of analysis. In particular, mixed finite element models, which contain stresses as nodal variables and hence would seem to be particularly suited for the analysis of contact problems, have seen extremely limited use, particularly in geometrically nonlinear analysis.

Furthermore, all numerical algorithms, regardless of the formulation used, are based on several key assumptions and approximations when performing an analysis on two or more bodies in contact. Various important quantities, such as the static and dynamic coefficients of friction, are assumed to be constant as a function of position and load. Hence it is difficult to isolate the effects of the different assumptions made in most computational schemes that have been developed in the past.

The present study will address each of these major difficulties or limitations and will primarily be directed toward the development of a computational technique for the analysis of two-dimensional contact problems. Different strategies developed here will use a mixed updated Lagrangian formulation as a basis for the analysis. This formulation has seen little or no use as a tool of analysis for elasticity problems in the past; however, it would be well suited for the analysis of contact problems since the displacements and stresses are approximated independently and each of the respective components appear as nodal variables. This immediately introduces the primary computational disadvantage of the mixed model compared to the displacement model in that there are five degrees of freedom per node for the mixed model whereas only two degrees of freedom per node in the displacement

model. However, this disadvantage must be weighed against the positive aspects of the mixed model. The computed nodal stresses are typically more accurate for the mixed model and also appear as part of the solution vector instead of requiring any post computations using the gradients of the displacements and the stress-strain relations of the material. This fact is of immediate value in the analysis of contact problems since the boundary stresses are required to compute the state of stick or slip at the nodes and also to compute tangential surface tractions due to friction for a contacting body.

In the purely numerical analysis of contact problems, different assumptions are made to approximate the behavior of the contacting bodies at the region of contact. For example, in most analyses, the material of one of the bodies is allowed to penetrate the domain of the second contact body and is then pushed back out during a subsequent portion of the analysis. In addition, the coefficients of friction used in the analysis are those determined from physical tests of specimens made of the materials in contact and are nearly always specified to be a constant throughout the domain for the duration of the analysis. These are two very basic but major assumptions frequently employed in the development of numerical schemes used to analyze contact problems. Although these assumptions are necessary in order to develop a relatively efficient algorithm, they may have drastic effects on the results of the analysis.

Considering these observations, a new method of analysis will be presented as a part of the present study that will attempt to eliminate the effects of some of the approximations made in the analysis of contact problems. This technique involves the combination of an

experimental technique, which determines the true state of the displacements on the contact boundary, with a finite element technique, which uses the information provided from the experimental technique to determine the states of displacement and stress within the rest of the domain under analysis.

The major objectives of the present study are three-fold. The first objective involves the development of a mixed updated Lagrangian formulation and corresponding finite element model of the plane elasticity equations for large deformation analysis. Second, the formulation will then be modified to develop several numerical algorithms for the analysis of two-dimensional contact problems. Finally, the mixed finite element model will be combined with the experimental technique of moire interferometry to form a hybrid method of analysis for the contact problem of a pin-loaded plate. The goal of this final task is quite different from that of the second task in that it is mainly being implemented to exclude the effects of the aforementioned computational assumptions on the stress distributions. On the other hand, the numerical schemes are self contained in that they do not depend on any experimental data, and will attempt to model the actual behavior of physical problems.

The following sections contain the formulation of and examples for the different schemes alluded to in this section. Section 2 contains the development of a mixed updated Lagrangian formulation and computational scheme for the analysis of two-dimensional elasticity problems. This formulation is extended in Section 3 to develop two computational algorithms to analyze the contact problem of a pin-loaded plate. These approaches are developed separately to consider the

distinct cases of allowing for a rigid pin or an elastic pin. In Section 4, a hybrid experimental/numerical technique is described that combines the experimental technique of moire interferometry and the numerical finite element method, again for the analysis of the pin-loaded plate problem. The results of several numerical examples from the algorithms developed in Sections 2-4 are presented in Section 5. Finally, summary and conclusions of the present study are given in Section 6.



## 2. GOVERNING EQUATIONS

### 2.1 Introduction

In this Section we begin with the statement of virtual work for an arbitrary solid body under external load and derive the variational statement that will be most convenient in applying the mixed finite element model to the problem. The finite element approximations for the displacements and stresses are then introduced into the variational statement for two-dimensional bodies resulting in the final matrix form of the finite element equations. The required specification of the boundary conditions is discussed using the variational form of the linear equilibrium and stress-displacement relations of the problem, and an alternative formulation of the linear finite element matrices is given as well. A brief discussion of the required order of polynomial approximation for the mixed finite elements is also given.

### 2.2 Mixed Virtual Work Formulation

We begin our derivation by first assuming that the current configuration  $C_1$  is known at time  $t$  as well as all equilibrium configurations previous to this time. We desire the solution, i.e. the displacements, strains, and stresses, at the configuration  $C_2$  at time  $t + \Delta t$  (see Figure 2.1). Using the principle of virtual displacements (see [51]), we can write

$$\int_{V_2} {}^2\tau_{ij} \delta({}_2e_{ij}) dV - \delta({}^2F) = 0 \quad (2.1a)$$

where

$$\delta({}^2F) \equiv \int_{V_2} {}^2f_i \delta u_i dV + \int_{S_2} {}^2t_i \delta u_i ds \quad (2.1b)$$

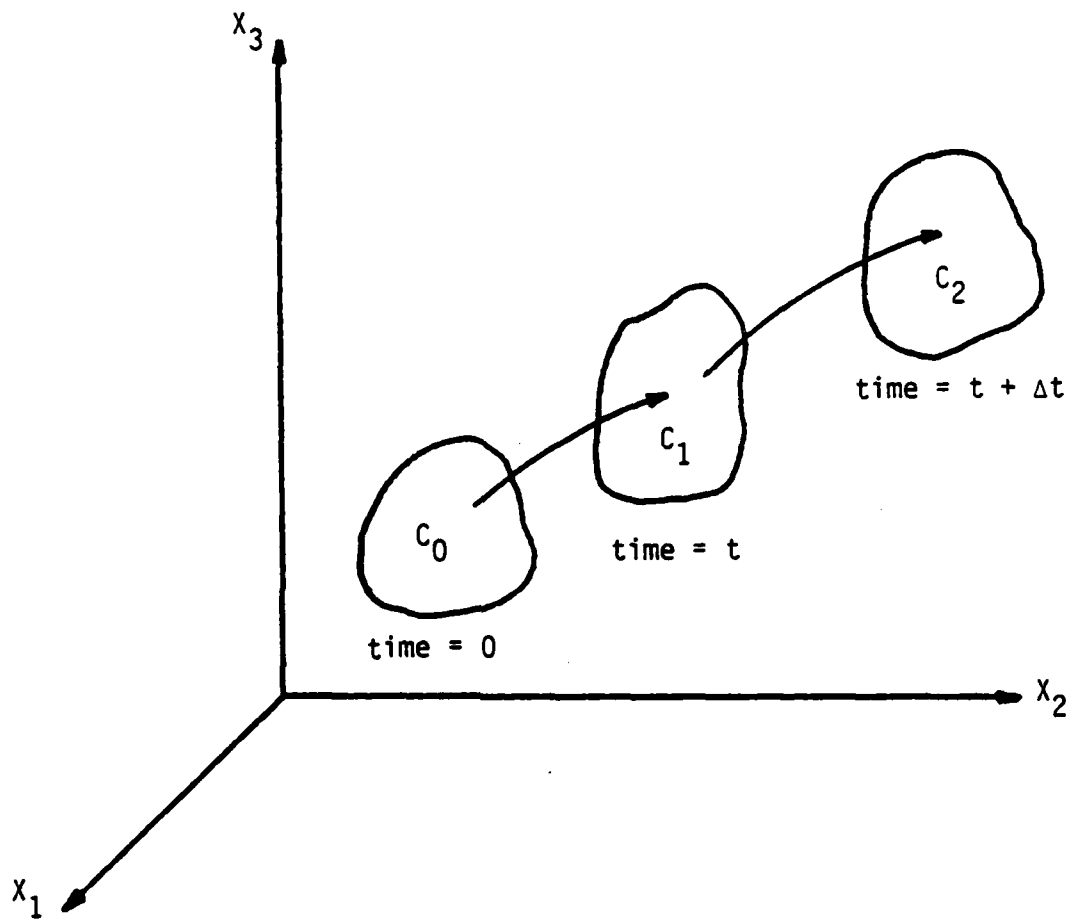


Figure 2.1 Motion of an arbitrary continuum in Cartesian coordinates

${}^2\tau_{ij}$  = the Cartesian components of the Cauchy stress tensor in the configuration  $C_2$  occupying the volume  $V_2$ ,

$u_i$  = the Cartesian components of the displacement vector in going from configuration  $C_1$  to configuration  $C_2$ ,

${}^2e_{ij}$  = the Cartesian components of the infinitesimal strain tensor associated with  $u_i$  which is defined as

$${}^2e_{ij} = \frac{1}{2} \left( \frac{\partial u_i}{\partial x_j} + \frac{\partial u_j}{\partial x_i} \right) \quad (2.2)$$

$x_i$  = the Cartesian components of a point in configuration  $C_2$ ,

${}^2f_i$  = the Cartesian components of the body force vector measured in configuration  $C_2$ .

${}^2t_i$  = the Cartesian components of the surface stress vector measured in configuration  $C_2$ .

Here  $\delta$  denotes the variational operator and  $\delta u_i$  denotes the virtual displacement vector (i.e. the variation of  $u_i$ ).

Although this statement is valid at time  $t + \Delta t$ , it is not immediately useful since the integrations are performed over domains that are not yet known. However, we may transform this equation into a known configuration using appropriate stress and strain measures [52]. To do this, we first define the second Piola-Kirchhoff stress tensor as

$${}^2S_{ij} = \frac{\rho_0}{\rho} \frac{\partial X_i}{\partial x_m} \cdot {}^2\tau_{mn} \cdot \frac{\partial X_j}{\partial x_n} \quad (2.3)$$

where  $X_i$  are the Cartesian coordinates of a generic point in configuration  $C_1$ ,  $\rho_0$  is the density in  $C_1$  and  $\rho$  denotes the density in  $C_2$ . We have indicated in the notation that the second Piola-Kirchhoff stress tensor is measured in  $C_2$  but is referred to  $C_1$ . Since the Cauchy stress tensor is defined as force per unit area of the deformed

configuration, it is always measured in and referred to the most current configuration. Hence, we may write

$${}^2S_{ij} = {}^2\tau_{ij} \equiv {}^2\tau_{ij} \quad (2.4)$$

We next define the components of the Green-Lagrange strain tensor as

$${}^2E_{ij} = \frac{1}{2} \left( \frac{\partial u_i}{\partial X_j} + \frac{\partial u_j}{\partial X_i} + \frac{\partial u_m}{\partial X_i} \frac{\partial u_m}{\partial X_j} \right) \quad (2.5)$$

Just as the Cauchy and second Piola-Kirchhoff stress tensors are related by a kinematic transformation (2.3), the variation in the Green-Lagrange strain tensor  $E_{ij}$  and the variation in the infinitesimal strain tensor  $e_{ij}$  are related by

$$\delta({}^2E_{ij}) = \frac{\partial x_m}{\partial X_i} \frac{\partial x_n}{\partial X_j} \delta({}^2e_{mn}) \quad (2.6)$$

Clearly, both of these strain tensors use the particle displacements  $u_i$  in going from configuration  $C_1$  to configuration  $C_2$ .

We next note that the second Piola-Kirchhoff stress tensor is energetically conjugate to the Green-Lagrange strain tensor and the Cauchy stress tensor is energetically conjugate to the infinitesimal strain tensor. In other words, if we use the definitions in Eqs. (2.3) and (2.6) along with the identities

$$\frac{\partial x_i}{\partial X_j} \frac{\partial x_j}{\partial x_m} = \delta_{im} \quad (2.7)$$

and

$$\rho_0 dV_1 = \rho dV_2 \quad (2.8)$$

then we may write the expression for the internal virtual work given in Eq. (2.1) as

$$\int_{V_1} {}^2_1 S_{ij} \delta({}^2_1 E_{ij}) dV = \int_{V_2} {}^2 \tau_{ij} \delta({}^2 e_{ij}) dV \quad (2.9)$$

Substituting Eq. (2.9) into Eq. (2.1), we obtain our modified statement of virtual work, which is now in terms of a known configuration, and is given by

$$0 = \int_{V_1} {}^2_1 S_{ij} \delta({}^2_1 E_{ij}) dV - \delta({}^1 F) \quad (2.10)$$

We have also implied the assumption that the applied loading is independent of the deformation of the structure, and hence

$$\delta({}^2 F) = \delta({}^1 F) \quad (2.11)$$

Next, we use the incremental decompositions of the stresses and strains to write

$$\begin{aligned} {}^2_1 S_{ij} &= {}^1 \tau_{ij} + {}^1 S_{ij} \\ {}^2_1 E_{ij} &= {}^1 e_{ij} + {}^1 n_{ij} \end{aligned} \quad (2.12)$$

where

$$\begin{aligned} {}^1 S_{ij} &= \text{incremental components of 2nd Piola-Kirchhoff stress tensor} \\ {}^1 e_{ij} &= (\text{incremental}) \text{ components of the infinitesimal strain tensor} \\ &= \frac{1}{2} \left( \frac{\partial u_i}{\partial X_j} + \frac{\partial u_j}{\partial X_i} \right), \\ {}^1 n_{ij} &= \frac{1}{2} \frac{\partial u_m}{\partial X_i} \frac{\partial u_m}{\partial X_j} \end{aligned} \quad (2.13)$$

Substituting Eq. (2.12) into Eq. (2.10) gives

$$0 = \int_{V_1} ({}^1\tau_{ij} + {}^1S_{ij}) \delta({}^1e_{ij} + {}^1n_{ij}) dV - \delta({}^1F) \quad (2.14)$$

or

$$\begin{aligned} \int_{V_1} {}^1S_{ij} \delta({}^1e_{ij} + {}^1n_{ij}) dV + \int_{V_1} {}^1\tau_{ij} \delta({}^1n_{ij}) dV \\ = - \int_{V_1} {}^1\tau_{ij} \delta({}^1e_{ij}) dV + \delta({}^1F) \end{aligned} \quad (2.15)$$

We next linearize the equations by assuming that

$${}^1S_{ij} = {}^1C_{ijrs} e_{rs}, \quad \delta_1^2 E_{ij} = \delta_1 e_{ij} \quad (2.16)$$

and thus obtain the approximate governing equation

$$\begin{aligned} \int_{V_1} {}^1C_{ijrs} {}^1e_{rs} \delta({}^1e_{ij}) dV + \int_{V_1} {}^1\tau_{ij} \delta({}^1n_{ij}) dV \\ = - \int_{V_1} {}^1\tau_{ij} \delta({}^1e_{ij}) dV + \delta({}^1F) \end{aligned} \quad (2.17)$$

The above linearization can be interpreted as a representation of the nonlinear curve between two consecutive load steps by a linear line segment, and must be solved iteratively.

A mixed (or stationary) virtual work statement that treats the displacements and stresses as independent variables can be derived from Eq. (2.17) as follows. First, we note that Eq. (2.17) is the first variation of the functional

$$\Pi = \int_{V_1} \frac{1}{2} {}^1C_{ijrs} {}^1e_{rs} {}^1e_{ij} dV + \int_{V_1} {}^1\tau_{ij} ({}^1e_{ij} + {}^1n_{ij}) dV - {}^1F \quad (2.18)$$

Next, we introduce the stresses as additional dependent variables by treating the strain-displacement relations

$$1e_{ij} = \frac{1}{2} \left( \frac{\partial u_i}{\partial X_j} + \frac{\partial u_j}{\partial X_i} \right) \quad (2.19)$$

as constraints. The increments in the 2nd Piola-Kirchhoff stress tensor components  $1S_{ij}$  act as the Lagrange multipliers (see [51]). The modified functional for the mixed formulation becomes

$$\Pi_L = \Pi - \int_{V_1} 1S_{ij} \left[ 1e_{ij} - \frac{1}{2} \left( \frac{\partial u_i}{\partial X_j} + \frac{\partial u_j}{\partial X_i} \right) \right] dV \quad (2.20)$$

where  $\Pi$  is given by Eq. (2.18).

We next write the linearized expressions for the strain energy density  $U_0$  and the complementary strain energy density  $U_0^*$  due to the incremental displacements as

$$U_0 = \frac{1}{2} C_{ijkl} 1e_{ij} 1e_{kl} \quad (2.21)$$

and

$$U_0^* = \frac{1}{2} D_{ijkl} 1S_{ij} 1S_{kl} \quad (2.22)$$

where  $D_{ijkl}$  are the components of the compliance tensor. The strain energy density and the complementary strain energy densities are related according to

$$\begin{aligned} -U_0^* &= U_0 - 1S_{ij} 1e_{ij} \\ &= \frac{1}{2} C_{ijkl} 1e_{ij} 1e_{kl} - 1S_{ij} 1e_{ij} \end{aligned} \quad (2.23)$$

Using Eqs. (2.22) and (2.23) in Eq. (2.20), we obtain

$$\Pi_L = \int_{V_1} \left[ 1\tau_{ij} (1e_{ij} + 1\eta_{ij}) + \frac{1}{2} 1S_{ij} \left( \frac{\partial u_i}{\partial X_j} + \frac{\partial u_j}{\partial X_i} \right) - U_0^* \right] dV - \delta(1F) \quad (2.24)$$

Imposing stationarity on this functional with respect to the displacements and the stresses, we obtain the two approximate equilibrium equations

$$\int_{V_1} {}^1\tau_{ij}\delta({}^1n_{ij})dV + \int_{V_1} {}^1S_{ij}\delta u_{i,j}dV = \delta({}^1F) - \int_{V_1} {}^1\tau_{ij}\delta({}^1e_{ij})dV \quad (2.25a)$$

$$\int_{V_1} u_{i,j}\delta({}^1S_{ij})dV - \int_{V_1} D_{ijkl} {}^1S_{kl}\delta({}^1S_{ij})dV = 0 \quad (2.25b)$$

These two equations are analogous to Eq. (2.17) for the displacement formulation. Since these equations are a linearized version of the true statement of equilibrium, they must be solved simultaneously and repeatedly for a given load until the increments of the displacement and stress components are within a preassigned tolerance. The final solution vector, after convergence, will represent the true state of equilibrium for a given load, and the iterations are therefore frequently termed equilibrium iterations.

### 2.3 Finite Element Model

We next construct the finite element model of Eqs. (2.25) for the two-dimensional case. We begin by assuming independent approximations of the displacements and stresses of the form

$$u_i(x_1, x_2) = \sum_{j=1}^n u_i^j \psi_j(x_1, x_2) \quad (2.26)$$

$${}^1S_{ij}(x_1, x_2) = \sum_{k=1}^n {}^1S_{ij}^k \psi_k(x_1, x_2) \quad (2.27)$$

where  ${}^1S_{ij}^k$  denote the value of  ${}^1S_{ij}$  at the k-th node. Substituting these expressions into the two equilibrium equations in Eq. (2.25) gives

$$\begin{bmatrix} [K^{11}] & [K^{12}] \\ [K^{12}]^T & [K^{22}] \end{bmatrix} \begin{Bmatrix} \{u\} \\ \{S\} \end{Bmatrix} = \begin{Bmatrix} \{F^L\} \\ \{0\} \end{Bmatrix} - \begin{Bmatrix} \{F^{NL}\} \\ \{0\} \end{Bmatrix} \quad (2.28)$$

where

$$[K^{11}] = t \int_{A_1} [B^\sigma]^T [\tau] [B^\sigma] dA$$



$$[K^{22}] = t \int_{A_1} [\psi^\sigma]^T [D] [\psi^\sigma] dA$$

$$[K^{12}] = t \int_{A_1} [B^L]^T [\psi^\sigma] dA$$

$$\{F^L\} = t \int_{A_1} [\psi]^T \{f\} dA$$

$$\{F^{NL}\} = t \int_{A_1} [B^L]^T \{\tau\} dA$$

$$[\psi^\sigma]_{(3 \times 3n)} = \begin{bmatrix} \psi_1 & 0 & 0 & \psi_2 & 0 & 0 & \dots & \psi_n & 0 & 0 \\ 0 & \psi_1 & 0 & 0 & \psi_2 & 0 & \dots & 0 & \psi_n & 0 \\ 0 & 0 & \psi_1 & 0 & 0 & \psi_2 & \dots & 0 & 0 & \psi_n \end{bmatrix}$$

$$[D] = \begin{bmatrix} D_{11} & D_{12} & D_{16} \\ D_{12} & D_{22} & D_{26} \\ D_{16} & D_{26} & D_{66} \end{bmatrix} \quad (2.29)$$

$$[B^L]_{(3 \times 2n)} = \begin{bmatrix} \psi_{1,1} & 0 & \psi_{2,1} & 0 & \dots & \psi_{n,1} & 0 \\ 0 & \psi_{1,2} & 0 & \psi_{2,2} & \dots & 0 & \psi_{n,2} \\ \psi_{1,2} & \psi_{1,1} & \psi_{2,2} & \psi_{2,1} & \dots & \psi_{n,2} & \psi_{n,1} \end{bmatrix}$$

$$[B^\sigma]_{(4 \times 2n)} = \begin{bmatrix} \psi_{1,1} & 0 & \psi_{2,1} & 0 & \dots & \psi_{n,1} & 0 \\ \psi_{1,2} & 0 & \psi_{2,2} & 0 & \dots & \psi_{n,2} & 0 \\ 0 & \psi_{1,1} & 0 & \psi_{2,1} & \dots & 0 & \psi_{n,1} \\ 0 & \psi_{1,2} & 0 & \psi_{2,2} & \dots & 0 & \psi_{n,2} \end{bmatrix}$$

$$[\tau] = \begin{bmatrix} \tau_{11} & \tau_{12} & 0 & 0 \\ \tau_{12} & \tau_{22} & 0 & 0 \\ 0 & 0 & \tau_{11} & \tau_{12} \\ 0 & 0 & \tau_{12} & \tau_{22} \end{bmatrix}$$

Here  $n$  is equal to the number of nodes in the element and  $\tau_{ij}$  represent the Cauchy stress components that have been determined at the last known configuration.

As mentioned in the previous section, the equilibrium equations are only approximate since we have linearized the true equations of motion. For this reason, there may be errors introduced into the computed solution at each load level, particularly if the load increment is large. To correct for this, we minimize the force imbalance that results from the linearization process for a given load increment. We do this by updating the stiffness matrices and force vectors to account for the change in the nodal positions and the Cauchy stresses during a given load step. The iterations are continued until the force imbalance, represented by the right hand side vector, is reduced to below some convergence limit. For example, the displacement and stress component increments at the  $(i + 1)$ st iteration for the solution at time  $t + \Delta t$  are calculated using

$$([K^L] + [K^{NL}])_i \{\Delta\}_{i+1} = \{F\}^L - \{F\}_i^{NL} \quad (2.30)$$

where the superscripts  $L$  and  $NL$  denote the linear and nonlinear contributions, respectively, and the stiffness and force terms have been computed using the displacements and stresses known from the previous iteration  $i$ .

Equation (2.30) must be solved repeatedly until the force imbalance is reduced to below or within a fixed tolerance. This amounts to measuring the percentage of the displacement and stress increments (measured using the Euclidean norm of the incremental solution vector) relative to the Euclidean norm of the total solution vector. When the increase in the displacements and stresses has been reduced to below a very small percentage of the total solution, the approximate state of equilibrium has been obtained for the given load step, and the load may then be increased or the analysis may be terminated.

The solution of Eq. (2.30) allows us to compute the total displacements according to the equation

$${}^2u_i = {}^1u_i + u_i \quad (2.31)$$

In the mixed formulation, there is no need to compute the Cauchy stresses using the Almansi strains as is required in the displacement formulation. Since the increments of the 2nd Piola-Kirchhoff stress tensor are computed as nodal variables, we simply use our incremental decomposition of the stress given in Eq. (2.12) as

$${}^2S_{ij} = {}^1\tau_{ij} + {}^1S_{ij} \quad (2.32)$$

To obtain the values of the Cauchy stresses within a given element as required in the computations of the nonlinear stiffness matrix and force vector, we may simply use nodal stress interpolation, or

$$\tau_{ij}(x_1, x_2) = \sum_{k=1}^n \tau_{ij}^k \psi_k(x_1, x_2) \quad (2.33)$$

When the increment in the  ${}^1S_{ij}$  terms is reduced to be within the required tolerance, we have by definition of the second Piola-Kirchhoff

stress tensor

$${}^2S_{ij} = {}^2\tau_{ij} \quad (2.34)$$

and we have clearly obtained the desired configuration  $C_2$ .

#### 2.4 Some Computational Aspects

If the element stiffness matrices shown in Eq. (2.28) are assembled in the form shown, the matrix  $[K^{11}]$  will be a null matrix for the first iteration of the first load step since the Cauchy stresses are zero everywhere in the domain for the undeformed configuration  $C_0$ . The global stiffness matrix counterpart of the submatrix  $[K^{11}]$  will also be a null matrix, resulting in an indefinite system of equations. The use of pivoting will eliminate this problem but will generally destroy the bandwidth of the system of equations. Mirza [53] has suggested premultiplying the left and right hand sides of the global finite element equation by the transpose of the global stiffness matrix, as in the least squares technique, to yield a positive definite system. In the present study, the first node of the finite element mesh was selected such that both of its displacements were specified to be zero. This results in the value 1.0 being placed in the diagonal position for the first two rows of the global stiffness matrix during the imposition of the boundary conditions. As the Gauss elimination is performed on each row of this matrix, the zeros on the diagonal corresponding to the remaining displacement degree's of freedom are eliminated. Hence, as long as the nodes are numbered as described here, a conventional banded solver may be used to solve the global system of equations.

An important note on the order of polynomial approximations used in the mixed model is in order. The variational statements of the governing differential equations for problems in plane elasticity given in Eqs. (2.25) show that the stress components appear undifferentiated whereas the displacement components  $u$  and  $v$  are each differentiated once with respect to the  $x$  and  $y$  coordinate directions. Hence to ensure continuity, the stress components must be approximated by at least a constant within the element and the displacement components must be at least linear in both  $x$  and  $y$  within an element. The approximation order should also be such that the mathematical definitions of the displacements and stresses are accounted for and are consistent with one another, i.e. the stresses are a function of the gradients of the displacements.

The continuity requirements of the variational statement of the problem alone are not sufficient in guaranteeing that the mixed finite element matrices will be acceptable for the analysis of a given problem. Unless the displacement and stress approximations are of a given order, the element matrices will contain more than the allowable three zero eigenvalues corresponding to the three rigid body modes for two-dimensional bodies. This point was examined in detail by Mirza and Olsen [20] who proposed and verified a completeness criterion that restricts the choice of the order of approximation for the displacements and stresses. The completeness criterion was given as:

*The strains from the stress approximations  
should possess at least all the strain modes  
that are present in the strains derived from the  
displacement approximations.*

When this criterion is violated, the global stiffness matrix in the mixed model will be singular even after the imposition of the boundary conditions. Isoparametric rectangular elements are used for all of the examples considered herein and, to meet the requirements of the completeness criterion, only linear-linear or quadratic-quadratic combinations are used to approximate the distributions of displacements and stresses in the mixed model.

A comment concerning the assembly of the element equations in a mixed formulation deserves attention. The assembly of the element stiffness matrices over the complete domain of the problem to construct the global stiffness matrix requires that the stresses be continuous across each interface between all elements. Although this assumption is valid for many problems, there are cases where the material properties, and hence one or more of the three stress components, are discontinuous. Such an example can be found in the bending of a composite beam. Clearly, mixed elements should not be used in the analysis of such problems, since the stresses will be erroneous at the points of material discontinuity.

One way to circumvent this difficulty is to condense out the stress degrees of freedom at the element level so that the continuity of the stresses across the element interface is no longer enforced. To do this we recall from Eq. (2.28) that the finite element equations can be written in partitioned form as

$$\begin{bmatrix} [K^{11}] & [K^{12}] \\ [K^{12}]^T & [K^{22}] \end{bmatrix} \begin{Bmatrix} \{u\} \\ \{s\} \end{Bmatrix} = \begin{Bmatrix} \{F\} \\ \{0\} \end{Bmatrix} \quad (2.35)$$

The second of these two matrix equations can be written as

$$[K^{12}]^T \{u\} + [K^{22}] \{s\} = \{0\} \quad (2.36)$$

Hence the nodal stress vector for a given element becomes

$$\{s\} = - [K^{22}]^{-1} [K^{12}]^T \{u\} \quad (2.37)$$

Substituting Eq. (2.37) into Eq. (2.36), we obtain

$$[K^{11}] \{u\} - [K^{12}] [K^{22}]^{-1} [K^{12}]^T \{u\} = \{F\} \quad (2.38)$$

or

$$[K^*] \{u\} = \{F\} \quad (2.39)$$

where

$$[K^*] = [K^{11}] - [K^{12}] [K^{22}]^{-1} [K^{12}]^T \quad (2.40)$$

Equation (2.40) is assembled as usual, and is solved for the nodal displacements (after applying the boundary conditions). The nodal stresses that were condensed out are then computed at the element level using Eq. (2.37). Since the stresses are no longer nodal variables, they will be discontinuous between elements.

Two points regarding the condensation procedure using linear elements merit some discussion. First, it can be shown that the matrix  $[K^*]$  in Eq. (2.40) is precisely the element stiffness matrix derived from a displacement formulation. Second, computing the nodal stresses using Eq. (2.37) yields exactly the same stresses as those computed using the procedures typically followed in a displacement formulation, i.e., computing the strains at the node points and then using the constitutive relations to compute the stresses. As with the condensation procedure, the stresses computed in a displacement formulation are not continuous between elements due to the discontinuity of the gradients of the displacements.

Although the condensation procedure results in the stiffness matrix derived from a displacement formulation for the case of linear elements,

this equivalence does not generally hold for elements containing higher-order approximations. For example, a quadratic isoparametric element will have the exact same stiffness matrices computed from Eq. (2.59) as from a displacement formulation only if the element shape is rectangular. If the element sides are not parallel with one another, the entries in the two stiffness matrices will not be identically the same, although they should be fairly close to one another. As the element shape differs from that of a rectangle, the discrepancies increase. Hence a quadratic element with curved sides will possess larger differences between the entries of the stiffness matrices computed from the two different approaches than will a quadratic element with the shape of a quadrilateral.



### 3. NUMERICAL ALGORITHMS

#### 3.1 Introduction

In this section we discuss two techniques for the analysis of two-dimensional elastic contact problems. Contact problems have a host of computational difficulties since the regions of contact are typically not known as a function of any of the parameters of the problem nor are the regions of relative stick and slip between the two contacting bodies due to the presence of friction. Most current numerical algorithms that solve contact problems are relatively complex and use a number of iterative schemes to account for the changing boundary conditions and regions of contact.

The nonlinear mixed finite element model described in Section 2 forms the cornerstone of the methods described in this section. The displacement finite element model has been used almost exclusively in previous numerical analyses of contact problems. Mixed elements provide the immediate advantage of computation of stresses as nodal variables, which is ideal for contact problems since the stresses may be obtained precisely on the contact boundary.

Although a number of contact problems may be analyzed by the two methods to be described in this section, the basic problem of interest involves a thin, pin-loaded plate under a uniform in-plane load, as shown in Figure 3.1. The plate may be orthotropic or isotropic, and the pin is generally considered to be isotropic. The first algorithm allows for the assumption of a rigid pin, and the second algorithm is much more general and allows for an elastic pin.

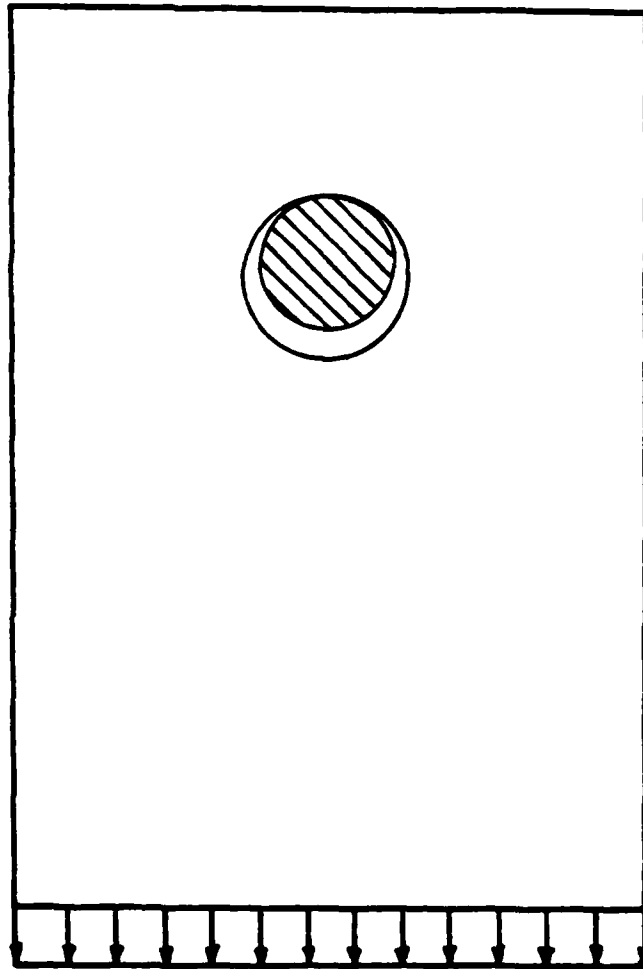


Figure 3.1 Elastic plate restrained by a pin and subjected to a uniform, in-plane load

### 3.2 Rigid Pin Contact Algorithm

In general, contact problems involve two or more elastic bodies pressing against one another under external or internal load. In the case of a pin-loaded plate, the bodies of interest are the plate and the pin. If the assumption of a rigid pin is used, the analysis is simplified considerably. This assumption eliminates the need to analyze the pin, which not only provides a known point of reference for the ensuing contact (i.e. the surface of the pin), but also drastically reduces the resulting global finite element system of equations since there is no need to discretize the domain of the pin. The assumption of a rigid pin is reasonable if the modulus of elasticity of the pin is much higher than that of the plate. Analytical studies have also shown that, in the contact analysis of composite plates, pin elasticity is not an important variable and has a relatively small effect on the resulting stress distributions [46].

One simple and effective method for analyzing thin, orthotropic, pin-loaded plates was developed originally by Wilkenson, Rowlands, and Cook [47] and was later refined by Rahman et al. [48] to capitalize on the computational advantages that arise from the rigid pin assumption. This method uses three separate iteration steps to account for the incremental load level, the contact process, and the effects of friction. Both the original and refined schemes use displacement finite elements. In the load step iteration, the solution for a given load increment was treated as a linear analysis, i.e. the equations of linear elasticity were used. The stresses in the plate were computed for each given load level using the original undeformed configuration of the plate along with the final displacement vector.

The computation of contact stresses using displacement elements in the analysis of contact problems may create difficulties since the contact action frequently results in very large displacement gradients near the region of contact. Since the required stresses in a displacement model are generally computed at the element interiors and are then extrapolated to the contact boundary, some type of stress smoothing is often necessary using, for example, a local least squares routine [54] or iterative improvement on the averaged nodal stresses [55]. Using mixed elements, this is not necessary since the stresses are computed as nodal variables and no postcomputation is necessary to modify the resulting nodal stresses. It is for this reason that mixed elements would appear to be advantageous over displacement elements for contact problems since the stresses on the boundary are required for certain portions of the analysis.

The refined algorithm developed by Rahman [48] uses a mixed polar-Cartesian coordinate system to fix the proper displacements of the nodes of the plate that have come in contact with the circular pin. An iterative scheme is used to ensure that all nodes that have come in contact remain in contact for a given load step. In other words, after every iteration the positions of all contact nodes of the plate that have previously come in contact with the pin are corrected in the radial direction so that they remain on the surface of the pin, which is actually defined as a set of imaginary points that specify the region of no penetration. If the resulting shearing stress for a given contact node is larger than the induced radial stress multiplied by the nodal coefficient of friction, the node is considered to be sliding, and it may subsequently move in the tangential direction of the pin.

Otherwise, the node is considered to be sticking to the pin due to friction, and it is fixed to an interpolated position on the pin for the remainder of the analysis. This iterative procedure is repeated until the sum of the load steps has reached the required load level. The details of this method are more completely described in reference [48].

### 3.3 Elastic Pin Contact Algorithm

The assumption of a rigid pin, which is reasonable for cases when the two bodies in contact have a very large difference in modulus of elasticity, is not usually valid for contact between two generic bodies. The algorithm described in the previous section, though useful for certain problems, was mainly developed to demonstrate the use and accuracy of the mixed finite element method for the analysis of contact problems. For general problems involving arbitrary bodies, it is necessary to revise the analysis to include the effects of pin elasticity, which may be significant if the two bodies are of similar constitution. A second computational algorithm is described below for this more general type of contact problem.

#### 3.3.1 General Concepts

To account for the complications arising from contact and the presence of friction between two elastic bodies, we add a Lagrange multiplier contribution to our original expression in Eq. (2.28) which will represent the summation of the total potential of each of the contact forces acting at the nodes on the discretized contact boundary. In addition, the kinematics of the elements of the two bodies at the contact interface must be monitored such that the nodal displacements are compatible, i.e. the bodies must not overlap. We

therefore will eventually invoke stationarity of the modified functional

$$\Pi_C = \Pi_L - \sum_{i=1}^k W_i \quad (3.1)$$

where  $k$  represents the number of the contactor nodes on the boundary and  $W$  represents the total potential for a given contact force acting at a given contact node. This idea was originated and developed using a displacement formulation by Bathe and Chaudhary [36].

To determine the total potential for a contact force at a given contact node, we consider the local geometry of a contactor node  $K$  that will penetrate the target domain whose boundary is defined by the nodes  $A$  and  $B$  as shown in Figure 3.2. In our discussion, we will assume that the two bodies have been discretized using linear elements. Although the algorithm could be developed using higher-order elements, this somewhat complicates the analysis, and linear elements were used in this study because of their relative simplicity in many phases of the subsequent analysis. For our problem, we define the pin to be the contactor body and the plate to be the target body to remove the ambiguity of analyzing two elastic bodies. Only the nodes on the pin will be required to remain on or outside of the domain of the plate during the loading of the plate, while the nodes of the plate are allowed to be within the domain of the pin. This is a key assumption and requires some care when modeling the problem to ensure that all contactor nodes (i.e. contact nodes on the contactor body) are originally outside the target body.

In the formulation that follows, we assume that  $(i - 1)$  iterations have been performed in the quest for the equilibrium configuration  $C_2$  at time  $t + \Delta t$  for a given loading. During the last iteration  $(i-1)$ , the

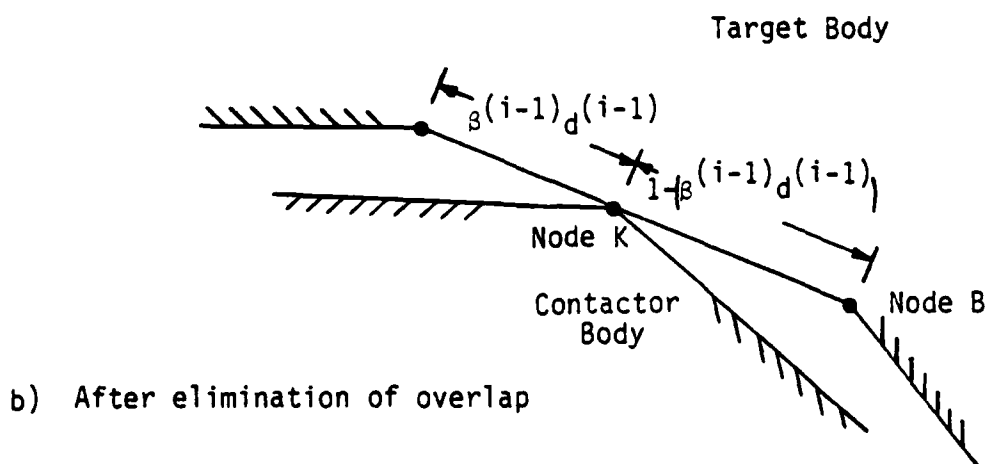
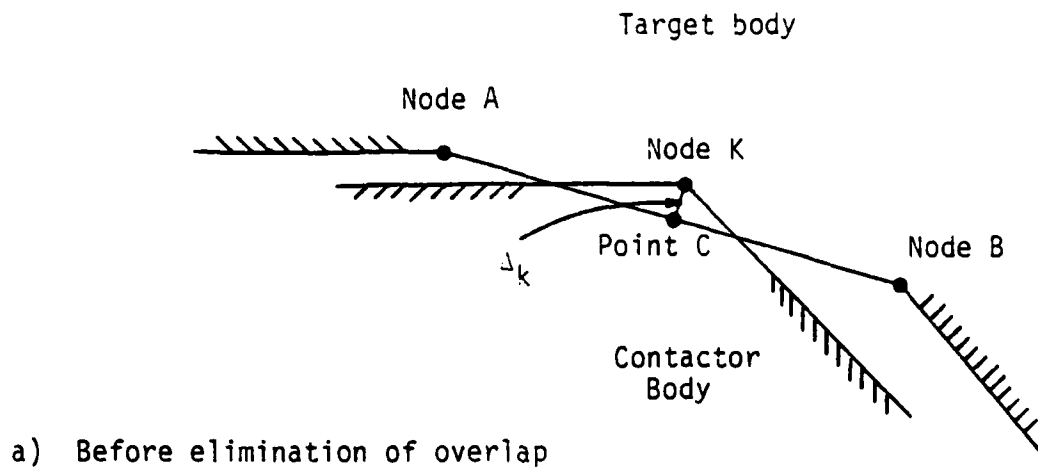


Figure 3.2 Local geometry of contactor node

displacements of the nodes K, B, and A have been such that the contactor node K has penetrated the domain of the plate a distance CK, where

$$CK = |CK| = \Delta_K \quad (3.2)$$

and

$$CK = \Delta_{Kx} \vec{i} + \Delta_{Ky} \vec{j} \quad (3.3)$$

The distance CK represents the minimum distance from the penetrated node K to the surface segment of the target body, which is defined as the line segment between the two nodes A and B of the target body.

The intermediate configuration defined by the updated Cartesian coordinates of the nodes after iteration (i - 1) is clearly not in an acceptable state of equilibrium since the contactor body has penetrated the target body at node K. This node must eventually lie exactly on the boundary of the plate, i.e. on the target segment defined by the nodes A and B, and its relative position  $\beta$  between nodes A and B must be a function of the coefficient of friction between the two bodies. In order for this to occur, the displacements of the nodes A, B, and K must be adjusted accordingly during the following iteration and a contact force must develop at the contactor node K as a result of the elimination of the overlap distance. We denote the latest estimate to this contact force at node K in configuration  $C_2$  as

$$2 \vec{\lambda}_K^{(i-1)} = \lambda_{Kx}^{(i-1)} \vec{i} + \lambda_{Ky}^{(i-1)} \vec{j} \quad (3.4)$$

This contact force is equal to zero after iteration (i - 1) and is developed as the overlap distance is eliminated during iteration (i).

Although the contact force acts alone at node K, it must be balanced by equivalent nodal forces at nodes A and B of the target segment. Imposing moment and force equilibrium on the discretized



target segment defined by the contactor node K and the target nodes A and B and solving these equations simultaneously gives the expressions for the target segment nodal forces as

$$\begin{aligned} 2_{\lambda_A}^*(i-1) &= - (1 - \beta^{(i-1)}) 2_{\lambda_K}^*(i-1) \\ 2_{\lambda_B}^*(i-1) &= - \beta^{(i-1)} 2_{\lambda_K}^*(i-1) \end{aligned} \quad (3.5)$$

As these nodal forces are generated, the displacement increments at the nodes A, B and K, which are given by  $\Delta u_A^{(i)}$ ,  $\Delta u_B^{(i)}$  and  $\Delta u_K^{(i)}$ , respectively, must occur such that the overlap distance CK is eliminated during iteration (i). Hence, the total potential of the contact force at node K may be written as

$$\begin{aligned} W_k &= \{2_{\lambda_K}^*(i)\}^T \{\Delta u_K^{(i)}\} + \{2_{\lambda_K}^*(i)\}^T \{\Delta_K^{(i-1)}\} \\ &+ \{2_{\lambda_A}^*(i)\}^T \{\Delta u_A^{(i)}\} + \{2_{\lambda_B}^*(i)\}^T \{\Delta u_B^{(i)}\} \end{aligned} \quad (3.6)$$

where the first term is due to the contactor body and the remaining three terms are due to the target body.

Since the contact force is originally equal to zero and is developed during the elimination of the overlap distance, we may write the incremental decomposition of the contact force at node K as

$$2_{\lambda_K}^*(i) = 2_{\lambda_K}^*(i-1) + \Delta \lambda_K^*(i) \quad (3.7)$$

We note that if the two bodies are in sticking contact, the contact force components may be written as in Eq. (3.4). However, if the bodies in contact are sliding, the contact force component increment in the direction tangent to the target segment is equal to zero, or

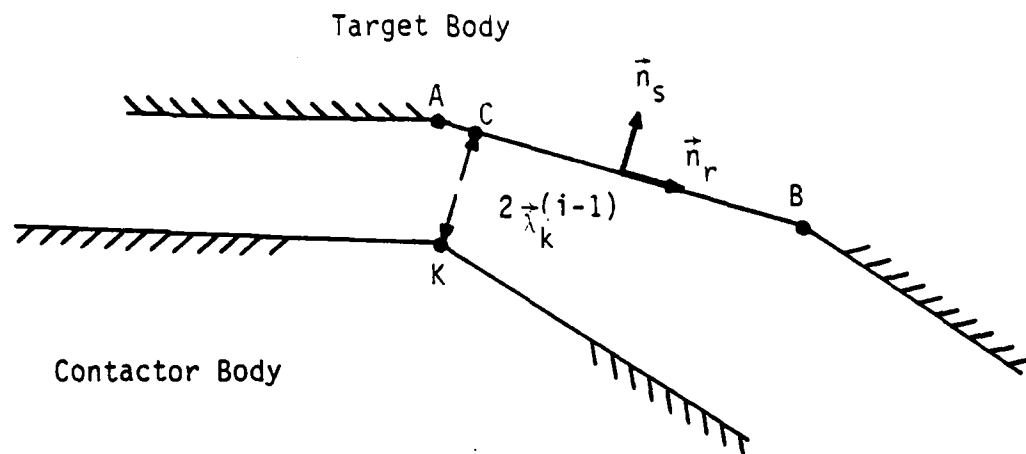
$$\Delta \vec{\lambda}_K^{(i)} = -\Delta \lambda_S^{(i)} \vec{n}_S \quad (3.8)$$

where  $\vec{n}_S$  is the unit vector acting normal to the target segment as shown in Figure 3.3. This expression is true because  $\Delta \lambda_S$  acts as a workless constraint force and only the normal contact force component may act in eliminating the overlap distance. In addition, the value of  $\beta$  will change during the iteration due to the relative slip between the two bodies. This value change is assumed to be negligible for each iteration.

In order to impose stationarity on the contact functional  $\pi_C$ , we need the first variation of  $W_K$ . Using the Equations (3.5)-(3.7), we may write the first variation of the total potential of the contactor node K due to sticking contact as

$$\begin{aligned} -\delta W_K = & -\{2_{\lambda_K}^{(i)}\}^T \{\delta \Delta u_K^{(i)}\} + (1 - \beta^{(i-1)}) \{2_{\lambda_K}^{(i)}\}^T \{\delta \Delta u_A^{(i)}\} \\ & + \beta^{(i-1)} \{2_{\lambda_K}^{(i)}\}^T \{\delta \Delta u_B^{(i)}\} - \{\Delta \lambda_K^{(i)}\}^T \{\delta \Delta u_K^{(i)}\} \\ & + (1 - \beta^{(i-1)}) \{\Delta \lambda_K^{(i)}\}^T \{\delta \Delta u_A^{(i)}\} + \beta^{(i-1)} \{\Delta \lambda_K^{(i)}\}^T \{\delta \Delta u_B^{(i)}\} \\ & - \{\delta \Delta \lambda_K^{(i)}\}^T \{\Delta u_K^{(i)}\} - \{\delta \Delta \lambda_K^{(i)}\}^T \{\Delta u_K^{(i-1)}\} \\ & - (1 - \beta^{(i-1)}) \{\delta \Delta \lambda_K^{(i)}\}^T \{\Delta u_A^{(i)}\} + \beta^{(i-1)} \{\delta \Delta \lambda_K^{(i)}\}^T \{\Delta u_B^{(i)}\} \end{aligned} \quad (3.9)$$

where the vector notation has been used to imply that the x and y components of the terms given within the braces are represented and the T superscript represents the transpose of the vector. We note that only the displacement increments and the contact force increments are allowed to vary, but the contact force components and the overlap distance components are fixed scalar quantities.



Note: The bodies are apart only for illustrative purposes.  
Points K and C actually coincide.

Figure 3.3 Direction of developed contact force after elimination of overlap

Similarly, we may write the components of the target segment unit normal vector as

$$\vec{n}_s = n_{sx}\vec{i} + n_{sy}\vec{j} \quad (3.10)$$

and using Eqs. (3.5)-(3.6) and Eq. (3.8) we may write the expression for the first variation of the total potential for the contact force at node K due to sliding contact as

$$\begin{aligned} -\delta W_K = & -\{^2\lambda_K^{(i-1)}\}^T \{\delta\Delta u_K^{(i)}\} + (1 - \beta^{(i-1)}) \{^2\lambda_K^{(i-1)}\}^T \{\delta\Delta u_A^{(i)}\} \\ & + \beta^{(i-1)} \{^2\lambda_K^{(i-1)}\}^T \{\delta\Delta u_B^{(i)}\} + \Delta\lambda_s^{(i)} n_{sx} \delta\Delta u_{Kx}^{(i)} + \Delta\lambda_s^{(i)} n_{sy} \delta\Delta u_{Ky}^{(i)} \\ & - (1 - \beta^{(i-1)}) \Delta\lambda_s^{(i)} n_{sx} \delta\Delta u_{Ax}^{(i)} - (1 - \beta^{(i-1)}) \Delta\lambda_s^{(i)} n_{sy} \delta\Delta u_{Ay}^{(i)} \\ & - \beta^{(i-1)} \Delta\lambda_s^{(i)} n_{sx} \delta\Delta u_{Bx}^{(i)} - \beta^{(i-1)} \Delta\lambda_s^{(i)} n_{sy} \delta\Delta u_{By}^{(i)} \\ & - \delta\Delta\lambda_s^{(i)} [-n_{sx} \Delta u_{Kx}^{(i)} - n_{sy} \Delta u_{Ky}^{(i)} - n_{sx} \Delta_{Kx}^{(i-1)} - n_{sy} \Delta_{Ky}^{(i-1)} \\ & + (1 - \beta^{(i-1)}) n_{sx} \Delta u_{Ax}^{(i)} + (1 - \beta^{(i-1)}) n_{sy} \Delta u_{Ay}^{(i)} + n_{sx} \beta^{(i-1)} \Delta u_{Bx}^{(i)} \\ & + n_{sy} \beta^{(i-1)} \Delta u_{By}^{(i)}] \quad (3.11) \end{aligned}$$

Here we have written out the components of the terms involving the contact force increments to aid in showing the origin of the terms in the sliding contact matrix and force vector. These are developed in the following section.

### 3.3.2 Finite Element Matrices

Our ultimate objective in constructing the total potential of each of the contact forces is to impose stationarity on the modified functional in Eq. (3.1) with respect to the displacement, stress, and contact force component increments. Hence, we must separate the

coefficients of the variations in the contact force increments and the displacement increments of nodes A, B, and K for the expressions in Eq. (3.9) and Eq. (3.11). The resulting contact equations can then be written in matrix form as

$$\begin{aligned}
 -\delta W_k = & \left( \begin{bmatrix} \{\delta \Delta U^{(i)}\}^T & \{0\} \\ \{0\} & \{\delta \Delta \lambda^{(i)}\}^T \end{bmatrix} + \begin{bmatrix} [0] & [K_C^{13}] \\ [K_C^{13}]^T & [K_C^{33}] \end{bmatrix} \right) \begin{Bmatrix} \{\Delta U^{(i)}\} \\ \{\Delta \lambda^{(i)}\} \end{Bmatrix} \\
 & - \begin{Bmatrix} \{^2 R_C^{(i-1)}\} \\ \{^2 \Delta_C^{(i-1)}\} \end{Bmatrix} \quad (3.12)
 \end{aligned}$$

where the entries of the  $[K_C^{13}]$  and  $[K_C^{33}]$  matrices and the contact force vector  $\{^2 R_C^{(i-1)}\}$  for the cases of sliding and sticking contact are given in the Appendix. These components are then added to the existing finite element matrices resulting from the stationarity of  $\Pi_R$  (see Section 2). Performing this step allows us to write the final finite element matrix representation of the stationary constraint imposed on the modified functional expressed in Eq. (3.1):

$$\begin{aligned}
 & \left( \begin{bmatrix} [K^{11}] & [K^{12}] & [0] \\ [K^{12}]^T & [K^{22}] & [0] \\ [0] & [0] & [0] \end{bmatrix} + \begin{bmatrix} [0] & [0] & [K_C^{13}] \\ [0] & [0] & [0] \\ [K_C^{13}]^T & [0] & [K_C^{33}] \end{bmatrix} \right) \begin{Bmatrix} \{\Delta U^{(i)}\} \\ \{S^{(i)}\} \\ \{\Delta \lambda^{(i)}\} \end{Bmatrix} \\
 & = \begin{Bmatrix} \{^2 R\} \\ \{0\} \\ \{0\} \end{Bmatrix} - \begin{Bmatrix} \{^2 F^{(i-1)}\} \\ \{0\} \\ \{0\} \end{Bmatrix} + \begin{Bmatrix} \{^2 R_C^{(i-1)}\} \\ \{0\} \\ \{t+\Delta t, \Delta_C^{(i-1)}\} \end{Bmatrix} \quad (3.13)
 \end{aligned}$$

The nature of the contact matrices will depend on the state of stick or slip between each contactor node and its corresponding target segment, and the contact matrix and contact force vector must represent

this current state. The entries in the contact matrices and force vectors are shown to be added to the standard mixed finite element stiffness matrix of a typical element in Eq. (3.13) as a matter of convenience. It should be understood that the constraint equations were derived for a generic contact node and its target segment, and the contact matrix and contact force vector entries must only be added to the existing values corresponding to the proper global degree's of freedom of the standard stiffness matrix for these contactor and target segment nodes.

Once the proper contact matrix and contact force vector corresponding to stick or slip for each of the contactor nodes have been added to the global finite element matrix and total force vector, the solution procedure is similar to that of the standard nonlinear analysis. The global system of equations is solved repeatedly for the increments in the displacements, stresses, and contact forces until the Euclidean norm of the incremental solution vector and/or the total force vector are within a preassigned tolerance. During the iterations, the entries in the contact matrices and the contact force vectors are updated to reflect the most current state of the geometry and loading. Once the solution has converged, another load increment may be applied or the analysis may be terminated.

#### 3.3.4 Determination of Stick and Slip

An important facet of the analysis is the determination of the state of stick or slip between each of the contact nodes and their corresponding target regions after each iteration. This step indicates whether the sliding or sticking contact matrices should be imposed for the next iteration. In Reference [36], which uses a displacement

formulation, the total distributed tractions along the contactor elements are computed after several intermediate steps and are compared to determine the state of stick or slip for a given element. Using the mixed formulation, this part of the analysis is simplified considerably since the state of stress is known precisely at the nodes and hence may be computed for each contactor node rather than for an element side. Using the stress transformation equations along with the relative angle (with respect to the fixed Cartesian reference frame) of the target edge of the target segment, the normal stress component  $\sigma_n$  and the shearing stress component  $\tau_{nt}$  may be computed for each of the contact nodes. Clearly, if the two bodies are in contact, the normal stress component of the contact node acting on the target body should be compressive. If we designate the static or dynamic coefficient of friction as  $\mu$ , we say that if, for a given contactor node,

$$|\tau_{nt}| > \mu |\sigma_n| \quad (3.14)$$

then the node is in sliding contact, and if

$$\mu |\sigma_n| \geq |\tau_{nt}| \quad (3.15)$$

then the node is in sticking contact. It should be noted that these expressions are the computational equations used to determine the state of stick or slip for a given node. Physically, however, Eq. (3.14) would be an equality since the node begins to slide as soon as the tangential stress just exceeds the frictional capacity of the node. Equation (3.15) would then be changed to a strict inequality. This physical situation is a very minor factor, however, since this bifurcation point would rarely be realized computationally.

Specifying  $\mu$  to be the static or dynamic coefficient of friction in these equations will depend on if the node was sliding or sticking

during the previous iteration. This comparison is made for all nodes in contact after each iteration, and the correct contact matrix is implemented for the next iteration. Since the state of stress is not known for the first iteration after the nodes have come in contact, the state of sticking contact was assumed so that a non-recoverable tangential displacement was avoided.

### 3.3.5 The Computation of Contact Forces

In the case of sticking contact, the increments in the contact force vector components are both nonzero since a force may develop in both the normal and tangential directions of contact along the target segment due to the two bodies sticking together. In the case of sliding contact, the only nonzero incremental contact force component is that in the direction normal to the target segment, which is automatically accounted for by the contact matrices given in Eq. (3.13). However, there is also a force component that opposes the relative tangential motion of the contactor node due to the presence of friction acting along the target segment containing the contactor node. Although this force component does not exist for frictionless problems, meaning that the sliding contact matrices may be imposed for all iterations with no corrections, this is not true in general. This section addresses the issue of the computation of these tangential forces that must be applied to the contactor nodes with nonzero coefficients of friction that are in sliding contact along their corresponding target segments for a given iteration.

According to the criteria given in Section 3.2.4 to determine the state of stick or slip for a given contactor node, we observe that there are four possible combinations of stick and slip for the triplet of



nodes neighboring and including the contactor node K. These four cases are shown in Figure 3.4. The first and fourth cases are relatively simple to handle computationally. In case 1, all three of the nodes are in sticking contact, and there are no additional force contributions due to friction resistance since the nodes do not slide. In case 4, where all nodes are sliding, the only forces that need be applied in the tangential directions are those due to friction. To compute these forces, we need to compute the tangential tractions acting on the contactor segment that corresponds to the total frictional capacity. This step must be performed for each of the two contactor segments.

To do this, we must first compute the normal and tangential surface tractions using the nodal stress values computed during the previous iteration, along with the equations

$$\begin{aligned} t_n &= \sigma_{nn}n_n + \tau_{nt}n_t \\ t_t &= \tau_{nt}n_n + \sigma_{tt}n_t \end{aligned} \quad (3.16)$$

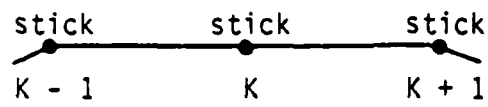
For segment 1, which contains two sliding nodes, the tangential surface traction is given by

$$t_t^* = \frac{\mu^{K-1}}{2} t_n^{K-1} + \frac{\mu^K}{2} t_n^K \quad (3.17)$$

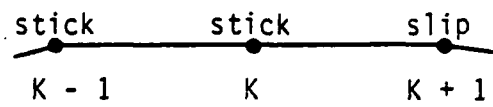
where the subscripts t and n indicate the tangential and normal directions, respectively, and  $\mu^i$  is the static or dynamic coefficient of friction at node i, depending on if the node was in sticking or sliding contact during the previous iteration. To compute the tangential force corresponding to these surface tractions, we use the formula for the equivalent nodal force given for plane elasticity problems as

$$F_{t_i} = \oint_S t_t^* \psi_i ds \quad (3.18)$$

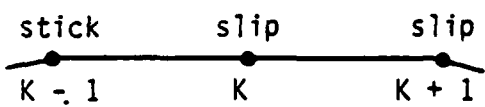
where S represents the boundary of the given element. Since we are



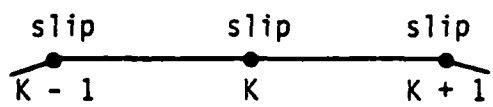
a) Case 1



b) Case 2



c) Case 3



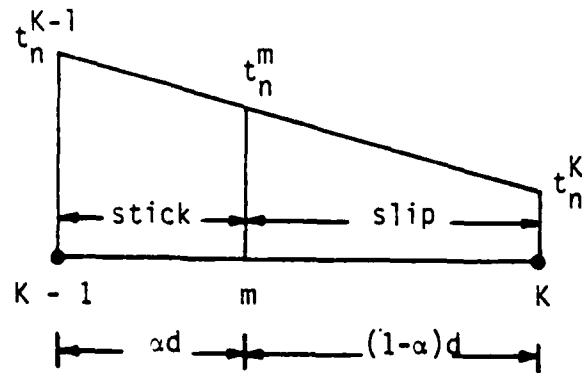
d) Case 4

Figure 3.4 Possible combinations of nodal stick and slip

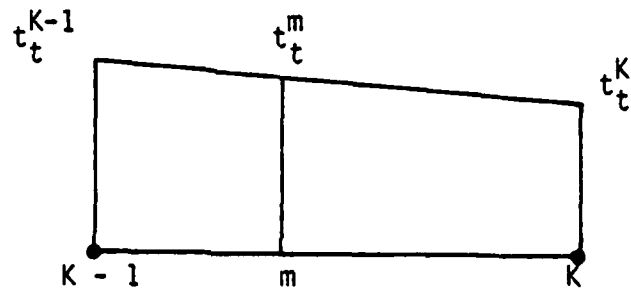
working with linear elements, the frictional force corresponding to the modified tangential traction  $t_t^*$ , which in this case is constant along the segment, will be divided evenly between the two nodes of the segment. This procedure is repeated for the second contactor segment, which borders the contactor node K on the opposite side, and the total summed force of these two frictional force components is applied to the contactor node K as an external load for the next iteration.

The remaining possible cases involve a contactor segment with one node sticking and one node sliding. If the neighboring segment is completely slipping (case 2) or sticking (case 3), the contact forces for this segment only are computed using the procedures described previously for the first and fourth cases. Hence the remaining case that we need to concern ourselves with is the situation shown in Figure 3.5. Clearly, the basic problem involves accounting for the transition between the zones of stick and slip, including the computation of the tangential contact force due to the appropriate tractions along the segment between the sticking node and the sliding node.

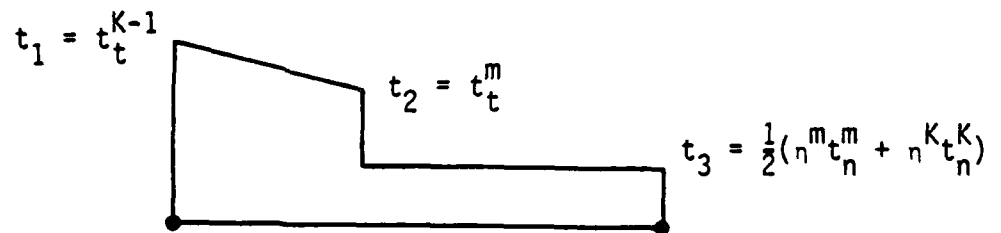
In order to determine the force due to friction along a segment acting on the sliding node, we first need to determine how much of the element segment is in sliding contact and how much is in sticking contact. For the sticking node, the frictional capacity of the node exceeds the corresponding shear stress, while this inequality is reversed for the sliding node. Since linear elements are being used, we assume that the frictional capacity and the shearing stress both vary linearly along the contactor segment. Hence there is a point  $m$  whose position is defined by the parameter  $\alpha$ , which denotes the point of transition between the zones of sticking and sliding contact. Using the



a) Normal surface tractions



b) Tangential surface tractions



c) Modified tangential surface tractions

Figure 3.5 Surface tractions for element side with sections of stick and slip

assumption of linear stress variation and similar triangles allows us to compute the value  $\alpha$  as

$$\alpha = \frac{(\mu|\sigma_{nn}| - \tau_{nt})^{K-1}}{(\mu|\sigma_{nn}| - \tau_{nt})^{K-1} + (\tau_{nt} - \mu|\sigma_{nn}|)^K} \quad (3.19)$$

where the superscripts outside the parentheses indicate the node at which the enclosed quantities are measured. Since the terms computed within the parentheses are all positive, the value of  $\alpha$  must be between zero and one.

Using  $\alpha$  to define the transition point, we next modify the tangential surface tractions to account for the portion of the contactor segment that is sliding. We note that the normal tractions are not changed since they do not explicitly depend on the state of stick or slip. At the transition point, the tangential traction is reduced to the value  $t_m^*$ , where

$$t_m^* = \frac{\mu^m t_n^m}{2} + \frac{\mu^k t_n^k}{2} \quad (3.20)$$

where  $m$  represents the transition point. The values of the tangential tractions in the sticking regions remain the same as computed using the nodal stress values. Using this equation and the modified values given in Figure 3.5, we may write the final distribution of the tangential traction  $t$  as a function of the length along the segment, denoted by  $x$ , as

$$t = \begin{cases} \left(\frac{t_2 - t_1}{ad}\right)x + t_1 & \text{if } 0 \leq x \leq ad \\ t_3 & \text{if } ad < x \leq d \end{cases} \quad (3.21)$$

where the values of  $t_1$ ,  $t_2$ , and  $t_3$  are given in Figure 3.5.

To compute the equivalent nodal forces corresponding to these tractions, we use Eq. (3.21) and substitute in the value of  $t$  given by Eq. (3.18) for  $t_t^*$ . The tangential traction is no longer a constant across the length of the contactor segment, and the force will no longer be divided evenly among the two nodes of the contactor segment. Performing the required integrations yields the desired tangential force components for the contactor nodes  $K - 1$  and  $K$  as

$$F_{K-1} = t_1 \alpha d \left( \frac{1}{2} - \frac{\alpha}{6} \right) + t_2 \alpha d \left( \frac{1}{2} - \frac{\alpha}{3} \right) + t_3 d \left[ \frac{1}{2} + \alpha \left( \frac{\alpha}{2} - 1 \right) \right] \quad (3.22)$$

$$F_K = t_1 \frac{\alpha^2 d}{6} + t_2 \frac{\alpha^2 d}{3} + t_3 d \left( \frac{1}{2} - \frac{\alpha d}{2} \right)$$

The component of force  $F_{K-1}$  is already incorporated into the contact force acting at node  $K - 1$  as part of the analysis. The magnitude of the force  $F_K$ , however, must be added to the tangential contact force at node  $K$  computed from the tractions acting on segment 2. This second force is equal to zero if the node  $K + 1$  is not in contact, and is computed using Eq. (3.17) if the node  $K + 1$  is in sliding contact.

As in the case of computing the state of stick or slip for a given contact node, it is evident that having stress as a nodal variable is quite advantageous. The normal and tangential surface tractions may be readily computed using the nodal stress values instead of using the nodal contact forces or other techniques to compute these quantities.

## 4. A HYBRID NUMERICAL/EXPERIMENTAL TECHNIQUE

### 4.1 Introduction

The primary difficulty in the numerical analysis of contact problems is the lack of knowledge regarding the region of contact and the state of stick or slip between the two bodies. If the regions of contact and the state of stick or slip are known for a given load level, the analysis is greatly simplified. A hybrid experimental/numerical technique is presented in this section that combines the experimental technique of moire interferometry with the numerical finite element method to form a hybrid technique. The new method uses the advantages of each of the two separate methods to create an accurate and powerful tool of analysis.

In this section, the basic concepts of moire interferometry, the experimental portion of the hybrid technique, are presented. The details of the hybrid technique are discussed, and the geometric and material properties of the physical specimens and the finite element models are given in preparation of the presentation of the numerical results given in the following section.

### 4.2 Moire Interferometry

A search for the origins of the French word "moire" would lead to a fabric known as watered silk, which displays varying patterns of light and dark bands. For this reason, the so-called moire effect occurs whenever two similar but not identical arrays of lines or dots are arranged such that one array can be viewed through the other [56]. Moire methods have been used in the field of solid mechanics for several decades to analyze deformed bodies. During recent years, the sensitivity of these methods has been improved dramatically.

Moire interferometry is an experimental technique which may be used in solid mechanics problems to measure in-plane displacements of deformable bodies under external action. The method is unique in that it is not dependent upon the geometrical or material nonlinearities of the specimen under analysis. All moire techniques use two bar-and-space gratings, one as a reference and one that is attached to the specimen. As the specimen is deformed, the specimen grating deforms along with it, and a contour map of moire fringes is formed due to the deformed specimen grating contrasting with the undeformed reference grating. Since the displacements in a given direction are directly proportional to the fringe order, the corresponding displacements may be computed by the analyst by counting the number of fringes on the contour map. Stresses may then be calculated using the gradients of the displacements and an assumed constitutive model, though this can become quite tedious and is not as accurate as the displacements themselves.

Moire interferometry provides the required sensitivity that is needed to accurately measure the small in-plane displacements of the two-dimensional pin-loaded plate contact problem. In particular, this method provides valuable information on the state of the displacements (not stresses) at the interface boundary between the pin and the plate. This eliminates the need for theoretical assumption on exactly what is occurring at the contact boundary that is so common in most numerical simulations of this problem. As mentioned previously, it is the complex state of contact, stick, and slip that makes this problem so difficult to model numerically, and the use of an experimental technique to determine the contact conditions greatly simplifies the computational effort.



Only the salient features of moire interferometry have been discussed in this section, and interested readers are urged to consult the more detailed references by Post [57-59].

#### 4.3 The Hybrid Technique

The two basic components of the hybrid technique are the nonlinear mixed finite element method and moire interferometry. By far, the more demanding portion of the hybrid technique is the experimental portion of the analysis. Although not discussed in this study, the experimental details of the hybrid technique will be reported by Joh [60]. Despite the effort required to obtain accurate experimental data and the relatively large computational time involved in the finite element analysis, the steps involved in the execution of the hybrid method are quite simple in concept and are outlined as follows.

The exact displacements around the hole boundary of a physical specimen may be measured for a sequence of increasing load steps using moire interferometry. These displacement increments, along with the loads applied to the plate, are input as a sequence of nonhomogeneous boundary conditions for the simulated problem analyzed by the nonlinear mixed finite element model. These steps can be represented mathematically by considering the global finite element matrix of the plate written in partitioned form as

$$\begin{bmatrix} [K^{11}] & [K^{12}] & [K^{13}] \\ [K^{12}]^T & [K^{22}] & [K^{23}] \\ [K^{13}]^T & [K^{23}]^T & [K^{33}] \end{bmatrix} \begin{Bmatrix} \{u_1\} \\ \{u_2\} \\ \{\Delta\} \end{Bmatrix} = \begin{Bmatrix} \{F^1\} \\ \{F^2\} \\ \{F^3\} \end{Bmatrix} \quad (4.1)$$

where the vector  $\{u_1\}$  contains the degrees of freedom corresponding to known zero displacements (for example, along lines of symmetry of the plate),  $\{u_2\}$  contains the degrees of freedom corresponding to the nodes

of the plate that are in contact with the pin, and  $\{\Delta\}$  contains the degrees of freedom corresponding to the remaining unknown nodal displacements and stresses throughout the domain of the plate.

The imposition of known boundary conditions on the global finite element matrix is a relatively straightforward task and only the major points will be described here. Further details of this procedure may be found in any textbook on structural analysis or the finite element method (e.g. see [11]). The specification of homogeneous boundary conditions, or in this case the known zero displacements, results in the modification of Eq. (4.1) which may then be written as

$$\begin{bmatrix} [I] & [0] & [0] \\ [0] & [K^{22}] & [K^{23}] \\ [0] & [K^{23}]^T & [K^{33}] \end{bmatrix} \begin{Bmatrix} \{u_1\} \\ \{u_2\} \\ \{\Delta\} \end{Bmatrix} = \begin{Bmatrix} \{0\} \\ \{F^2\} \\ \{F^3\} \end{Bmatrix} \quad (4.2)$$

where  $[I]$  and  $[0]$  represent the identity matrix and the null matrix, respectively, and  $\{0\}$  is the null vector. This step is typically performed in all analyses of the plate regardless of whether a hybrid technique or a numerical technique is being used in order to remove the rigid body motion of the plate and to account for the symmetry of the structure. The primary difficulty in the execution of the numerical contact algorithms described in section 3 is the determination of the vector  $\{u_2\}$  for a given load step such that there is no penetration between the nodes of the pin and the plate and that the regions of stick and slip are accounted for. Hence in a strict computational contact algorithm the vector  $\{u_2\}$  is solved for in an iterative fashion for a given load step. Each iteration involves significant computation in order to eventually obtain a solution to the problem.

In the hybrid technique, the vector  $\{u_2\}$  is given by the experimental technique and contains the true displacements of the plate boundary as it has come in contact with the pin. Imposing the known displacement boundary conditions on the global system of equations is slightly more complicated than the procedure described in Eq. (4.2) for the homogeneous boundary conditions since the specified displacements are no longer equal to zero and hence have an effect on the remaining equations of the system. The force vector must therefore be modified to reflect this condition. If the vector  $\{\hat{u}_2\}$  represents the known displacement of the contact nodes around the boundary of the plate determined by the experimental technique, then the modified global matrix equation after imposition of all boundary conditions may be written as

$$\begin{bmatrix} [I] & [0] & [0] \\ [0] & [I] & [0] \\ [0] & [0] & [K^{33}] \end{bmatrix} \begin{Bmatrix} \{u_1\} \\ \{u_2\} \\ \{\Delta\} \end{Bmatrix} = \begin{Bmatrix} \{0\} \\ \{\hat{u}_2\} \\ \{\hat{F}^3\} \end{Bmatrix} \quad (4.3)$$

We note that the remaining force vector has been modified to account for the nonzero specified displacements. The components of this vector may be written as

$$\hat{F}_i^3 = F_i^3 - K_{ij}^{33} \hat{u}_2^j \quad (4.4)$$

where the indicial subscripts and superscripts indicate the appropriate vector or matrix entries. Solving the modified matrix equation in Eq. (4.3) will result in the correct boundary displacements as well as the corresponding displacements and stresses throughout the rest of the plate.

Since the solution of the incremental displacement and stress vector is an iterative process, the vector  $\{\hat{u}_2\}$  is nonzero only for the first iteration of the solution procedure for the given load step, and is specified to be zero for the subsequent iterations. Hence for a given load step, the prescribed contact boundary displacements are applied to the plate along with the appropriate force vector resulting from the uniform, in-plane load that is applied to the plate. The nonzero displacements throughout the rest of the plate along with all nodal stresses are then solved for using Eq. (2.40) until acceptable convergence criteria have been met. As in the case of the rigid pin algorithm described in Section 3.2, the pin is completely eliminated from the finite element analysis and therefore only the domain of the plate is discretized and analyzed.

The only approximations involved in this technique are those due to the physical and mathematical limitations of moire interferometry and the finite element method. The numerically solved problem is simply a special boundary-value problem with specified displacements, and no other assumptions are involved.

Since, in theory, the one half of the plate acts as the mirror image of the other half of the plate, only one half of the plate domain is modeled for the finite element analysis. This will significantly reduce the computational time involved. Experimental data have shown that the displacements around the hole of the plate are not exactly symmetric, even for an isotropic material. This is most probably due to the limitations of creating a perfectly symmetric specimen and applying a perfectly symmetric load. The displacements are therefore averaged in both of the coordinate directions of the plate to yield one pair of

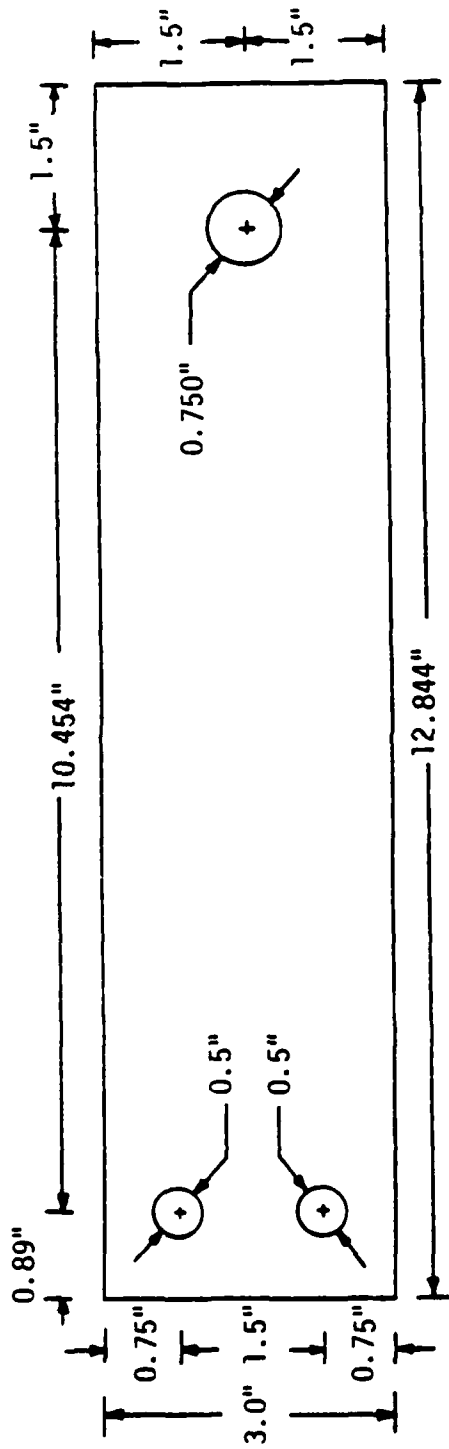
displacement values for a given point of the contact boundary for the modeled half of the plate.

#### 4.4 Description of the Plate

In this section the physical dimensions and material properties are given for the plate and the pin used in the experimental portion of the hybrid technique. Also given are the different finite element meshes used in the numerical portion of the analysis of the plate.

A diagram of the plate used in the experiments performed to determine the boundary displacements between the plate and the pin is shown along with the dimensions used in Figure 4.1. The plate and the pin were both constructed of 7075-T6 aluminum ( $E = 10,400$  ksi and  $\nu = 0.33$ ). The thickness of the plate was taken to be 0.061 inches. The restraining pin, with a radius of 0.3745 inches, was fixed to a structure exterior to the plate and hence its center did not deform except for a very small displacement due to the bending of the pin fixture. The plate was loaded by means of pins passing through the two 0.5 inch diameter holes.

Several assumptions were made in the finite element modeling of the plate domain for use in the hybrid technique. The assumption of symmetry was used along the length of the plate in order to reduce the total number of degrees of freedom of the problem, thereby reducing the cost of the finite element analysis. In addition, St. Venants principle was invoked near the loaded end of the plate to eliminate the localized effects of the pins loading the plate. Hence only the first 8.5 inches of the plate were discretized, and the applied load was assumed to act as a uniform in-plane load to the shortened end of the plate (i.e. the left end of the plate in Figure 4.1).



Radius of plate hole = 0.375"

Radius of pin = 0.3745"

Thickness of plate = 0.061"

Figure 4.1 Physical dimensions of experimental pin/plate specimen

Several different mesh configurations were used in the finite element analysis in order to determine the effect of element size and approximation order and also to compare results for a variety of domain and variable approximations. The first mesh used is shown in Figure 4.2 and contains 191 linear isoparametric elements and 228 nodes, representing 1140 total degrees of freedom. As indicated by the type of element used to approximate the geometry, both stresses and displacements were assumed to vary linearly in the finite element approximations. Since the inner boundary of the plate is circular, the use of linear elements introduces some domain approximation error into the solution for this mesh and any other mesh constructed of linear elements.

The second finite element mesh used to model the plate was constructed of quadratic elements and is shown in Figure 4.3. The use of quadratic elements minimizes the domain approximation error in the analysis of this problem. This second mesh contains 104 elements and 367 nodes, which corresponds to 1835 total degrees of freedom. Although the quadratic elements do represent an improvement over linear elements in terms of modeling the circular boundary of the plate, their use does tend to increase the bandwidth of the global finite element matrix, and hence the computational effort.

The nodes of both finite element meshes used in this example were renumbered using the Cuthill-McKee ordering strategy [65] to reduce the size of the bandwidth and thereby decrease the cost of the analysis. As mentioned in Section 2, the nodes must still be numbered such that the first node has specified (zero or nonzero) displacements. Several different contact nodes were selected as the initial node in the

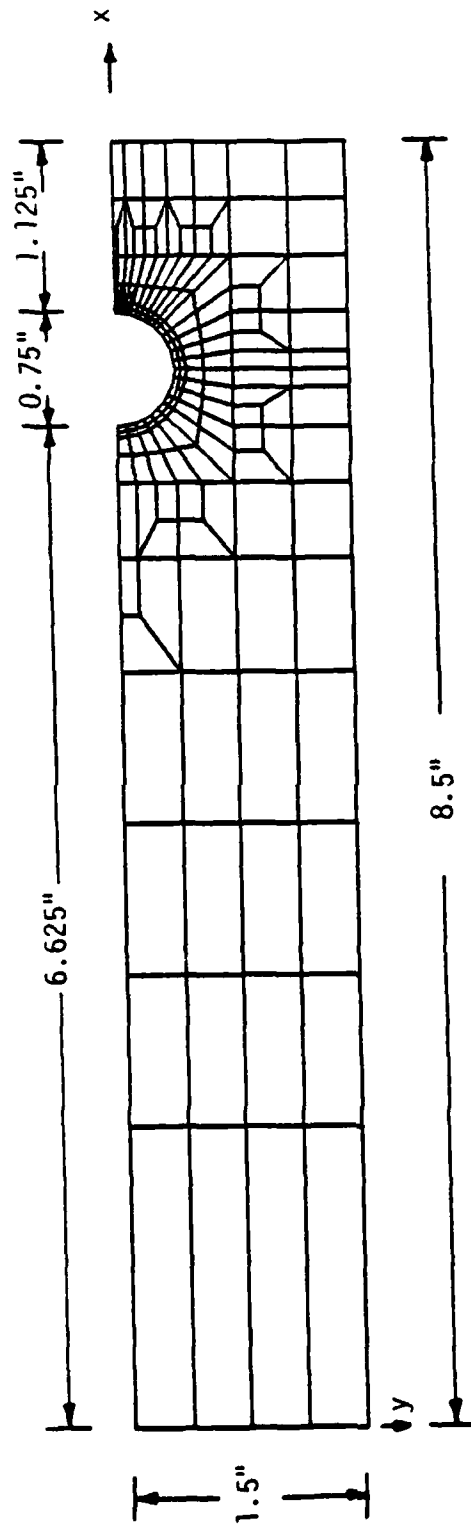


Figure 4.2 Finite element model of plate for hybrid technique using linear elements



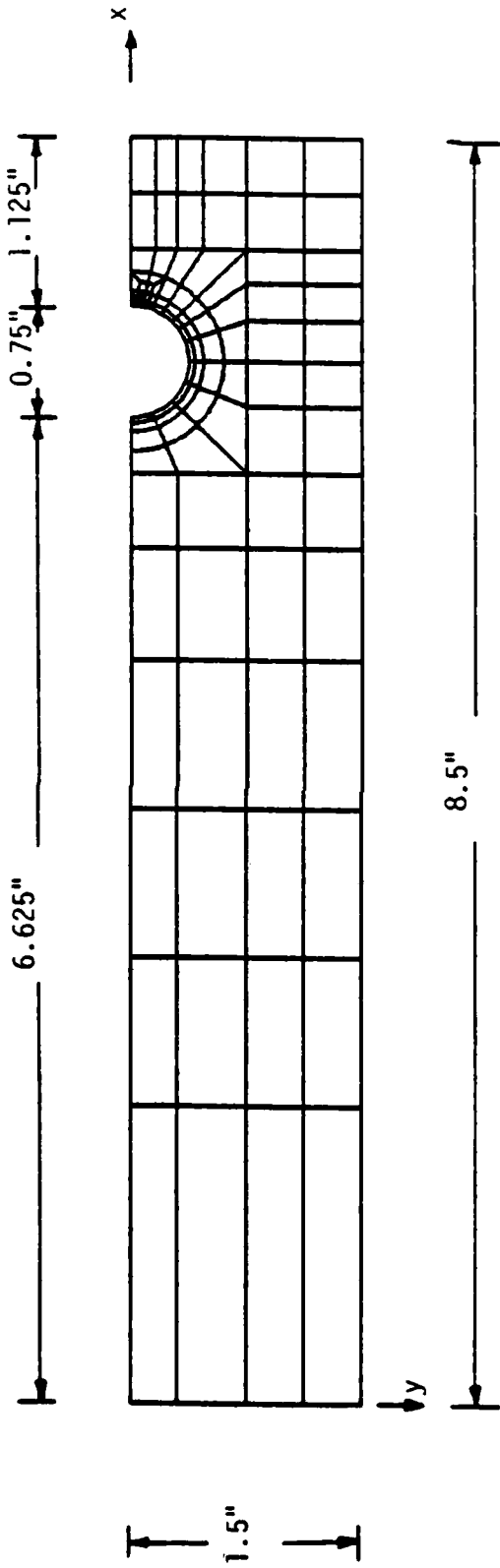


Figure 4.3 Finite element model of plate for hybrid technique using quadratic elements

renumbering scheme and it was found that selecting the node of initial contact (i.e. the node at  $x = 7.375$  and  $y = 0.0$ ) gave the node numbering with the smallest resulting corresponding bandwidth.

The displacements around the boundary of the hole obtained by moire interferometry are eventually expressed in Cartesian components as a function of the angular position around the inside of the hole. The displacements were given every 0.5 degrees for each load step. In order to retain as much of the accuracy of these displacements as was possible, the contact nodes of the plate were located exactly at a point where the experimental displacements were computed, i.e. on the degree or half-degree. Due to the storage restrictions of the finite element model, only a finite number of nodes could be specified on the plate boundary, which necessitated ignoring many of the data points from the experimental analysis. Hence for the half-plate model, the contact nodes of the linear element mesh were located at the following (degree) locations: 0.0, 1.0, 2.0, 4.0, 6.0, 8.0, 10.0, 12.5, 15.0, 20.0, 25.0, 30.0, 35.0, 40.0, 45.0, 54.0, 63.0, 72.0, 90.0, 99.0, 108.0, 117.0, 126.0, 135.0, 144.0, 153.0, 162.0, 171.0, and 180.0. In an attempt to incorporate some of the different data point displacements and to determine if this change affected the resulting stress distributions, the nodes for the quadratic element mesh were placed at slightly different locations: 0.0, 1.5, 3.0, 4.5, 6.0, 7.5, 9.0, 10.5, 12.0, 14.0, 16.0, 19.0, 22.0, 27.0, 32.0, 38.5, 45.0, 50.0, 55.0, 62.5, 70.0, 80.0, 90.0, 101.0, 112.0, 123.5, 135.0, 146.5, 158.0, 169.0, and 180.0.

## 5. NUMERICAL EXAMPLES AND RESULTS

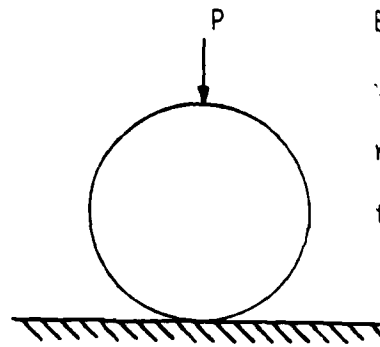
### 5.1 Introduction

In this chapter, the results are presented for a number of numerical examples to demonstrate the accuracy and efficiency of the methods described in the previous sections. The next three sections contain results for several elastic contact problems, and in particular the pin-loaded plate problem, using the rigid pin algorithm, the elastic pin algorithm, and the hybrid experimental/numerical technique.

It is again emphasized that all of the contact algorithms contain the nonlinear mixed formulation described in Section 2 as a foundation, and the only procedures that vary in these different computational schemes are the assumptions and computations that account for the regions of contact and the zones of stick and slip. Throughout the presentation of the results, the effectiveness of having stress as a nodal variable is demonstrated and highlighted.

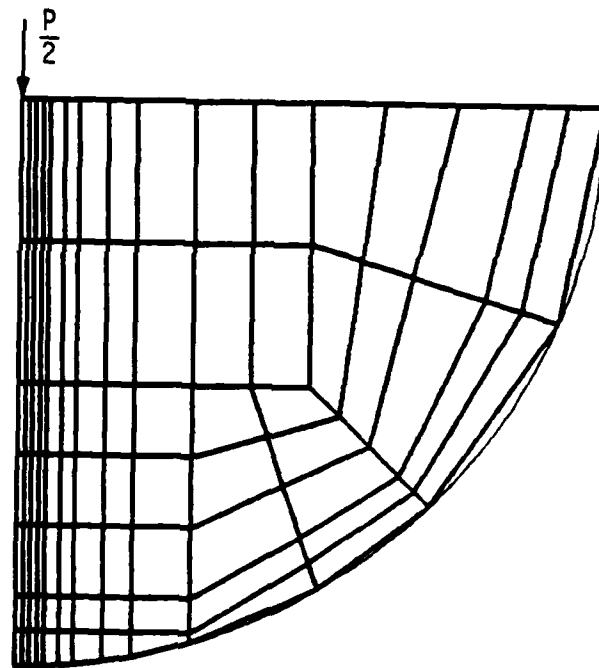
### 5.2 Rigid Pin Algorithm Examples

The contact algorithm proposed by Rahman in [48] was implemented using the three basic iterations of load, contact, and friction using a geometrically nonlinear formulation along with mixed finite elements. Here the results of several example problems involving contact between an elastic body and a rigid pin are presented not only to demonstrate the accuracy of the algorithm but also to highlight the effectiveness of having stress as a nodal variable. The results of the example problems are compared with available analytical and numerical solutions.



$E = 21000 \text{ psi}$   
 $\nu = 0.3$   
radius = 1 in.  
thickness = 1 in.

a) Geometry and material properties of cylinder



b) Finite element mesh used for quarter cylinder

Figure 5. 1 Modeling used for infinite cylinder resting on rigid plane under uniform line load

### 5.2.1 Infinitely Long Cylinder Under Uniform Load

As a first example we consider an infinitely long cylinder of radius  $r = 1$  inch resting on a rigid plane and under a uniform line load. This problem was modeled using the assumptions of plane strain and a thickness of 1 inch. One quarter of the circular domain was used to model the problem and was approximated by 84 linear elements. The mesh is shown in Figure 5.1. The load was assumed to act at the center of the cylinder and was applied in 12 increments with the initial increments smaller than the later increments. The problem was modeled by assuming that the cylinder was in contact with a rigid pin of very large radius ( $R = 1000$  in.) to model the rigid plane. A tolerance of 0.001 (i.e. 0.1 percent) was used for the equilibrium iterations. The modulus of elasticity used was 21,000 psi and the Poisson's ratio used was 0.3.

The results of the analysis are shown in Figures 5.2 and 5.3. The numerical results are compared with the Hertz analytical solution [63]. Figure 5.2 shows the contact pressure distribution plotted against the distance from the original point of contact and corresponds to a total applied load of 56 lbs. Figure 5.3 shows the load plotted against the total contact area, the data points of which can only be determined when each successive node comes in contact with the pin. The results from the contact algorithm appear to be quite good.

### 5.2.2 Orthotropic, Pin-Loaded Plate

The second example considers a thin, orthotropic, pin-loaded plate with a hole of radius  $r$  under a uniform in-plane load, similar to the situation shown in Figure 3.1. The modeled plate is shown in Figure 5.4 along with the geometrical and material properties of the plate. Due to

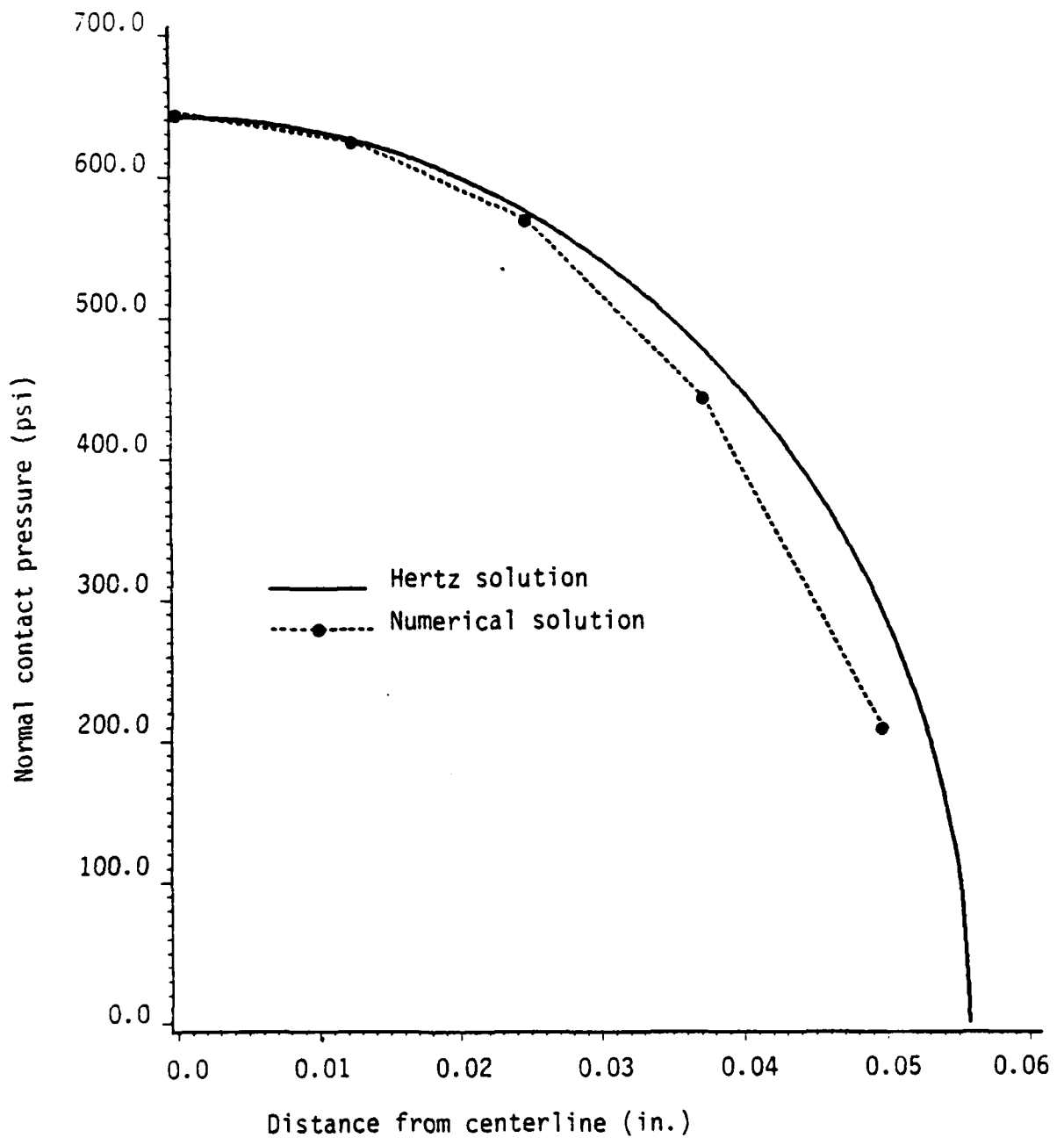


Figure 5.2 Contact pressure distribution for infinite cylinder using rigid pin algorithm

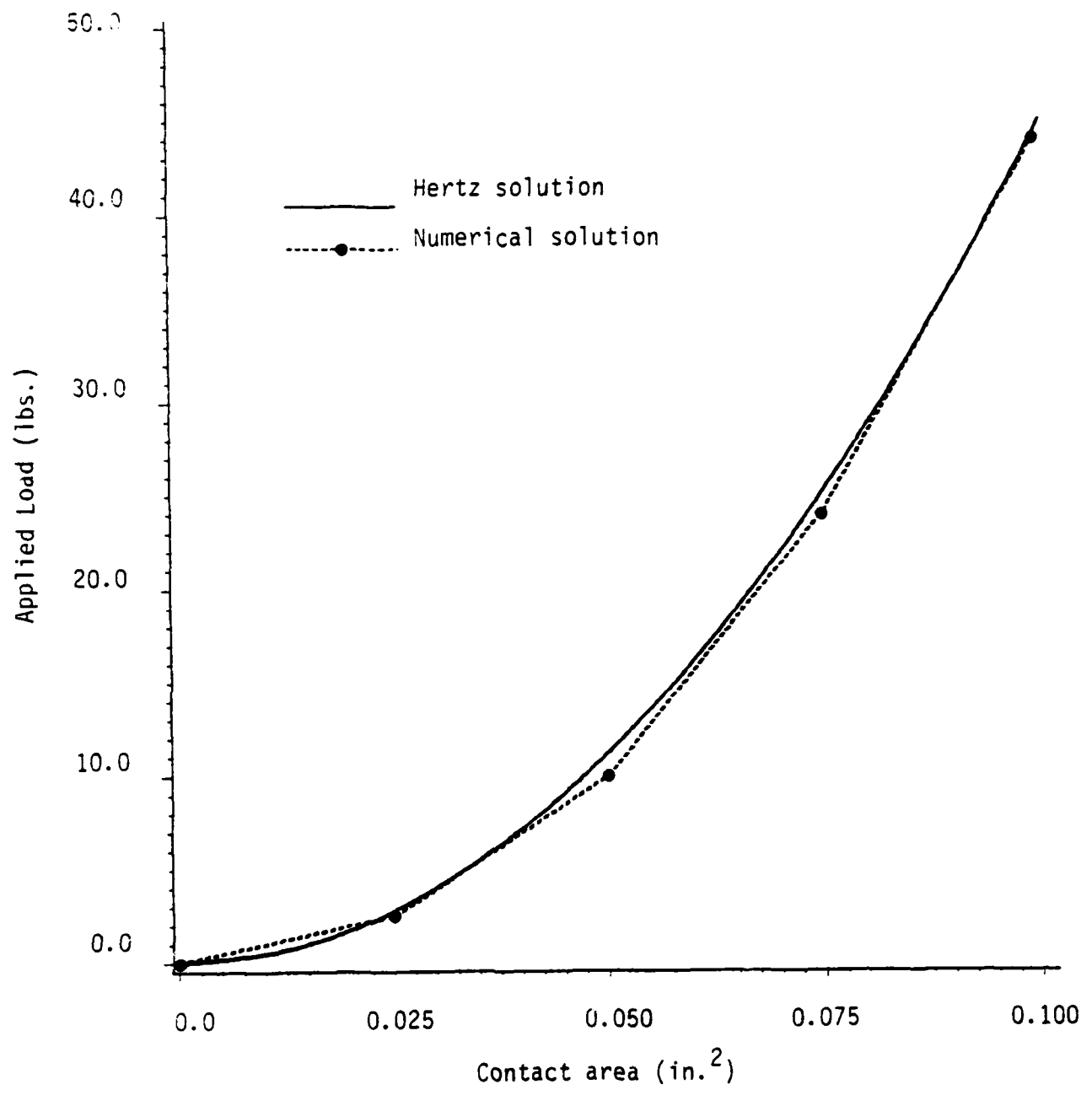
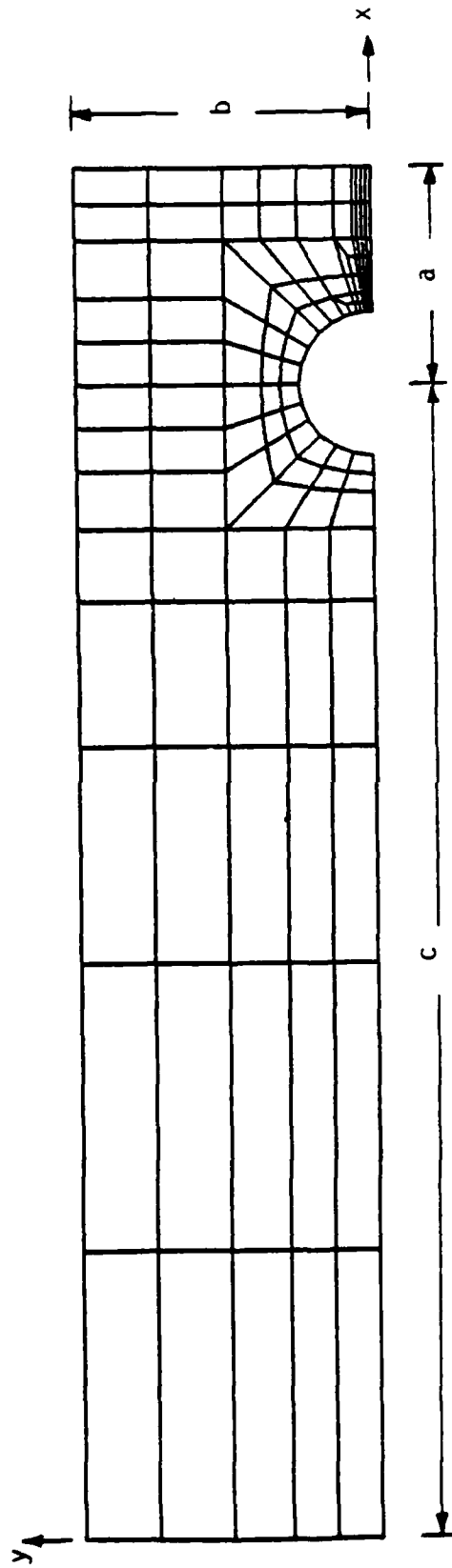


Figure 5.3 Contact area for infinite cylinder using rigid pin algorithm



$R =$  radius of plate hole = 0.25 in.

$r =$  radius of pin = 0.231 in.

$c =$  4.0 in.

$a =$  0.75 in.

$b =$  1.0 in.

$t =$  thickness of plate = 0.25 in.

$$E_x = 2.4 \times 10^6 \text{ lb./in.}^2$$

$$E_y = 0.12 \times 10^6 \text{ lb./in.}^2$$

$$G_{xy} = 0.144 \times 10^6 \text{ lb./in.}^2$$

$$\nu_{xy} = 0.5$$

Figure 5.4 Material properties and finite element mesh used for pin-loaded plate example



symmetry, one half of the plate was modeled using 124 linear elements with 156 nodes for a total of 780 degrees of freedom. The material properties given in the figure are averaged properties from a number of species of wood. The pin was assumed to be rigid and of radius  $R$ . The plate was loaded to a final load of 400 pounds per inch of plate thickness, and was applied in 18 unequal increments. A constant coefficient of friction of 0.7 was assumed at all points of contact between the plate and the pin for all load levels and is a typical value for wood on steel. No equilibrium iterations were performed for this problem.

Figure 5.5 shows the radial stress distribution as a function of the angular position around the pin for the nodes that have come in contact at the final load step. These results are compared with the results obtained by Wilkenson [64] using a finer mesh (385 nodes) and quadratic displacement elements. The comparison is very good.

### 5.3 Elastic Pin Algorithm Examples

The method of analyzing contact problems developed in Section 3.3 is much more general than the algorithm described in Section 3.2 which uses the assumption of a rigid pin. Although this assumption greatly simplifies the analysis, it also restricts the number of problems to which this technique may be applied, since one of the bodies must be rigid and have a circular shape. This second requirement is certainly valid for the present study, as the primary problem of interest is that of a pin-loaded plate, but it should be pointed out that the scheme developed in Section 3.3 is much more versatile and may be applied to a much larger variety of contact problems.

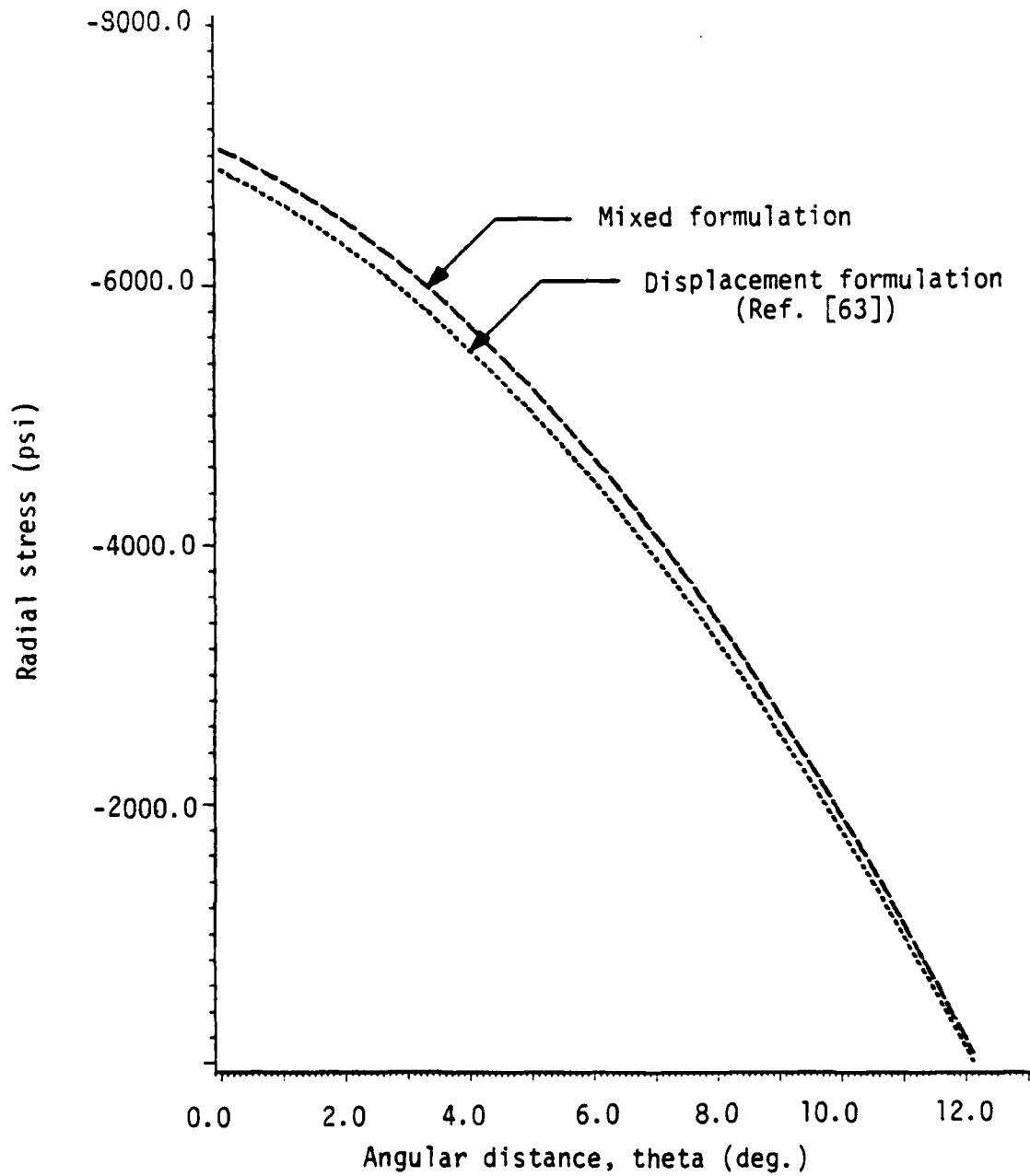


Figure 5.5 Radial stress distribution around hole of orthotropic plate using rigid pin algorithm

### 5.3.1 Infinitely Long Cylinder Under Uniform Load

As a first example of the so-called elastic pin algorithm, we consider the Hertz contact problem analyzed by the rigid pin algorithm in the previous section. This problem was modeled using the three different mesh configurations shown in Figure 5.6. The geometry and material properties of the cylinder are identical to those shown in Figure 5.1. The rigid plane in this case is modeled as a square block of very high stiffness with its displacements specified to be zero and would be defined as the target body according to the terminology introduced in Section 3.3.

Instead of applying the load to the quarter cylinder by means of a point load along the vertical centerline, as done in the previous section, we instead require the upper horizontal mid-plane of the cylinder to deform a uniform amount. Hence, we specify the vertical displacements of each of the nodes along this horizontal mid-plane to be a certain distance for each successive load step. The total load may then be computed by summing each of the nodal forces corresponding to the specified vertical displacements. For this example, the load was applied in 14 non-uniform displacement increments until a final displacement of 0.014 inches was reached. Since this problem involves frictionless contact, sliding matrices are always imposed for a node in contact, even for the first iteration.

Figures 5.7-5.9 show the contact pressure distributions computed by the elastic pin algorithm, shown by the dotted lines, between the cylinder and the rigid plane for the cases corresponding to the total applied displacements of 0.006 and 0.014. We note that the smaller displacement level corresponds to an applied loading of approximately  $P$

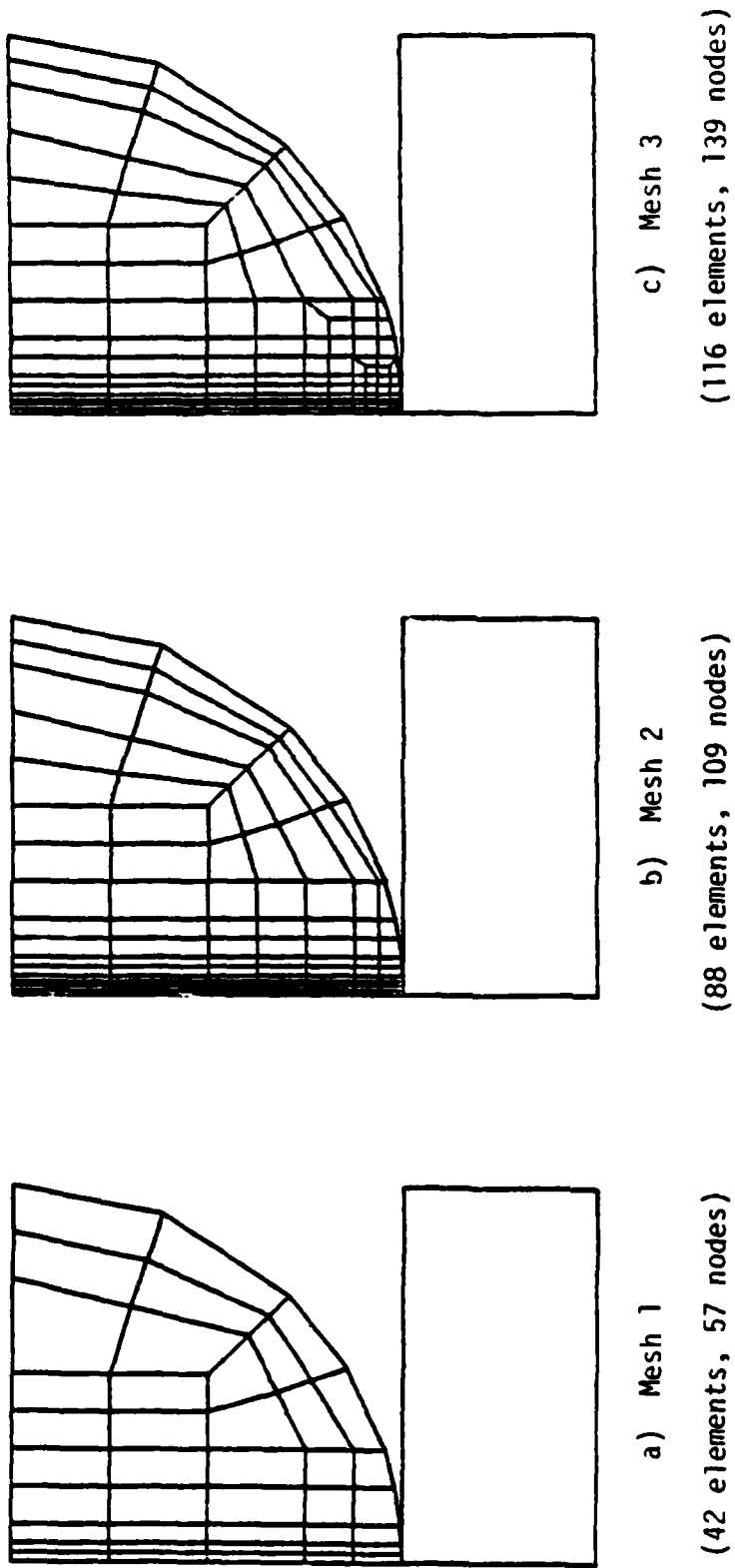


Figure 5.6 Mesh configurations used for analysis of Hertz problem using elastic pin algorithm

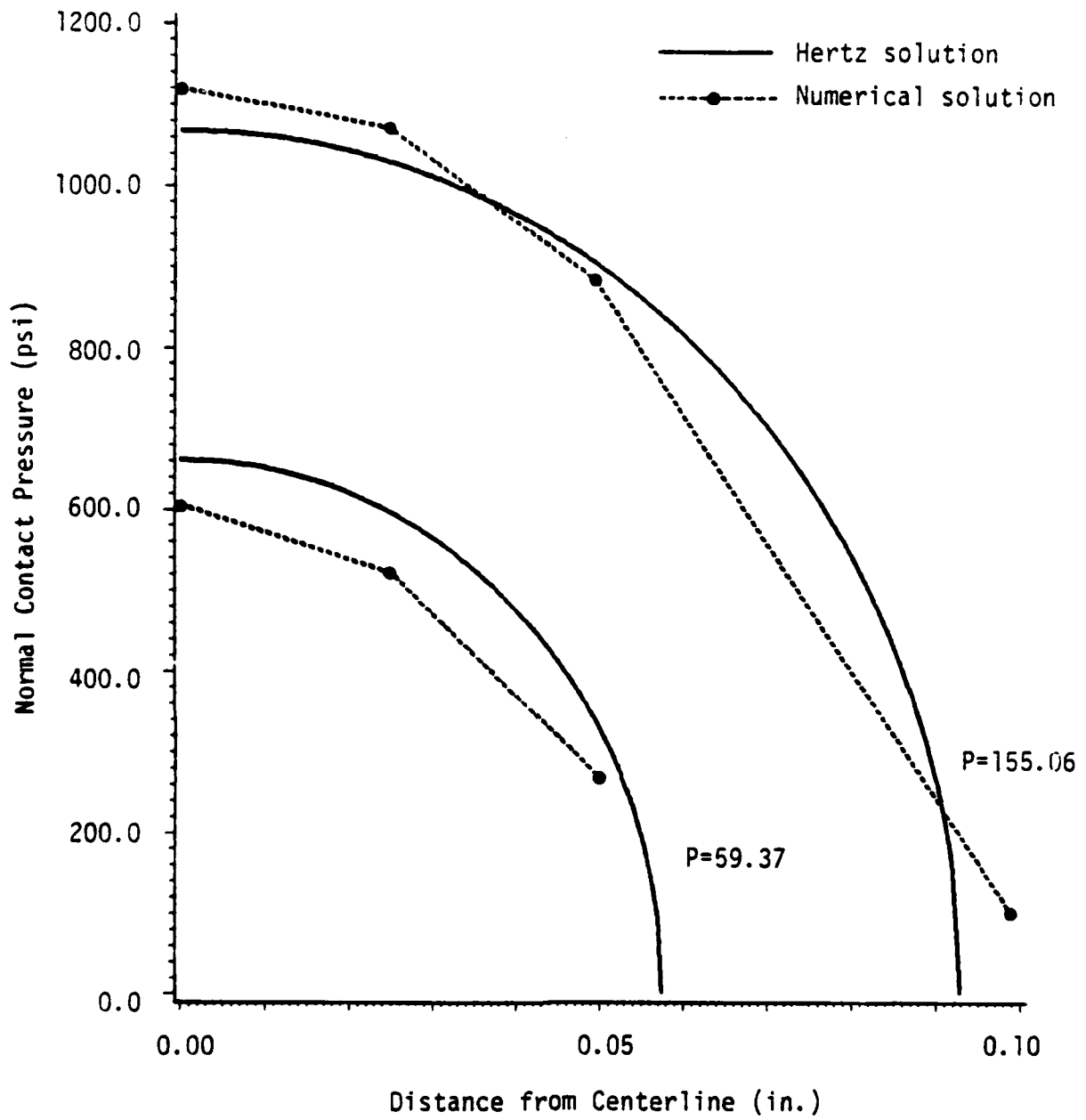


Figure 5.7 Contact pressure distribution for infinite cylinder using elastic pin algorithm and mesh 1

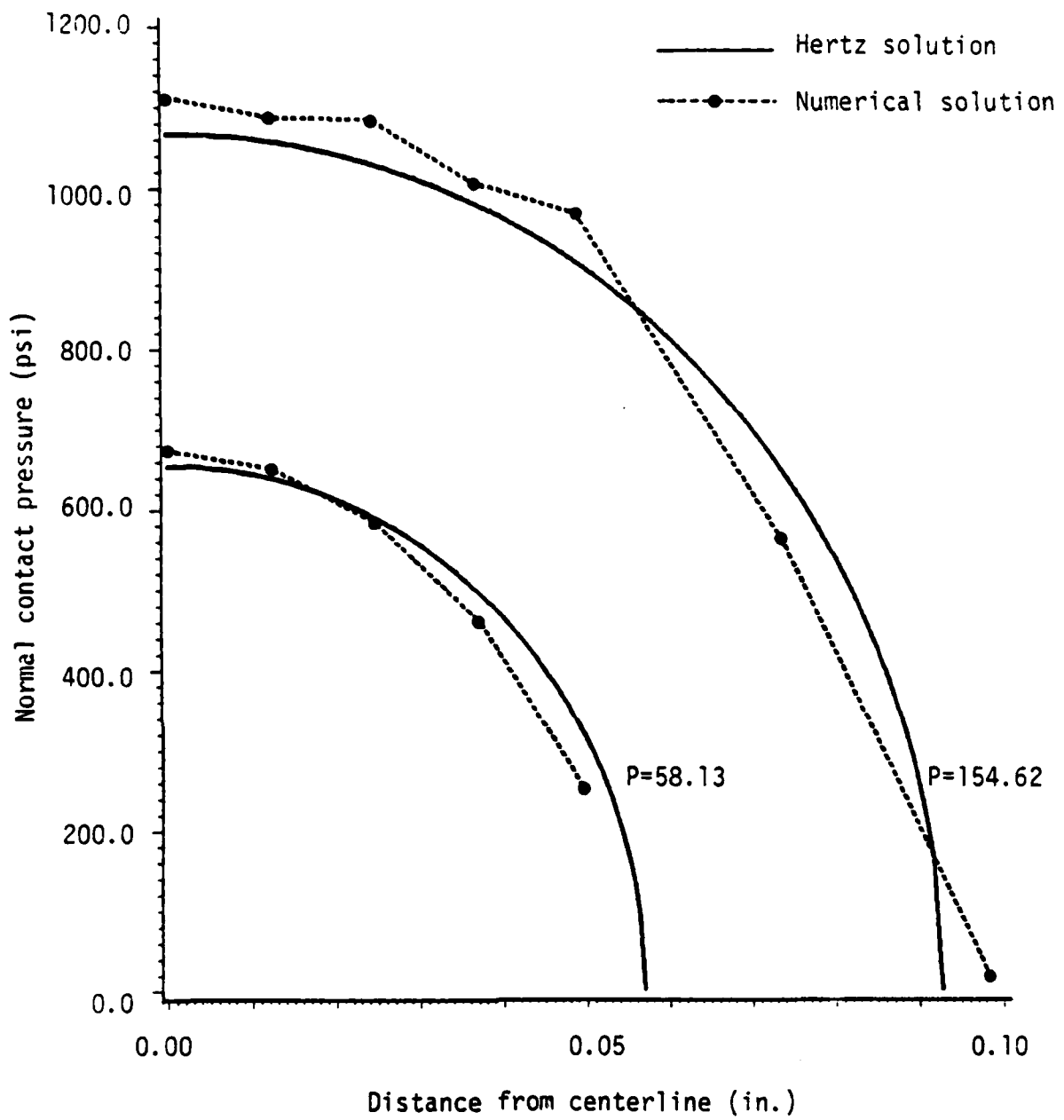


Figure 5.8 Contact pressure distribution for infinite cylinder using elastic pin algorithm and mesh 2

= 56 lbs. which is near the final load level reached for the same problem analyzed by the rigid pin contact algorithm and hence may be compared with the results given in Figure 5.2. The computed stresses are compared with the Hertz analytical solution which is again represented by the solid line in the figure. The agreement is quite good for both load levels and improves as the mesh is refined.

The stress distributions have been plotted on different graphs due to the change in the Hertz solution resulting from the differences in the total applied load. As the mesh is refined, the force required to displace the horizontal mid-plane of the cylinder decreases since the cylinder is generally becoming more flexible. This change in load is relatively small, but makes a large enough difference in the Hertz solutions to warrant separate figures.

It is also of interest to compare the changes in the contact pressure distributions for different frictional conditions. The plot of the contact pressure along the rigid plane measured at the final load step for mesh 3 is shown in Figure 5.10 as a function of the distance away from the vertical centerline of the cylinder for various values of the coefficient of friction,  $\mu$ . The plot of the Hertz analytical solution is shown by the solid line in the figure. We note that as the coefficient of friction increases, the total load required to displace the horizontal centerline of the cylinder a uniform amount also increases. Hence in Figure 5.10, even though each of the total applied forces corresponds to the same uniform displacement of 0.014 inches, the Hertz solution is given for the load that is computed from the finite element solution for the case of an infinite coefficient of friction.

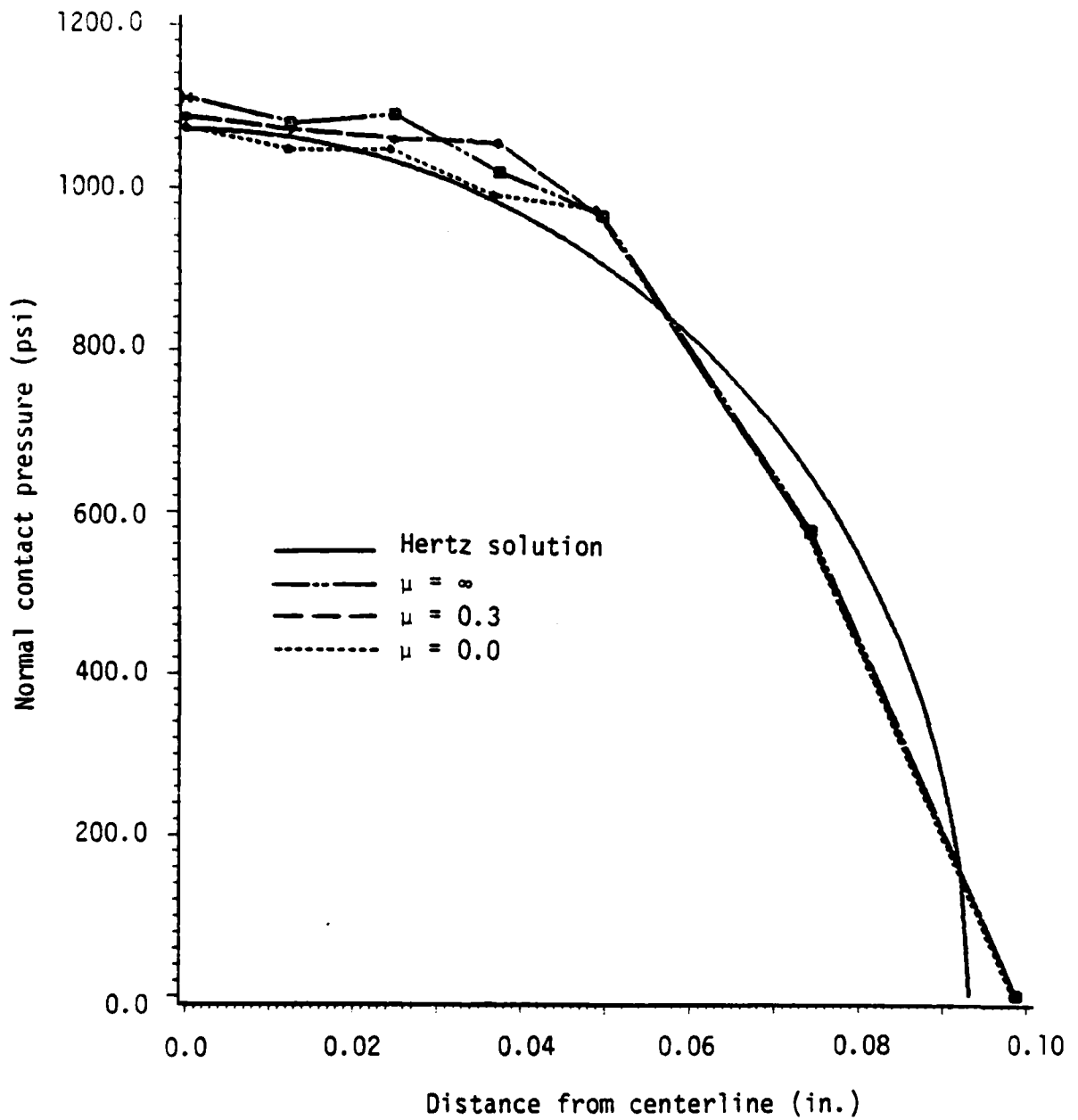


Figure 5.10 Contact pressure distribution for infinite cylinder at maximum load with different frictional conditions ( $\mu$  = coefficient of friction)



The contact pressure distributions shown in Figure 5.10 agree fairly well with the analytical solution. As the coefficient of friction is increased, the contact pressure also increases, especially for the initial nodes of contact. The pressures computed from the computational algorithm for all frictional conditions are generally higher than the pressures computed from the analytical solution due to the stiffening effect of the cylinder as it deforms. Although not shown in this figure, the contact area decreases as the coefficient of friction increases. The contact area may only be determined as each successive contact node on the boundary of the cylinder comes in contact with the rigid plane. For example, for the load level corresponding to the horizontal centerline displacement of 0.011 inches, the seventh contactor node is in contact with the rigid plane for the case of frictionless contact, but this node has not come in contact for the cases where  $\mu = 0.3$  and  $\mu = \infty$ .

A second means of computing the total applied load required to displace the horizontal centerline may be implemented by integrating the contact stresses along the length of the contact area of the rigid block. This not only provides a check on the total applied force, but it also gives some indication as to the accuracy of the nodal stresses computed from the mixed finite element model. The resulting forces calculated by integrating the contact pressures using a consistent formulation for each of the displacement increments are shown for mesh 3 in Figure 5.11, denoted by the dashed line, and are plotted against the total specified displacement of the cylinder mid-plane. These forces are compared with the forces computed from summing the equivalent nodal forces at the points of specified displacement, shown by the dotted line

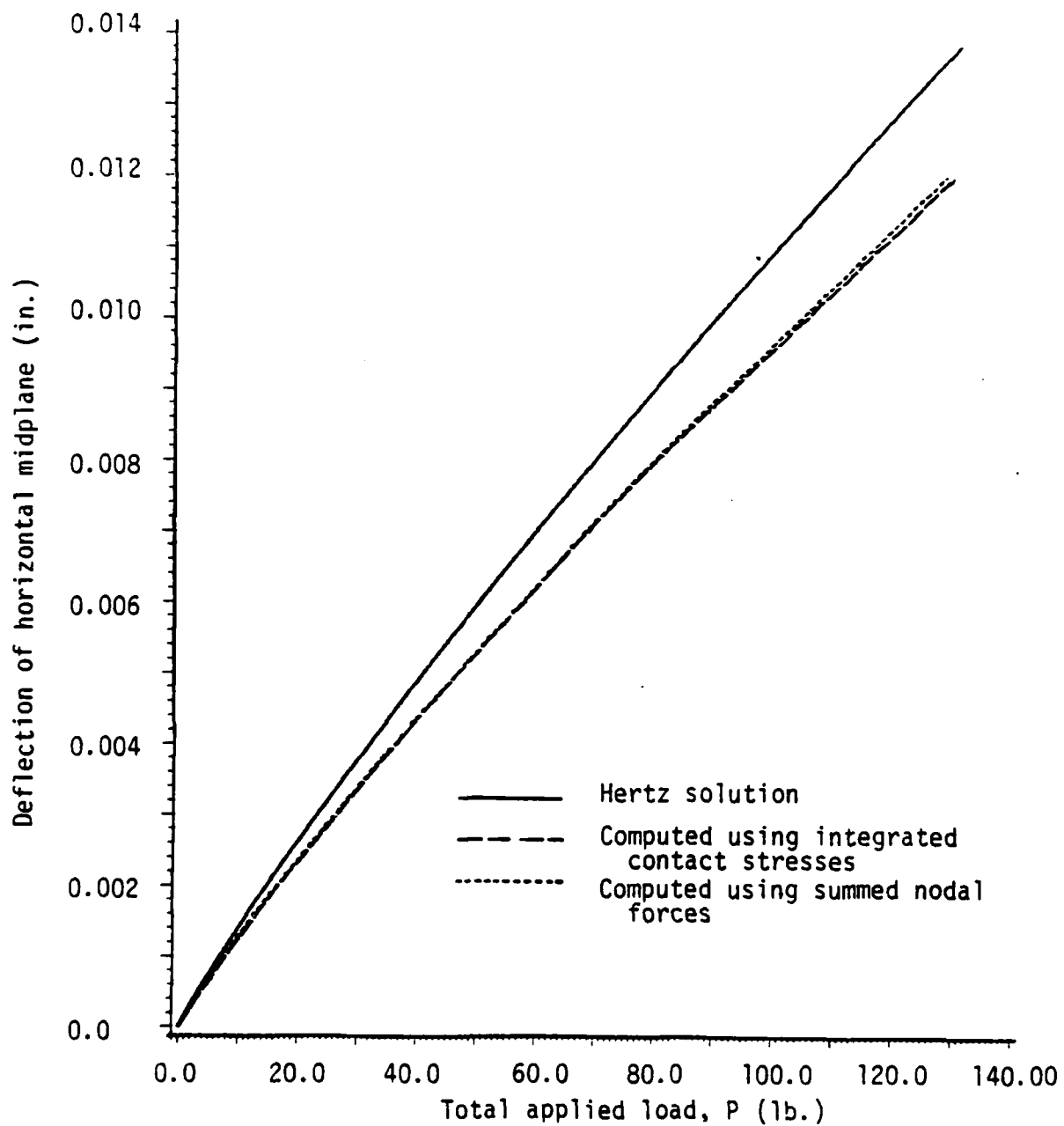


Figure 5.11 Total applied force comparison for infinite cylinder using elastic pin algorithm

in the figure. Also shown are the forces computed from the exact solution which are denoted by the solid line. Clearly, the applied loads calculated from the two methods within the finite element solution are in excellent agreement with the forces computed using the pressure integration being somewhat higher than those computed from the nodal forces. Both of these loads are larger than the corresponding exact loads computed for a given displacement, and again this is due to the stiffening effect of the cylinder.

### 5.3.2 Orthotropic, Pin-Loaded Plate

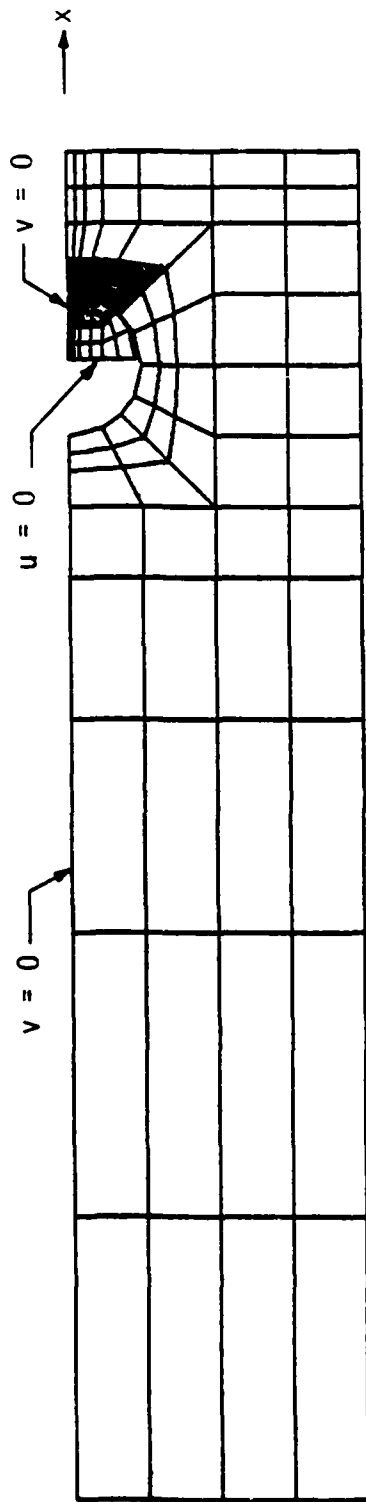
We next consider the orthotropic, pin-loaded plate previously analyzed by the rigid pin algorithm in Section 5.2.2. The allowance for an elastic pin requires that the domain of the pin be analyzed as well as the domain of the plate. Since the elastic pin algorithm was developed using linear elements, this discretization introduces another source of error into the problem since the approximation of the curved boundaries of both the plate and the pin must be approximated by a series of straight line segments. As with any finite element discretization, however, this approximation error decreases as the mesh is refined.

The location of the boundary nodes at the pin/plate interface, though not difficult to model, does require special attention to ensure that the limitation of straight line segment boundaries does not result in the nodes of the contactor body (i.e., the pin) being initially within the domain of the target body (i.e., the plate). The mesh generation was performed such that the nodes on the boundaries of both the plate and the pin were located on the correct geometric locations on

the appropriate circular boundaries, while all nodes of the pin were located outside the domain of the plate.

A major disadvantage of this algorithm in the analysis of the pin-loaded plate problem is that the pin must be discretized as well as the plate. While this does not increase the total number of degrees of freedom to an unreasonable extent, it does hinder the effectiveness of the bandwidth reduction scheme mentioned in Section 4. As the nodes of the pin come in contact with the target segments of the plate, the global influence of the degrees of freedom corresponding to the given contactor node extends to the corresponding target node degrees of freedom of the plate. Care must therefore be taken in the numbering of the nodes of the pin and the plate to ensure that the resulting bandwidth does not exceed the allowable maximum as new contactor nodes of the pin come in contact with the plate.

The domain of this problem was modeled using three different mesh configurations where the symmetry of the plate was used to advantage. The initial coarse mesh is shown in Figure 5.12 along with the appropriate specified zero displacements. Most of the subsequent mesh refinement was restricted to the region of probable contact to increase the number of contact points between the pin and the plate. This region is shown by the darkened area in Figure 5.12. The three element meshes corresponding to this sub-region are shown in Figure 5.13. In general, the region of contact was estimated to be within  $0^\circ$  and  $45^\circ$ , where  $0^\circ$  represents the initial point of contact between the pin and the plate. The coarse mesh (mesh 1 in Figure 5.13) consisted of 99 elements and 132 nodes and contained 6 specified contactor nodes. Hence the total number of degrees of freedom corresponding to his mesh is 672 ( $132 \times 5 + 6 \times$



Darkened area represents region of refinement

Material Properties

Plate:  $E_1 = 2.4 \times 10^6 \text{ lb./in.}^2$

$E_2 = 0.12 \times 10^6 \text{ lb./in.}^2$

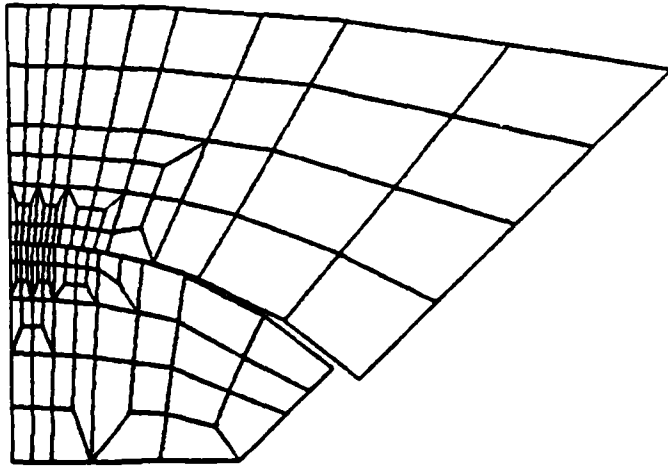
$G_{12} = 0.144 \times 10^6 \text{ lb./in.}^2$

$\nu_{12} = 0.5$

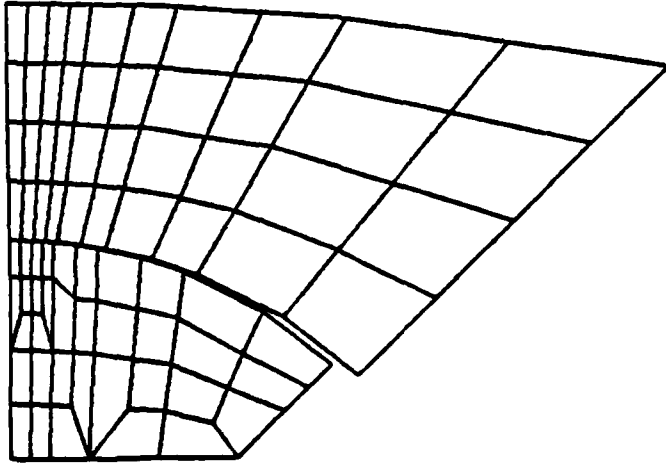
Pin:  $E = 29.0 \times 10^6 \text{ lb./in.}^2$

$\nu = 0.3$

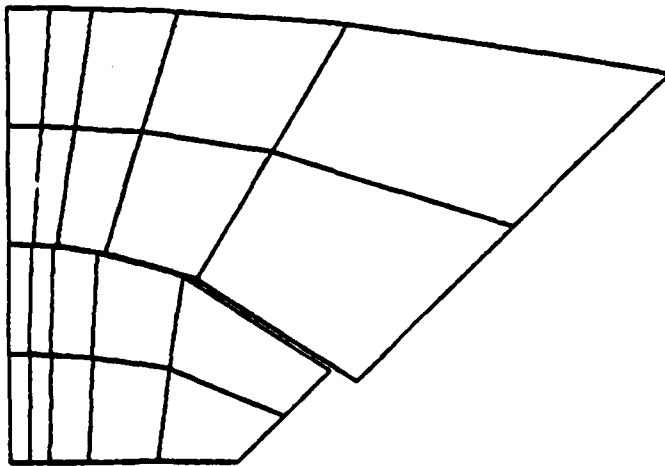
Figure 5.12 Coarse mesh used for pin-loaded plate example using elastic pin algorithm



(c) Mesh three



(b) Mesh two



(a) Mesh one

Figure 5.13 Discretized contact subregions for pin-loaded orthotropic plate example

2). The refined domain approximations resulted in 1085 and 1433 total degrees of freedom for mesh 2 and mesh 3, respectively.

The plate was loaded to a final load of 400 pounds per inch of plate thickness, and was applied in 12 unequal increments using an error tolerance per load step of 0.01. The material properties used for the plate are identical to those of the orthotropic plate shown in Figure 5.4, but the material properties for the pin were taken to be those of steel, and were assumed to be given by  $E = 29,000$  ksi and  $\nu = 0.3$ . The physical dimensions of the plate and the pin are identical to those given in Figure 5.4.

The radial stress distributions around the hole of the plate are shown as a function of angular position in Figure 5.14 for  $P = 0.32 P_{\max}$  and in Figure 5.15 for  $P = P_{\max}$ . In Figure 5.15 the stresses from each of the three different meshes are represented by dashed lines and are compared with the results obtained by Wilkenson [64] which are shown by the solid line and were obtained using the assumption of a perfectly rigid, circular pin. The results are fairly reasonable even for the coarse mesh, although the stresses are significantly underestimated near the initial points of contact. As the mesh is refined, however, both the shape of the stress distribution and the maximum stress values approach the solution obtained by Wilkenson, yielding fairly good agreement for the final refined mesh.

An important point to note is that the maximum stress given by the elastic pin algorithm is not given at the point of initial contact. In fact, the nodal stresses do not follow a regular pattern of decreasing as the angular position away from the initial contact point increases, as reported by Wilkenson. It is unknown if the pattern shown is a

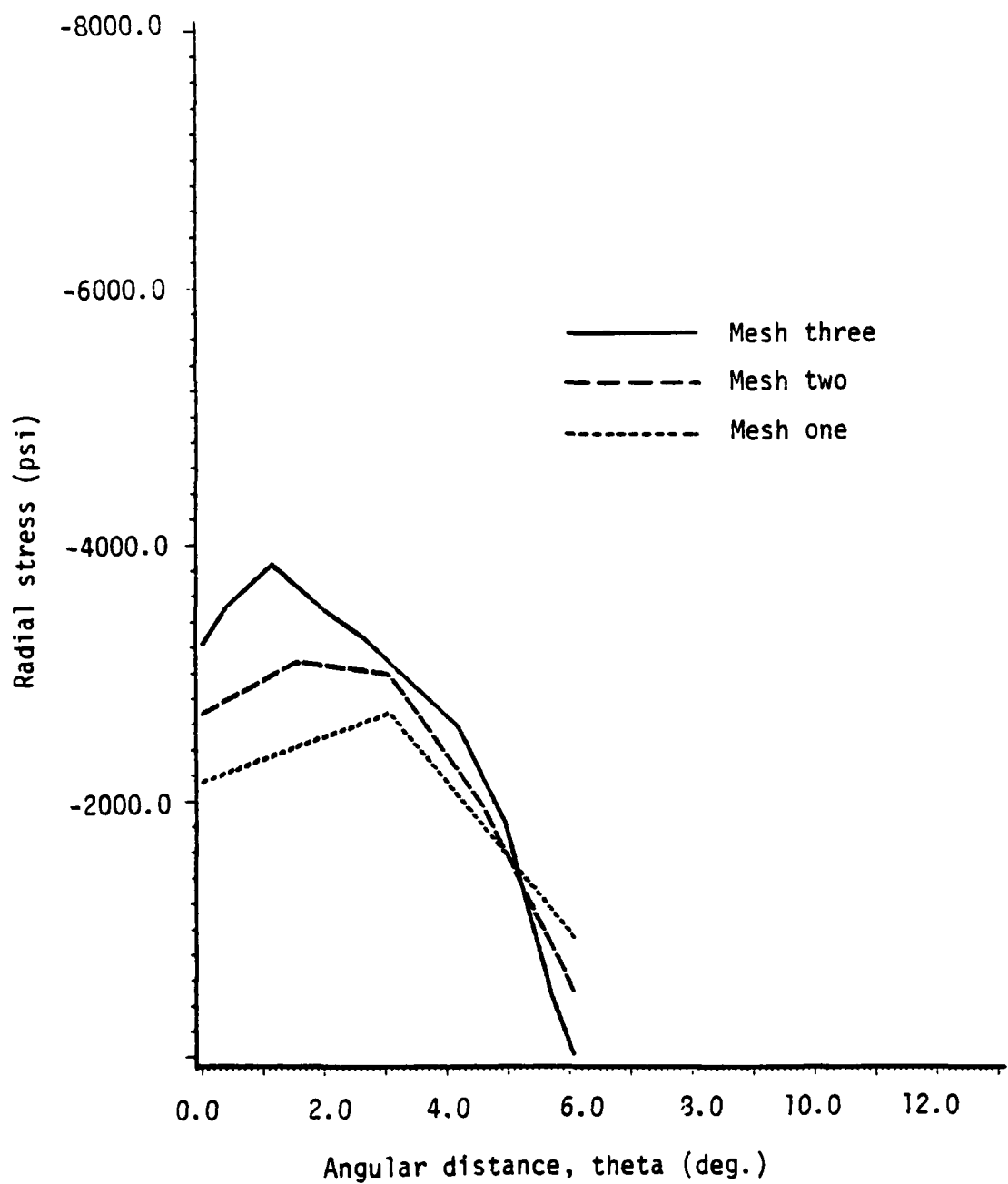


Figure 5.14 Radial contact stress distribution using elastic pin algorithm with  $P=0.32P_{max}$



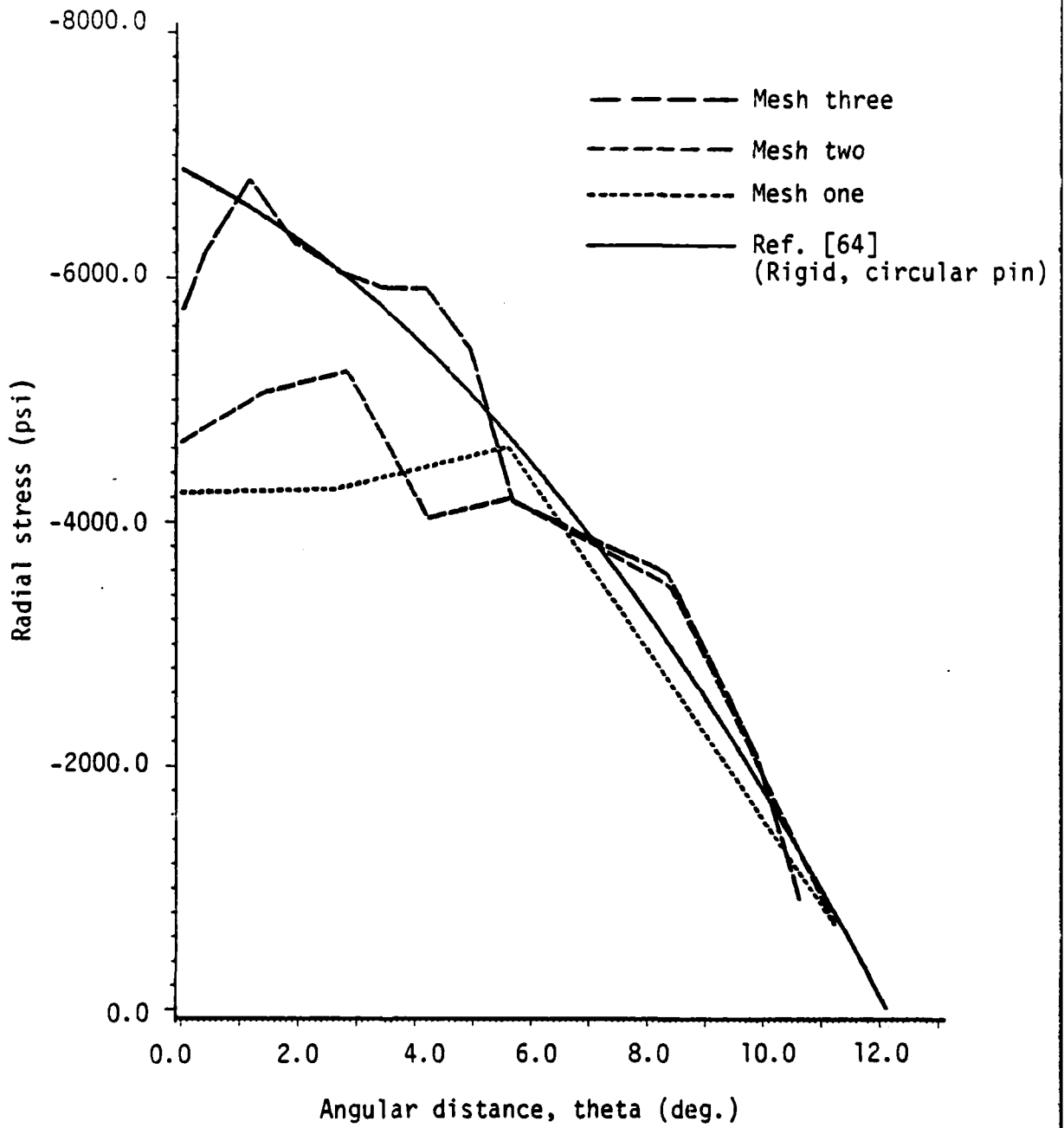


Figure 5.15 Radial contact stress distribution using elastic pin algorithm with  $P=P_{max}$

result of the modeling of the problem, the contact algorithm used, or as a consequence of using mixed elements. It should be pointed out, however, that the results given in [64] were plotted using a smoothing routine, and in the actual analysis of this problem, reported in [47], this phenomena of increasing stress with increasing angle was recorded at several points around the boundary of the plate. Furthermore, in one of the few other contact analyses that used mixed elements, this effect is also shown rather dramatically in the analysis of the Hertz contact problem [45].

In this example problem, the results of the elastic pin algorithm are compared with the results obtained by means of a different technique using the assumption of a perfectly rigid pin. To simulate this rigid pin, the material properties of steel were used. To investigate the effect of higher pin stiffness on the resulting stress distributions, the analyses in this section were repeated using a pin modulus of elasticity one order of magnitude larger than that of steel. Poissons ratio was kept as 0.3. For both mesh configurations, the displacements near the contact region decreased approximately one order of magnitude from the displacements using the steel pin. This discrepancy decreased rapidly away from the contact region, with the displacements at the loaded end of the plate differing by only one percent. More importantly, the increase in pin stiffness had a very small effect on the radial stress distributions as all computed stresses around the plate were within two percent of one another. Hence within the context of this example, the rigid pin was adequately modeled by having a modulus of elasticity approximately one order of magnitude higher than that of the plate.

### 5.3.3 Aluminum, Pin-Loaded Plate

We next consider a second example problem involving a pin-loaded plate. The specimen used in this example is the aluminum plate shown in Figure 4.1. The plate is restrained by an aluminum pin that is assumed to be of the same thickness (0.061 inches) as the plate. The mesh used to model the plate and the pin is shown in Figure 5.16 and contains 236 elements, 286 nodes, and has a total of 16 possible contact nodes, which accounts for 1462 total degrees of freedom. The mesh used to discretize the plate is very similar to the mesh of linear elements used in the implementation of the hybrid technique shown in Figure 4.2. Only the region of initial contact contains slightly fewer elements and nodes.

In contrast to the previous example, the initial clearance between the pin and the plate is very small for this problem. Hence even for a very small initial load increment several nodes will come in contact at the same time. The algorithm used to analyze this problem was written such that the specified displacement increments corresponding to the penetration of a contactor node are imposed one at a time to ensure that the effects of each of these displacement increments do not subsequently alter the penetration distance of subsequent contactor nodes. The loading for this problem was applied in 6 increments with initial small load steps giving way to much larger load steps until a final load of 1037 pounds was applied to the plate. The material properties used for this plate were the same as those given in Section 4.4.1. A coefficient of friction of 0.15 was used in this example.

Figures 5.17 and 5.18 show the radial and shearing stress distributions computed at the end of the third and sixth load steps, respectively. In each of the figures, the results are compared with the

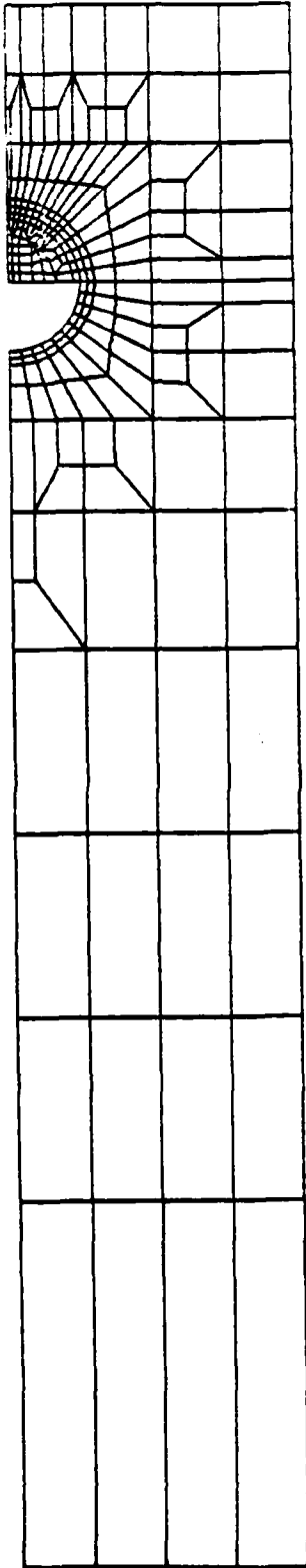


Figure 5.16 Finite element mesh used in analysis of aluminum plate

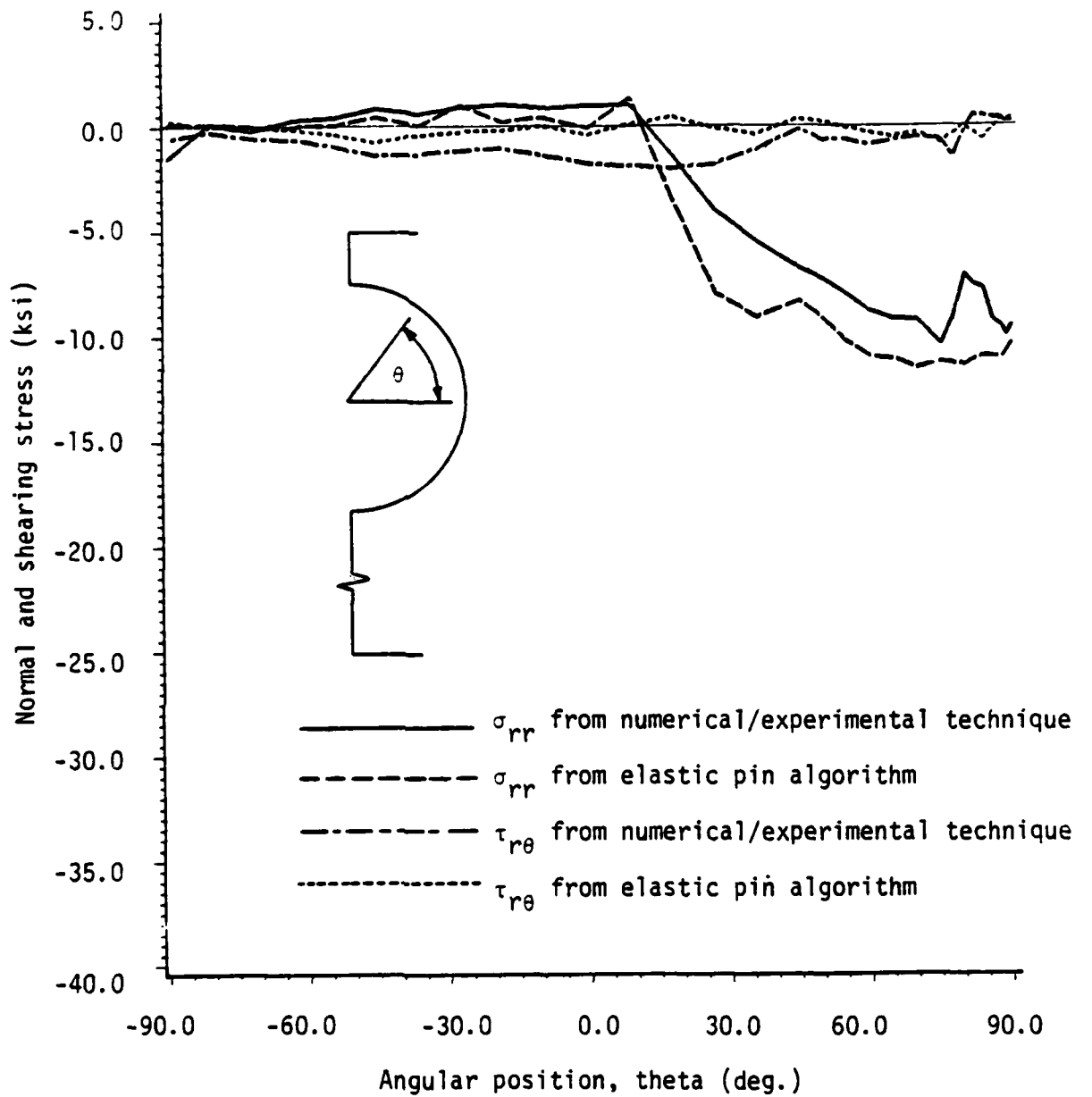


Figure 5.17 Normal and shearing stress distributions for aluminum plate example at 3rd load step

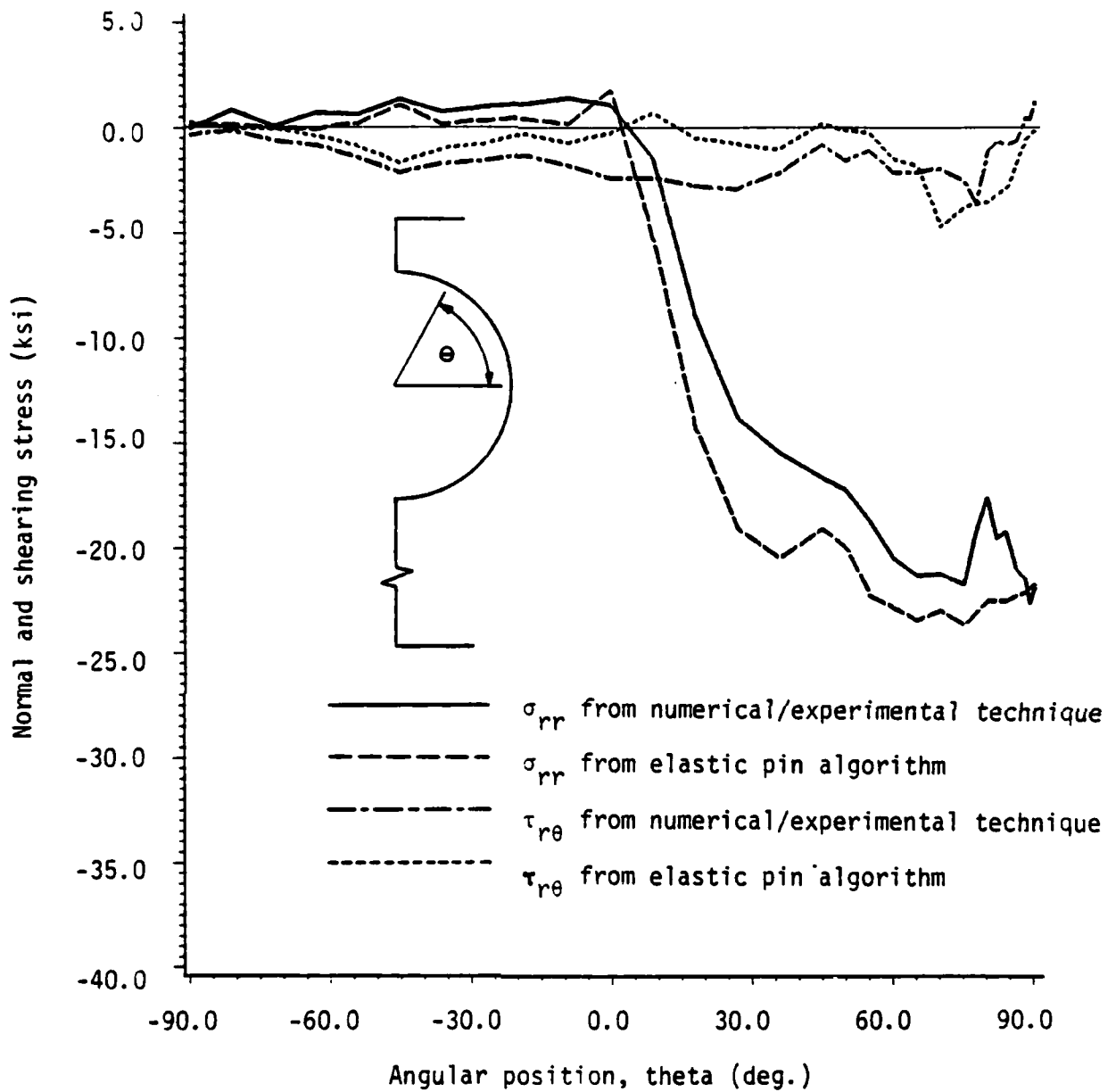


Figure 5.18 Normal and shearing stress distributions for aluminum plate example at 6th load step

corresponding results from the hybrid technique described in Section 4 (see Section 5.5). The radial stress distributions are in quite good agreement with one another where the differences can probably be attributed to the linear domain approximation of the pin, the approximation of the restraining pin using the assumptions of plane stress, and the effects of the relatively large load steps that force several nodes to come in contact for a given increment due to the very small clearance for this problem. The shear stress distribution computed from the elastic pin algorithm increases during the initial 15 degrees of contact and then abruptly drops to near zero. This peak in fact indicates the termination of the zone of sticking contact, and all nodes in contact past this point are in sliding contact. The results from the hybrid technique also show this pattern to a slightly lesser extent, and the shearing stress does not approach zero quite as abruptly.

We also note that in general the displacements in the direction of the load computed by the elastic pin algorithm are larger than those given by the experimental data from the hybrid technique. The differences are largest near the initial points of contact and then dissipate away from this region. This behavior is almost certainly caused by modeling the pin as a two-dimensional body under plane stress conditions when in reality this fixture is much more three-dimensional than is the plate.

#### 5.4 Results of Hybrid Numerical/Experimental Technique

This section contains the results of the implementation of the hybrid technique described in Section 4. All analyses were performed using either the mesh of linear elements shown in Figure 4.2 or the mesh

of quadratic elements shown in Figure 4.3. The loading was typically applied in 9 increments where the values used were given as follows (all values in pounds): 225, 467, 667, 855, 1037, 1240, 1458, 1670, and 1840. This load was assumed to be uniformly distributed along the bottom of the plate. All u displacements (i.e. the displacements in the direction perpendicular to the load) along the centerline of the plate were specified to be zero due to the symmetry of the plate. All nodal displacement increments around the hole interior were specified using the displacement values from the moire analysis, except for the known zero u displacements for the two nodes located on the centerline of the plate.

Several representative radial contact stress distributions are shown in Figure 5.19. In all plots containing the results from the hybrid technique, the angular positions of the data points correspond to the diagram of the truncated plate shown in this figure. The stresses shown here correspond to the second load level and the ninth or final load level. The stresses shown are taken from the mesh of linear elements, represented by the dotted line, and from the mesh of quadratic elements, represented by the solid line. The compressive radial stresses are at a maximum near the initial nodes of contact near  $90^\circ$  and then decrease to near zero for the lower quarter of the hole boundary. This is as expected since the points of initial contact on the plate have normals that are closer to the direction of applied load than the later contact nodes, and would therefore be expected to balance the majority of the load in the radial direction. The stress free condition is well shown in the region from  $-90^\circ$  to  $0^\circ$  with the small variations most likely due to numerical and experimental scatter. In general, good



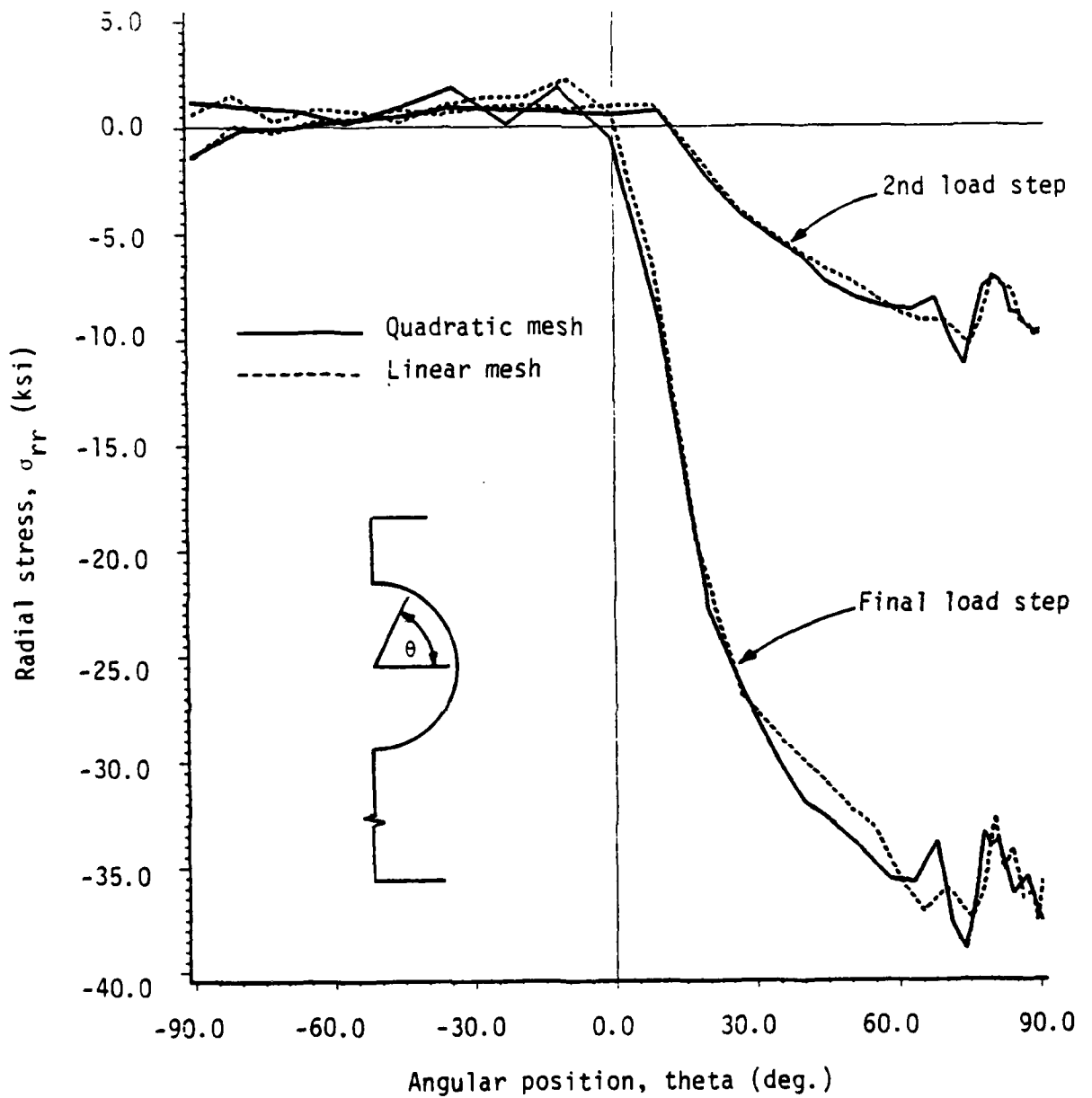


Figure 5.19 Radial contact stress distributions around hole boundary for linear and quadratic element meshes at 2nd and final load steps

agreement exists between the stresses computed using the mesh of linear elements and the mesh of quadratic elements.

It should be stressed that all of the results presented from the hybrid technique in this section are based on the experimental data from a single experiment and should be viewed with this in mind. Since the results are so highly dependent on the experimental data, it is necessary to avoid making sweeping generalizations based on the results presented in this section. Nevertheless, several preliminary observations can be made from these results. First, the region of contact is very large, even for the lower load steps, but never exceeds 90 degrees. This is most likely due to the very small initial clearance between the plate and the pin. Second, there are obvious fluctuations in the compressive stress in the initial 15 degrees of contact for both levels, and in fact this pattern exists for each load step. This is a consequence of an unexplained sequence of sign changes in the  $v$ -displacement increments of the experimental data that appear in this region for each load step. These peculiarities may be due to surface flaws, a localized stick/slip effect, or some other unexplained physical phenomenon. Figure 5.20 shows the radial stress distribution from 0 to 90 degrees for the final load step using the mesh of quadratic elements for a series of increasing radii inside the plate domain. As the distance from the hole boundary is increased, the fluctuations become much smaller and are nearly eliminated altogether for a radius of 0.6 inches. Hence these oscillations are quite localized and are most likely due to a surface effect.

Figure 5.21 shows the shearing stress distributions calculated using the two different mesh configurations measured at the final load

AD-A172 145

A MIXED COMPUTATIONAL ALGORITHM BASED ON THE UPDATED  
LAGRANGIAN DESCRIPTI. (U) VIRGINIA POLYTECHNIC INST AND  
STATE UNIV BLACKSBURG DEPT OF E. P R HEVLIGER ET AL.

2/2

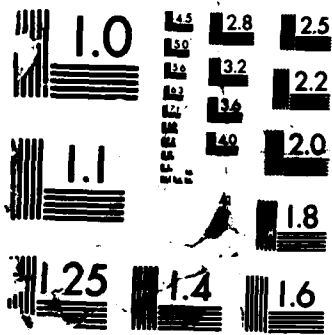
UNCLASSIFIED

AUG 86 VPI-E-86-17 N00014-84-K-0552

F/G 12/1

NL





MICROCOPY RESOLUTION TEST CHART  
NATIONAL BUREAU OF STANDARDS-1963-A

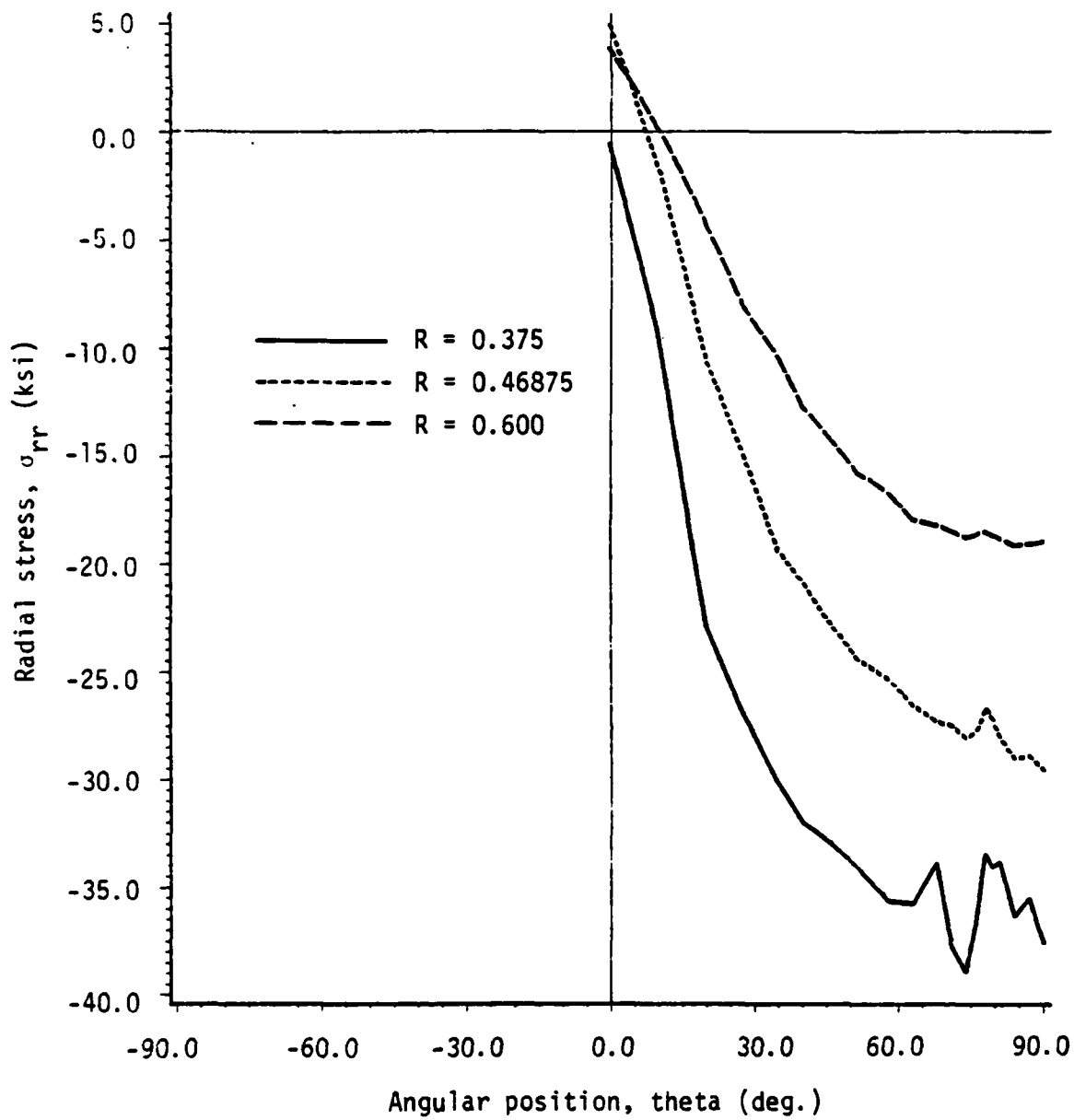


Figure 5.20 Radial contact stress distributions for varying radial distance within the plate domain (quadratic elements)

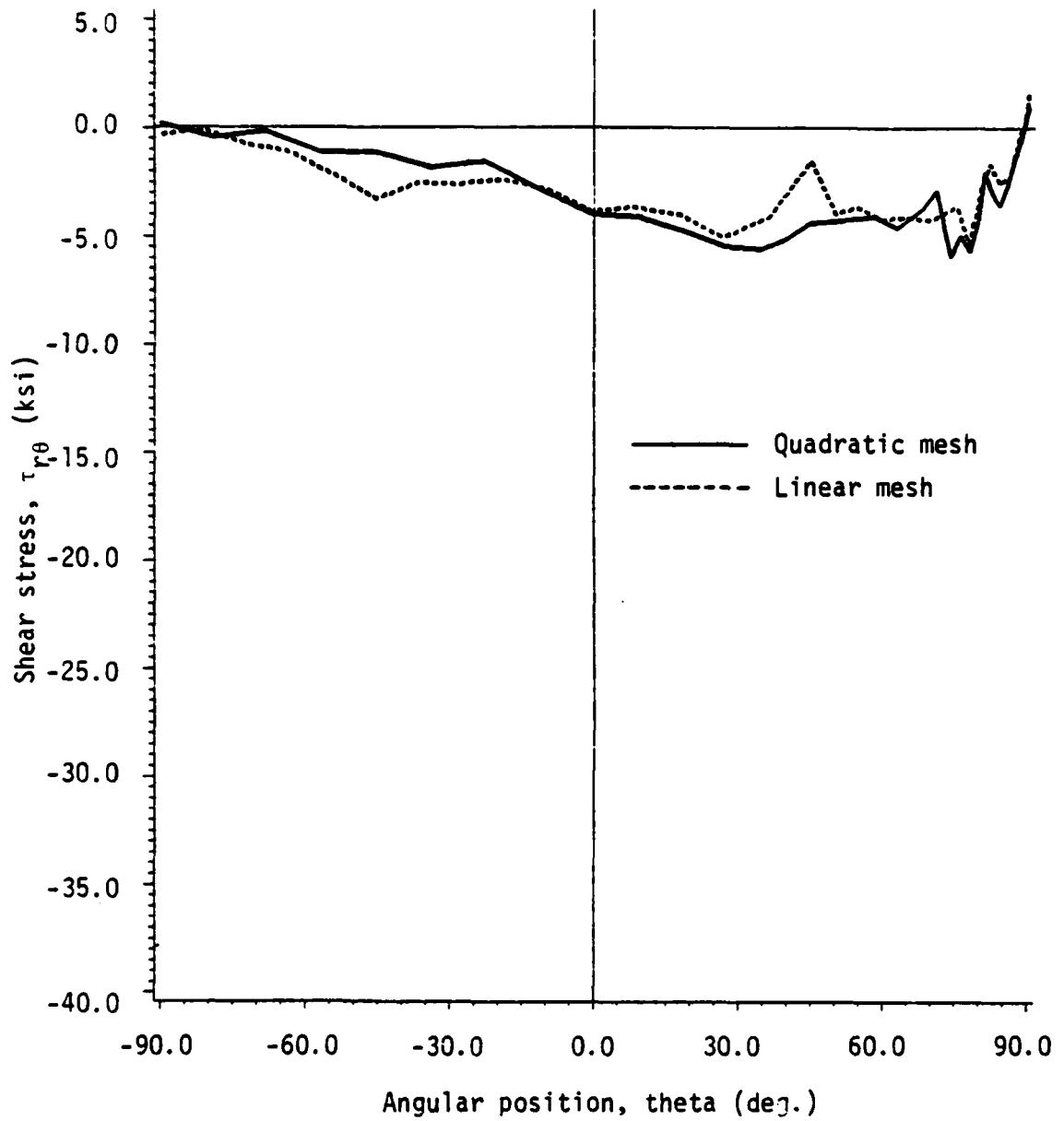


Figure 5.21 Shear contact stress distribution around hole boundary for linear and quadratic element meshes at final load step

step. The trends are generally the same for both meshes except for several obvious kinks that are due to the differences in the data point displacements used and the differences in the two meshes. The values of the shearing stresses are quite small and are in fact nearly an order of magnitude smaller than the corresponding radial stresses for this same load step. Although the stresses are of the proper negative sign, they remain negative and slightly nonzero even in the region of supposed non-contact. It is difficult to ascertain if these patterns are due to the actual behavior of the plate or if either numerical or experimental difficulties are affecting the solution.

The circumferential stress distributions for the final load level are shown in Figure 5.22 for both mesh configurations. These two curves are in very good agreement and, except for the small jumps in the region of initial contact which are again probably due to the discrepancies in the  $v$ -displacement data, this stress distribution is quite smooth. This stress component is of little interest in terms of the contact problem and is mainly shown here for completeness.

In the preceding discussion, the region of contact was always assumed to be determined by the region of compressive stress. Where the radial stress went to approximately zero, the contact region was assumed to have ended. In terms of the hybrid technique, this is the only means that is available for computing the angle or region of contact between the pin and the plate for a given load step.

Fortunately, the experimental data provides a second means of computing the contact area. A cursory glance at the  $u$ -displacements from the moire results shows a positive displacement increment for all of the boundary nodes from  $90^\circ$  down to some angle  $\phi$ . All data points

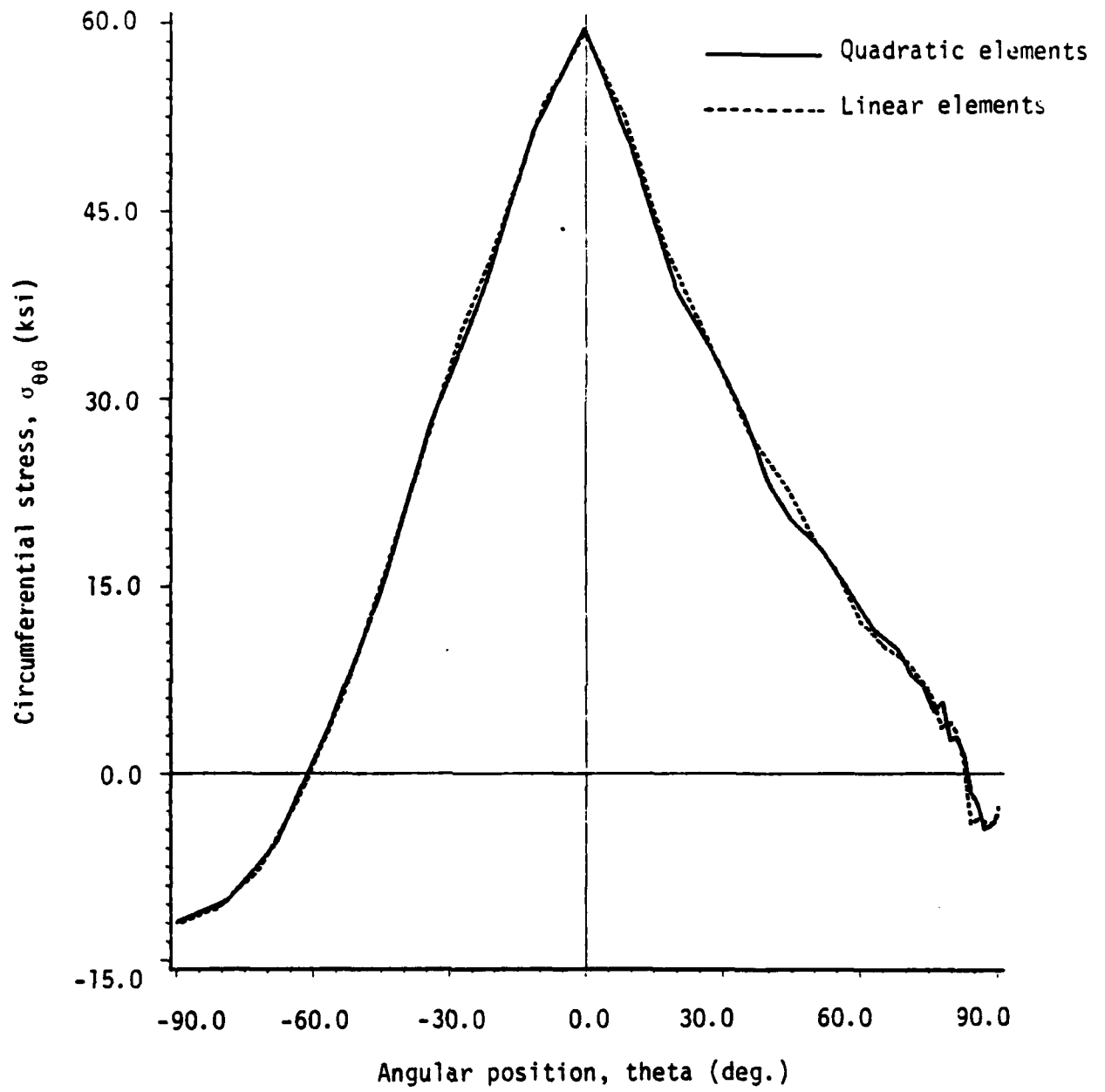


Figure 5.22 Circumferential stress around hole boundary at the final load step



past this angle have a negative u-displacement increment up to the final boundary node located at 180 degrees. The angle  $\phi$  decreases as the loading is increased. Intuitively, one would expect that the only constraint that would cause a positive u-displacement for the nodes on the hole boundary of the plate is the presence of the pin, and that the point of the sign change would correspond to the end of the contact region. This conclusion is reinforced by viewing the resulting radial stress distribution from the hybrid technique and noting that the nodes bounding the change in the sign of the u-displacement increments also bound the change in the sign of the radial stress component from negative to positive (or near zero).

If the above argument holds, one could recall the boundary conditions of the mixed method given in Eqs. (2.50) and (2.51) and note that only the displacements on the contact boundary need be specified since the remaining portion of the hole boundary is stress free. Using the criterion given in the preceding paragraph, only those displacements corresponding to nodes thought to be on the contact boundary were specified using the experimental data. The resulting radial and shearing stress distributions are shown in Figures 5.23 and 5.24, respectively using the mesh of linear elements. The radial stress distributions are in very good agreement with one another, indicating that the change in sign of the u-displacement increments most likely does represent the end of the contact region. There is a small but sharp jump in the stress at the node located at  $0^\circ$  which is most probably caused by specifying the displacements for one node and not specifying the displacements for the adjacent node. The numerical scatter is much smaller from  $-90^\circ$  to  $0^\circ$  and the revised stress is

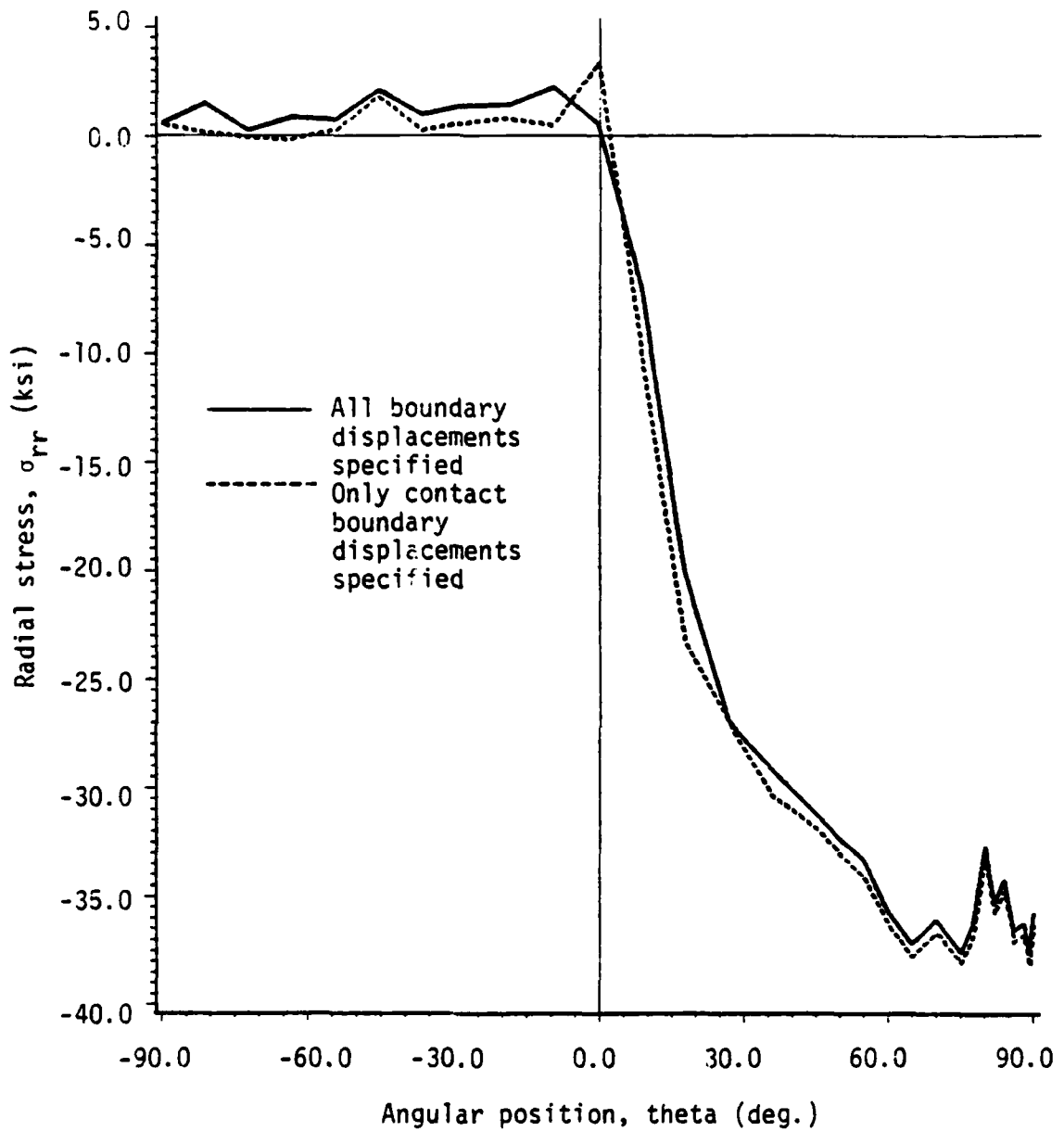


Figure 5.23 Radial contact stress around hole boundary with varying regions of boundary displacements specified using linear elements

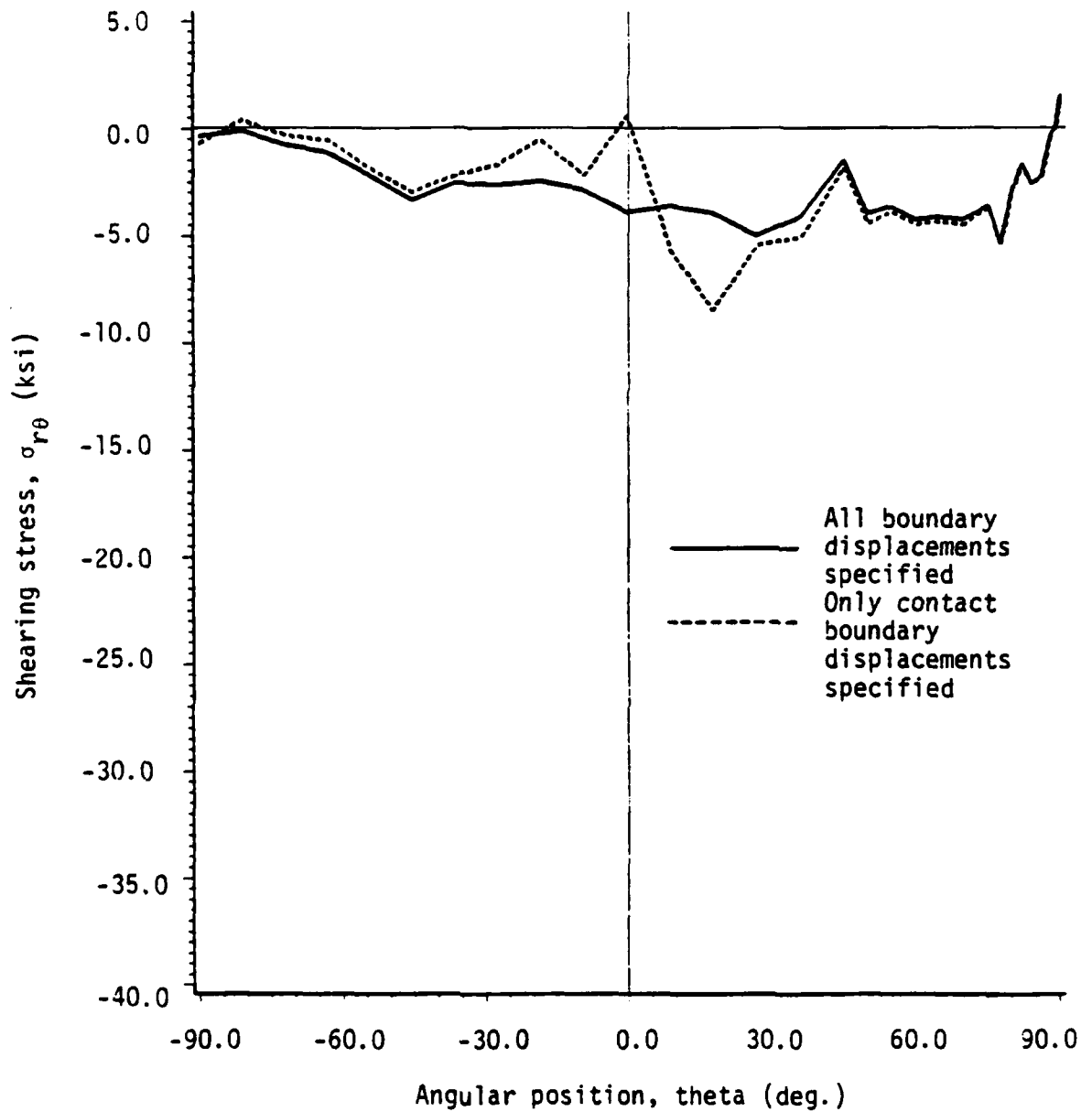


Figure 5.24 Shear contact stress distribution around hole boundary with varying regions of boundary displacements specified using linear elements

slightly more compressive from  $0^\circ$  to  $90^\circ$ , indicating that the specified displacements somewhat restrain the motion of the plate using this particular mesh.

The shearing stress distributions are also in good agreement except near the end of the contact region, where the stress values resulting from the specification of only the contact boundary node displacements dips slightly more negative and then goes to near zero before following the original stress distribution for the remainder of the hole boundary. Again, the shearing stresses remain much smaller than the corresponding radial stress components.

A final analysis was performed to determine the effects of geometric nonlinearity for this particular specimen. The final load step was applied along with the corresponding specified boundary displacements as a single load step in contrast to the incremental analysis that had been performed for the preceding examples. The resulting stresses and displacements were in excellent agreement with the results from the incremental solution, with all values within 1 percent of each other and most values much closer. The single load step analysis converged in three iterations whereas the incremental analysis converged in two iterations for each of the 9 applied load increments. Hence it appears that for this example, the effects of geometric nonlinearity are quite small. This is no doubt due to the relatively stiff material being used and the very small initial clearance between the plate and the pin.

In summary, the hybrid technique provides a useful alternative to strictly computational schemes for the analysis of the pin-plate problem in that no approximations are involved regarding the location of the

contact region or the regions of stick and slip. Since this information is provided by an actual physical test there are several unfortunate drawbacks to this method that have yet to be resolved. First, although the region of contact can be computed using the results of the hybrid technique with what appears to be good accuracy, the regions of stick and slip are still unknown since the relative displacements between the points of the pin and the plate in the tangential direction are not known. Second, the resulting radial and circumferential stress distributions on the hole boundary of the plate are relatively smooth and appear to be reasonable. The shear stresses, however, are very small compared to the radial stresses, have no uniform pattern around the hole boundary and are nonzero in the regions of no contact. Since the material used in the experiment was isotropic, this may mean that the extensional strains  $\epsilon_{rr}$  and  $\epsilon_{\theta\theta}$  are measured with good accuracy but either there is some problem in experimentally capturing the true shearing strains or numerically modeling the shearing stresses along the contact boundary of the plate. Other conclusions must await the computation of the boundary stresses using the moire fringe patterns and the results of additional experiments, which are to be reported by Joh [60].

## 6. SUMMARY AND CONCLUSIONS

### 6.1 Summary

A mixed variational statement and corresponding finite element model were developed for plane elastic bodies undergoing large deformations using the updated Lagrangian formulation. The mixed finite element formulation allows independent approximation of the displacements and stresses and both of these quantities appear as nodal variables. This formulation was applied to several plane elasticity contact problems to assess the efficiency and accuracy of this approach.

Using the mixed formulation, two separate computational algorithms were developed for the analysis of contact between two bodies considering the effects of friction. The first algorithm assumed that one of the bodies was perfectly rigid and circular in shape. The second algorithm was much more general and allowed for two bodies of arbitrary shape and constitution. Both techniques required the use of several iterative procedures to account for the accurate computation of the regions of contact and the regions of stick and slip between the two bodies. The mixed formulation yields stresses on the boundaries of the two bodies in contact since these components are nodal variables. This facet is a key advantage of this formulation since the contact stresses are not only part of the desired solution to the problem but are also used in several intermediate steps of the analysis. Both of these algorithms were applied to several example contact problems, including the well known Hertz problem and several examples involving contact between a plate under in-plane load containing a hole and a circular pin located within this hole.

A hybrid numerical/experimental method of contact analysis was developed using the mixed finite element formulation and the experimental technique of moire interferometry. This approach is unique in that there are no approximations required to determine the contact regions or the states of stick and slip as required by all strictly computational algorithms since the displacements on the contact interface are provided by the moire analysis. The only approximations involved in this technique are those due to the physical and mathematical limitations of the experimental and numerical techniques. This hybrid approach was applied to the problem of an aluminum plate with a hole restrained by a pin and subjected to an in-plane load.

## 6.2 Conclusions

The displacements computed from the mixed formulation applied to several linear and nonlinear plane elasticity problems are in good agreement with values computed using the more conventional displacement finite element model. The stresses computed using the mixed method, however, are not only slightly more accurate than those computed from a displacement formulation, but they are also computed precisely at the nodes. This is a valuable characteristic when applying this formulation to problems with stress concentrations or contact problems since the displacement formulation typically requires that the stresses be computed within the elements which are then somehow extrapolated to the boundaries.

Both contact algorithms yield reasonably accurate results for the contact problems analyzed in this study. The stress distributions and area of contact for the Hertz problem are in very good agreement with the analytical solution. The pin-loaded plate examples are generally

much more difficult to analyze in a computational sense. This is particularly true for the second algorithm, which must approximate the domains of both the plate and the pin. The results of the two algorithms are compared with results reported by other investigators using both numerical and experimental methods. The results are generally in good agreement with existing solutions, but at times the points of maximum stress computed by the second algorithm are not at the points of initial contact, which is typically the case for this type of problem. This might be due to the fact the approximation of the contact boundaries of two circular bodies using linear elements necessitates careful modeling of these bodies to ensure that they do not initially overlap. This phenomenon does not occur in the analysis of the Hertz problem, where the target body is modeled by a straight line, and for most contact problems analyzed here the results were consistent with those reported elsewhere. Care must be taken when applying these contact algorithms to problems with known stress discontinuities or singularities, since by definition the stresses must be continuous at the nodes.

The stress distributions computed from the hybrid algorithm for the analysis of an aluminum plate shows very large regions of contact for the example problem considered. This is due to the very small initial clearance between the pin and the plate. There is a very distinct jump in the radial contact stress distributions near the initial region of contact for all load steps, which appears to be due to several unexplained patterns in the displacement data. The shearing stresses are very small relative to the normal stresses, and the distributions have no uniform patterns. The contact stresses were computed by the



hybrid technique using two separate approaches: 1) specifying all displacement increments around the hole boundary, and 2) specifying only the displacement increments corresponding to the region of assumed contact. The assumed contact region was determined using the displacement data of the plate hole boundary nodes in the direction perpendicular to that of the applied load direction. The results of these two approaches are in good agreement with one another.

For the example problem considered, the contact stress distributions are similar regardless of whether a mesh of linear or quadratic elements is used, indicating that the mesh refinement yields little change in the stresses. Although the contact stresses computed by the hybrid technique are in fairly good agreement with the results of the second computational contact algorithm, no other comparisons are currently available.

Although the hybrid technique provides a unique way of obtaining the stress distributions within the plate domain with minimal computational effort compared with the numerical contact schemes, the technique unfortunately does not yield the regions of stick and slip between the plate and the pin. Such information could provide valuable information on the bounds of the static and dynamic coefficients of friction for the contacting bodies. It should be noted, however, that the moire technique does not involve measuring stresses; the stresses are computed from the measured displacements/strains using a stress-strain law that is assumed to be valid for the situation.

The computational algorithm for the contact analysis between two elastic bodies of arbitrary shape could be extended to higher order elements to allow the accurate modeling of two bodies with curved

boundaries in contact, such as in the case of the pin-loaded plate. This task is more complicated than it first appears since general expressions must be developed for the contact force potentials and the forces due to friction considering curved element sides and normal surface vectors that are constantly changing. This approach would be relatively straightforward to apply to problems such as that of Hertz, where the target body can be defined by a straight line. This would greatly simplify the formulation.

The mixed finite element model could also be modified to include the effects of material nonlinearity. This could be of significance in the analysis of contact problems since large stresses commonly occur at or near the region of contact, and nonlinear material response could have a dramatic effect on the contact stress distributions.

The hybrid technique consisting of the finite element method and moire interferometry may be applied to additional isotropic or anisotropic plates. It may be of use to consider specimens with a larger initial clearance between the pin and plate than was used in this study. This would decrease the total contact region and increase the region of sticking contact as well as help to minimize the effects of minor surface flaws near the initial points of contact.

## REFERENCES

1. Soni, S. R., "Failure Analysis of Composite Laminates with a Fastener Hole," ASTM STP 749, Joining of Composite Materials, pp. 145-164, 1981.
2. Chang, F. K., Scott, R. A. and Springer, G. S., "Strength of Mechanically Fastened Composite Joints," J. Comp. Mat., Vol. 16, pp. 470-494, Nov., 1982.
3. Nisida, M. and Saito, H., "Stress Distributions in a Semi-Infinite Plate Due to a Pin Determined by Interferometric Method," Experimental Mechanics, Vol. 6, No. 5, pp. 273-279, May 1966.
4. Oplinger, D. W. and Gandhi, K. R., "Analytical Studies of Structural Performance in Mechanically Fastened Fiber-Reinforced Plates," Proc. Army Symp. on Solid Mech., pp. 211-240, Sept. 1974.
5. de Jong, T., "Stresses Around Pin-Loaded Holes in Elastically Orthotropic or Isotropic Plates," J. Comp. Mat., Vol. 11, pp.313-331, July, 1977.
6. Mangalgi, P. D. and Dattaguru, B., "Elastic Analysis of Pin Joints in Composite Plates," Rep. No. ARDB-STR-5014, Dept. Aeronaut. Engng., Ind. Inst. Sci., Nov., 1980.
7. Wong, C. M. S. and Matthews, F. L., "A Finite Element Analysis of Single and Two-Hole Bolted Joints in Fibre-Reinforced Plastic," J. Comp. Mat., Vol. 15, pp. 481-491, Sept., 1981.
8. de Jong, T. and Vuil, H. A., "Stresses Around Pin-Loaded Holes in Elastically Orthotropic Plates with Arbitrary Load Direction," Report LR-333, Dept. of Aerospace Engng., Delft Univ. Tech., Sept. 1981.
9. de Jong, T., "The Influence of Friction on the Theoretical Strength of Pin-Loaded Holes in Orthotropic Plates," Rep. No. LR-350, Dept. of Aerospace Engng., Delft Univ. Tech., March, 1982.
10. Garbo, S. P. and Ogonowski, J. M., "Stress Concentration Factors for Finite Orthotropic Laminates with a Pin-Loaded Hole," NASA TP 1862, May, 1981.
11. Reddy, J. N., An Introduction to the Finite Element Method, McGraw-Hill, New York, 1984.
12. Zienkiewicz, O. C., The Finite Element Method, McGraw-Hill, New York, 1977.
13. Bathe, K. J., Finite Element Procedures in Engineering Analysis, Prentice Hall, Inc., New Jersey, 1982.

14. Reddy, J. N. and Oden, J. T., "Mixed Finite-Element Approximations of Linear Boundary-Value Problems," Q. Appl. Math., Vol. 33, No. 3, pp. 255-280, 1975.
15. Oden, J. T. and Reddy, J. N., "On Mixed Finite Element Approximations," SIAM J. Numer. Analysis, Vol. 13, No. 3, pp. 393-404, 1976.
16. Oden, J. T. and Lee, J. K., "Theory of Mixed and Hybrid Finite Element Approximations in Linear Elasticity," in Proc. IUTAM/IUM Sump. Applications of Methods of Functional Analysis to Problems of Mechanics, Marseilles, France, Sept. 1975.
17. Reissner, E., "On a Variational Theorem in Elasticity," J. Mathematical Physics, Vol. 29, 1950.
18. Dunham, R. S. and Pister, K. S., "A Finite Element Application of the Hellinger-Reissner Variational Theorem," Proc. Conf. Matrix Methods in Structural Mechanics, AFFDL-TR-68-150, pp. 471-487, 1968.
19. Pitkaranta, J. and Sternberg, R., "Analysis of Some Mixed Finite Element Methods for Plane Elasticity Equations," Mathematics of Computation, v. 41, n 164, pp. 399-423, 1983.
20. Mirza, F. A. and Olson, M. D., "The Mixed Finite Element Method in Plane Elasticity," Int. J. Numer. Meth. Engng., Vol. 15, pp. 273-289, 1980.
21. Murray, D. W. and Wilson, E. L., "Finite Element Large Deflection Analysis of Plates," J. Engng. Mech. Div., ASCE, Vol. 94, pp. 143-165, 1965.
22. Yaghmai S. and Popov, E. P., "Incremental Analysis of Large Deflections of Shells of Revolution," Int. J. Solids Struct., Vol. 7, pp. 1375-1393, 1971.
23. Stricklin, J. A., Von Riesenmann, W. A., Tillerson, J. R. and Haisler, W. E., "Static Geometric and Material Nonlinear Analysis," Adv. in Comp. Meth. in Struct. Mech. and Design, J. T. Oden, R. W. Clough and Y. Yamamoto (eds.), Univ. of Alabama in Huntsville, pp. 301-324, 1972.
24. Yamada, Y., "Incremental Formulations for Problems with Geometric and Material Nonlinearities," Adv. in Comp. Meth. in Struct. Mech. and Design, J. T. Oden, R. W. Clough and Y. Yamamoto (eds.), Univ. of Alabama in Huntsville, pp. 325-355, 1972.
25. Hibbit, H. D., Marcel, P. V. and Rice, J. R., "Finite Element Formulation for Problems of Large Strain and Large Displacements," Int. J. Solids and Struct., Vol. 6, pp. 1069-1086, 1970.

26. McNamara, J. F., "Incremental Stiffness Method for Finite Element Analysis of the Nonlinear Dynamic Problem," Ph.D. Thesis, Dept. of Engng., Brown University, 1972.
27. Haug, E. and Powell, G. H., "Finite Element Analysis of Nonlinear Membrane Structures," SESM Report No. 72-7, Dept. of Civil Engng., Univ. of California, Berkeley, 1972.
28. Chao, W. C. and Reddy, J. N., "Analysis of Laminated Composite Shells Using a Degenerated 3-D Element," Int. J. Numer. Meth. Engng., Vol. 20, pp. 1991-2007, 1984.
29. Pian, T. H. H. and Tong, Pin, "Variational Formulation of Finite-Displacement Analysis," High Speed Computing of Elastic Structures, B. Fraeiji de Veubeke (ed.), University of Liege, Belgium, pp. 43-63, 1971.
30. Bathe, K. J., Ramm, E. and Wilson, E. L., "Finite Element Formulations for Large Deformation Dynamic Analysis," Int. J. Numer. Meth. Engng., Vol. 9, pp. 353-386, 1975.
31. Haisler, W. E., Sticklin, J. A., and Stebbins, F. J., "Development and Evaluation of Solution Procedures for Geometrically Nonlinear Structural Analysis," AIAA J., Vol. 10, No. 3, pp. 264-272, 1972.
32. Mondkar, P. and Powell, G. H., "Finite Element Analysis of Nonlinear Static and Dynamic Response," Int. J. Numer. Meth. Engng., Vol. 11, pp. 499-520, 1977.
33. Horrignoe, G. and Bergan, P. G., "Incremental Variational Principles and Finite Element Models for Nonlinear Problems," Comp. Meth. Appl. Mech. Eng., Vol. 7, pp. 201-217, 1976.
34. Hertz, H., "On the Contact of Elastic Solids," J. Math., Vol. 92, pp. 156-171, 1881.
35. Chan, S. K., and Tuba, I. S., "A Finite Element Method for Contact Problems of Solid Bodies - Part I. Theory and Validation," Int. J. Mech. Sci., Vol. 13, pp. 615-625, 1971.
36. Bathe, K. J. and Chaudhary, A., "A Solution Method for Planar and Axisymmetric Contact Problems," Int. J. Numer. Meth. Engng., Vol. 21, pp. 65-88, 1985.
37. Campos, L. T., Oden, J. T. and Kikuchi, N., "A Numerical Analysis of a Class of Contact Problems with Friction in Elastostatics," Comp. Meth. Appl. Eng., Vol. 34, pp. 821-845, 1982.
38. Francavilla, A. and Zienkiewicz, O. C., "A Note on Numerical Computation of Elastic Contact Problems," Int. J. Numer. Meth. Eng., Vol. 9, pp. 913-924, 1975.

39. Sachdeva, T. D. and Ramakrishnan, C. V., "A Finite Element Solution for the Two-Dimensional Elastic Contact Problems with Friction," Int. J. Numer. Meth. Eng., Vol. 17, pp. 1257-1271, 1981.
40. Marks, W. R. and Salamon, N. J., "A Modified Conjugate Gradient Method for Frictionless Contact Problems," J. Vib. Stress, Rel. in Design, Vol. 105, pp. 242-246, April 1983.
41. Mahoud, F. F., Salamon, N. J. and Marks, W. R., "A Direct Automated Procedure for Frictionless Contact Problems," Int. J. Numer. Meth. Eng., Vol. 18, pp. 245-257, 1982.
42. Okamoto, N. and Nakazawa, M., "Finite Element Incremental Contact Analysis with Various Frictional Conditions," Int. J. Numer. Meth. Eng., Vol. 14, pp. 337-357, 1979.
43. Fredrikson, B., "Finite Element Solution of Surface Nonlinearities in Structural Mechanics with Special Emphasis to Contact and Fracture Mechanics Problems," Comp. and Struc., Vol. 6, pp. 281-190, 1976.
44. Haslinger, J. and Hlavacek, I., "Approximations of the Signorini Problem with Friction by a Mixed Finite Element Method," J. Mathematical Analysis and Applications, Vol. 86, pp. 99-122, 1982.
45. Tseng, J. and Olsen, M. D., "The Mixed Finite Element Method Applied to Two-Dimensional Elastic Contact Problems," Int. J. Numer. Meth. Engng., Vol. 17, pp. 991-1014, 1981.
46. Klang, E. C. and Hyer, M. W., "The Stress Distribution in Pin-Loaded Orthotropic Plates," Report No. CCMS-85-05, Virginia Polytechnic Institute and State University, Blacksburg, Virginia, 24061, June, 1985.
47. Wilkinson, T. L., Rowlands, R. E. and Cook, R. D., "An Incremental Finite-Element Determination of Stresses Around Loaded Holes in Wood Plates," Computers and Structures, Vol. 14, pp. 123-128, 1981.
48. Rahman, M. U., Rowlands, R. E., Cook, R. D. and Wilkinson, T. L., "An Iterative Procedure for Finite-Element Stress Analysis of Frictional Contact Problems," Computers and Structures, Vol. 18, pp. 947-954, 1984.
49. Wilkinson, T. L. and Rowlands, R. E., "Analysis of Mechanical Joints in Wood," Exper, Mech., Vol. 21, No. 10, pp. 408-414, Nov., 1981.
50. Rao, A. K., "Elastic Analysis of Pin Joints," Comp. and Struct., Vol. 9, pp. 125-144, 1978.
51. Reddy, J. N., Energy and Variational Methods in Applied Mechanics, Wiley, New York, 1984.

52. Malvern, L. E., Introduction to the Mechanics of a Continuous Medium, Prentice-Hall, Englewood Cliffs, N.J., 1974.
53. Mirza, F. A., "A Solution Technique for Indefinite Systems of Mixed Finite Elements," Int. J. Numer. Meth. Engng., Vol. 20, pp. 1555-1561, 1984.
54. Hinton, E., Scott, F. C. and Ricketts, R. E., "Local Least Squares Stress Smoothing for Parabolic Isoparametric Elements," Int. J. Numer. Meth. Engng., Vol. 9, pp. 235-238, 1975.
55. Loubignac, G., Cantin, G. and Touzot, G., "Continuous Stress Fields in Finite Element Analysis," AIAA J., 15, pp. 1645-1646, 1977.
56. Dally, J. W. and Riley, W. F., Experimental Stress Analysis, McGraw-Hill, New York, 1978.
57. Post, D., "Developments in Moire Interferometry," Optical Engineering, Vol. 21, No. 3, pp. 458-467, June, 1982.
58. Post, D., "Moire Interferometry at VPI&SU," Experimental Mechanics, Vol. 23, No. 2, pp. 203-210, June, 1983.
59. Post, D., "Moire Interferometry for Deformation and Strain Studies," Optical Engineering, Vol. 24, No. 4, pp. 663-667, July/August 1985.
60. Joh, D., "An Experimental Study of Frictional Phenomena Around the Pin Joints of Plates Using Moire Interferometry," Ph.D. Thesis, Engineering Science and Mechanics, Virginia Polytechnic Institute, 1986 (in preparation).
61. Holden, J. T., "On the Finite Deflections of Thin Beams," Int. J. Solids Struct., Vol. 8, pp. 1051-1055, 1972.
62. Pagano, N. J., "Analysis of the Flexure Test of Bidirectional Composites," J. Comp. Mat., Vol. 1, p. 336, 1967.
63. Timoshenko, S. P. and Goodier, J. N., Theory of Elasticity, McGraw-Hill, 1970.
64. Wilkinson, T. L. and Rowlands, R. E., "Influence of Elastic Properties on the Stresses in Bolted Joints in Wood," Wood Sci., Vol. 14, pp. 15-22, 1981.
65. Cuthill, E. and McKee, J., "Reducing the Bandwidth of Sparse Symmetric Matrices," Proc. 24th Nat. Conf. of the ACM, ACM Publ. P-69, Association for Computing Machinery, New York, pp. 157-172, 1969.

## APPENDIX

The finite element equations (2.28) can also be written in more explicit form as

$$\begin{bmatrix} [K^{11}] & [0] & [K^{13}] & [0] & [K^{15}] \\ [0] & [K^{22}] & [0] & [K^{24}] & [K^{25}] \\ [K^{31}] & [0] & [K^{33}] & [K^{34}] & [K^{35}] \\ [0] & [K^{42}] & [K^{43}] & [K^{44}] & [K^{45}] \\ [K^{51}] & [K^{52}] & [K^{53}] & [K^{54}] & [K^{55}] \end{bmatrix} \begin{Bmatrix} \{u\} \\ \{v\} \\ \{S_{xx}\} \\ \{S_{yy}\} \\ \{S_{xy}\} \end{Bmatrix} = \begin{Bmatrix} \{F^{L1}\} \\ \{F^{L2}\} \\ \{0\} \\ \{0\} \\ \{0\} \end{Bmatrix} - \begin{Bmatrix} \{F^{NL1}\} \\ \{F^{NL2}\} \\ \{0\} \\ \{0\} \\ \{0\} \end{Bmatrix}$$

where

$$K_{ij}^{13} = \int_{\Omega} \frac{\partial \psi_i}{\partial x} \psi_j dx dy = K_{ji}^{31}$$

$$K_{ij}^{15} = \int_{\Omega} \frac{\partial \psi_i}{\partial y} \psi_j dx dy = K_{ji}^{51}$$

$$K_{ij}^{24} = \int_{\Omega} \frac{\partial \psi_i}{\partial y} \psi_j dx dy = K_{ji}^{42}$$

$$K_{ij}^{25} = \int_{\Omega} \frac{\partial \psi_i}{\partial x} \psi_j dx dy = K_{ji}^{52}$$

$$K_{ij}^{33} = - \int_{\Omega} D_{11} \psi_i \psi_j dx dy$$

$$K_{ij}^{34} = - \int_{\Omega} D_{12} \psi_i \psi_j dx dy = K_{ji}^{43}$$



$$K_{ij}^{35} = - \int_{\Omega} D_{16} \psi_i \psi_j dx dy = K_{ji}^{53}$$

$$K_{ij}^{44} = - \int_{\Omega} D_{22} \psi_i \psi_j dx dy$$

$$K_{ij}^{45} = - \int_{\Omega} D_{26} \psi_i \psi_j dx dy = K_{ji}^{54}$$

$$K_{ij}^{55} = - \int_{\Omega} D_{66} \psi_i \psi_j dx dy$$

$$K_{ij}^{11} = K_{ij}^{22} = \int_{\Omega} \left[ \tau_{xx} \frac{\partial \psi_i}{\partial x} \frac{\partial \psi_j}{\partial x} + \tau_{xy} \left( \frac{\partial \psi_i}{\partial x} \frac{\partial \psi_j}{\partial y} + \frac{\partial \psi_i}{\partial y} \frac{\partial \psi_j}{\partial x} \right) + \tau_{yy} \frac{\partial \psi_i}{\partial y} \frac{\partial \psi_j}{\partial y} \right] dx dy$$

$$F_i^{L1} = \int_{\Omega} f_x \psi_i dx dy + \oint_{\Gamma} (\tau_{xx} n_x + \tau_{xy} n_y) \psi_i dS$$

$$F_i^{L2} = \int_{\Omega} f_y \psi_i dx dy + \oint_{\Gamma} (\tau_{xy} n_x + \tau_{yy} n_y) \psi_i dS$$

$$F_i^{NL2} = \int_{\Omega} \left( \tau_{xx} \frac{\partial \psi_i}{\partial x} + \tau_{xy} \frac{\partial \psi_i}{\partial y} \right) dx dy$$

$$F_i^{NL2} = \int_{\Omega} \left( \tau_{xy} \frac{\partial \psi_i}{\partial x} + \tau_{yy} \frac{\partial \psi_i}{\partial y} \right) dx dy$$

Note: The Cauchy stresses  $\tau_{ij}$  are computed using nodal stress interpolation and not using the Almansi strains. For the first iteration, the Cauchy stresses are zero and hence  $[K^{11}]$  is a null matrix. This yields an indefinite system and an equation solver should be selected accordingly for this first iteration.

The contact matrices and contact force vectors given in Eq. (3.13) can be expressed in explicit form as follows:

Sticking Contact

$$\begin{bmatrix} [0] & [K_C^{13}] \\ [K_C^{13}]^T & [K_C^{33}] \end{bmatrix} =$$

$$\begin{bmatrix} 0 & 0 & 0 & 0 & 0 & 0 & -1 & 0 \\ 0 & 0 & 0 & 0 & 0 & 0 & 0 & -1 \\ 0 & 0 & 0 & 0 & 0 & 0 & (1-\beta)^{(i-1)} & 0 \\ 0 & 0 & 0 & 0 & 0 & 0 & 0 & (1-\beta)^{(i-1)} \\ 0 & 0 & 0 & 0 & 0 & 0 & \beta^{(i-1)} & 0 \\ 0 & 0 & 0 & 0 & 0 & 0 & 0 & \beta^{(i-1)} \\ -1 & 0 & (1-\beta)^{(i-1)} & 0 & \beta^{(i-1)} & 0 & 0 & 0 \\ 0 & -1 & 0 & (1-\beta)^{(i-1)} & 0 & \beta^{(i-1)} & 0 & 0 \end{bmatrix}$$

$$\{2_{R_C}^{(i-1)}\} = \begin{pmatrix} 2_{\lambda_{Kx}}^{(i-1)} \\ 2_{\lambda_{Ky}}^{(i-1)} \\ -(1 - \beta^{(i-1)}) 2_{\lambda_{Kx}}^{(i-1)} \\ -(1 - \beta^{(i-1)}) 2_{\lambda_{Ky}}^{(i-1)} \\ -\beta^{(i-1)} 2_{\lambda_{Kx}}^{(i-1)} \\ -\beta^{(i-1)} 2_{\lambda_{Ky}}^{(i-1)} \end{pmatrix}$$

$$\{\Delta U^{(i)}\} = \begin{pmatrix} \Delta u_{Kx}^{(i)} \\ \Delta u_{Ky}^{(i)} \\ \Delta u_{Ax}^{(i)} \\ \Delta u_{Ay}^{(i)} \\ \Delta u_{Bx}^{(i)} \\ \Delta u_{By}^{(i)} \end{pmatrix}$$

The above two vectors are the same in the case of sliding contact,

$$\{\Delta \lambda^{(i)}\} = \begin{pmatrix} \Delta \lambda_{Kx}^{(i)} \\ \Delta \lambda_{Ky}^{(i)} \end{pmatrix} \quad \{t+\Delta t_{\Delta_C}^{(i-1)}\} = \begin{pmatrix} \Delta_{Kx}^{(i-1)} \\ \Delta_{Ky}^{(i-1)} \end{pmatrix}$$

### Sliding Contact

$$\begin{bmatrix} [0] & [K_C^{13}] \\ [K_C^{13}]^T & [K_C^{33}] \end{bmatrix} =$$

$$\begin{bmatrix} 0 & 0 & 0 & 0 & 0 & 0 & n_{sx} & 0 \\ 0 & 0 & 0 & 0 & 0 & 0 & n_{sy} & 0 \\ 0 & 0 & 0 & 0 & 0 & 0 & -(1-\beta^{(i-1)})n_{sx} & 0 \\ 0 & 0 & 0 & 0 & 0 & 0 & -(1-\beta^{(i-1)})n_{sy} & 0 \\ 0 & 0 & 0 & 0 & 0 & 0 & -\beta n_{sx} & 0 \\ 0 & 0 & 0 & 0 & 0 & 0 & -\beta n_{sy} & 0 \\ n_{sx} & n_{sy} & -(1-\beta^{(i-1)})n_{sx} & -(1-\beta^{(i-1)})n_{sy} & -\beta n_{sx} & -\beta n_{sy} & 0 & 0 \\ 0 & 0 & 0 & 0 & 0 & 0 & 0 & 1 \end{bmatrix}$$

$$\{\Delta \lambda^{(i)}\} = \begin{pmatrix} \Delta \lambda_s^{(i)} \\ \Delta \lambda_r^{(i)} \end{pmatrix} \quad \{^2_{\Delta_C}^{(i-1)}\} = \begin{pmatrix} -n_{sx} \Delta_{Kx}^{(i-1)} - n_{sy} \Delta_{Ky}^{(i-1)} \\ 0 \end{pmatrix}$$

Note that in the case of sliding contact, we must compute the increments in the contact forces in Cartesian coordinates using the equations

$$\Delta\lambda_{Kx}^{(i)} = -\Delta\lambda_S^{(i)} n_{sx}$$

$$\Delta\lambda_{Ky}^{(i)} = -\Delta\lambda_S^{(i)} n_{sy}$$

UNCLASSIFIED

SECURITY CLASSIFICATION OF THIS PAGE (When Data Entered)

REPORT DOCUMENTATION PAGE		READ INSTRUCTIONS BEFORE COMPLETING FORM
1. REPORT NUMBER VPI-E-86.17	2. GOVT ACCESSION NO. ADA172145	3. RECIPIENT'S CATALOG NUMBER
4. TITLE (and Subtitle) A MIXED COMPUTATIONAL ALGORITHM BASED ON THE UPDATEDLAGRANGIAN DESCRIPTION FOR PLANE ELASTIC CONTACT PROBLEMS	5. TYPE OF REPORT & PERIOD COVERED Interim	
	6. PERFORMING ORG. REPORT NUMBER ONR-MECH-R-3	
7. AUTHOR(s) P. R. Heyliger and J. N. Reddy	8. CONTRACT OR GRANT NUMBER(s) N00014-84-K-0552	
9. PERFORMING ORGANIZATION NAME AND ADDRESS Virginia Polytechnic Institute and State University Blacksburg, Virginia 24061	10. PROGRAM ELEMENT, PROJECT, TASK AREA & WORK UNIT NUMBERS NR-064-727/5-4-84 (430)	
11. CONTROLLING OFFICE NAME AND ADDRESS Office of Naval Research Mechanics Division (Code 430) 800 N. Quincy St., Arlington, VA 22217	12. REPORT DATE August 1986	
	13. NUMBER OF PAGES 122	
14. MONITORING AGENCY NAME & ADDRESS (if different from Controlling Office)	15. SECURITY CLASS. (of this report) UNCLASSIFIED	
	15a. DECLASSIFICATION/DOWNGRADING SCHEDULE	
16. DISTRIBUTION STATEMENT (of this Report)  This document has been approved for public release and sale; distribution unlimited.		
17. DISTRIBUTION STATEMENT (of the abstract entered in Block 20, if different from Report)		
18. SUPPLEMENTARY NOTES		
19. KEY WORDS (Continue on reverse side if necessary and identify by block number) contact problems, finite element analysis, friction, hybrid technique, large deformations, stick and slip, updated Lagrangian description.		
20. ABSTRACT (Continue on reverse side if necessary and identify by block number) A mixed variational formulation and associated finite element model are deve- loped for the stress analysis of plane elastic bodies in contact and undergoing large deformations (large displacements and small strains). The updated Lagran- gian formulation is used to develop the incremental equations. The finite ele- ment model contains displacements and the components of the second Piola-Kirchh- off stress tensor as the nodal degrees of freedom. Two different computational algorithms are developed to analyze the separate cases of rigid pin and elastic pin. The procedure accounts for friction between the contacting bodies (cont.)		

DD FORM 1473  
1 JAN 73

EDITION OF 1 NOV 65 IS OBSOLETE


UNCLASSIFIED

SECURITY CLASSIFICATION OF THIS PAGE (When Data Entered)

20. ABSTRACT (continued from the previous page)

→ and the computational difficulties associated with the unknown contact area.

A hybrid technique is also presented that combines the ~~numerical~~ ~~(finite element)~~ procedure and the moire inteferometry to determine stresses in a pin-loaded plate. The procedure involves the use of the displacements measured in the experiment (moire technique) as boundary conditions at the pin-hole interface of the finite element analysis. Then the whole field information of displacements and stresses is obtained using the finite element method. Results of this hybrid technique are compared with those obtained by the numerical algorithm ~~developed in the present study~~. The results are found to be in good agreement.



ENM

IP - 86

DTIC